Rijksinstituut voor Volksgezondheid
en Milieu
*Ministerie van Volksgezondheid,
Welzijn en Sport*

The OPS-model

Description of OPS 5.3.1.0

Ferd Sauter
Koen Siteur
Marina Sterk
Eric van der Swaluw
Roy Wichink Kruit
Wilco de Vries

The following authors have contributed to previous versions of this report of which parts are still included in the current documentation: Hans van Jaarsveld, Margreet van Zanten, Jan Aben, Frank de Leeuw, Addo van Pul.

National Institute for Public Health and the Environment (RIVM)

Changes with respect to previous description (v5.1.1.0)

FS   2023-07-05 Finished documentation of version v5.1.1.0.
FS   2023-07-31 Added more information on the role of the NH_3 background map in Table 7. 7.3.
FS   2023-08-03 Renewed Figure 5.11; old graph erroneously showed R_{part} instead of $1/R_{part}$.
FS   2024-03-19 Corrected text for x-axis of Figure 4.3.
KS   2025-05-02 Updated the map with meteorological regions and KNMI measurement sites (*Figure 2.1*), after changes described by Wichink Kruit et al. (2024; RIVM-rapport 2024-0095).
KS   2025-05-02 Added reference to Wichink Kruit et al. (2024; RIVM-rapport 2024-0095) for description of derivation of Γ_{water}-maps (Section 5.4.1).
KS   2025-05-02 Update of description of iterative procedure for background maps (Section 7.3).
KS   2025-05-02 Introduction of the ROADS option for modelling dispersion near roads (Section 3.3.2).

Summary

This report describes in detail the OPS (Operational Priority Substances) model. OPS simulates the atmospheric process sequence of emission, dispersion, transport, chemical conversion and deposition. The main purpose of the model is to calculate the concentration and deposition of pollutants (e.g. particulate matter, acidifying compounds like SO_2, NO_x and NH_3) for the Netherlands using a high spatial resolution (typical 1 x 1 km^2). The model is, however, set up as a universal framework supporting the modelling of other pollutants such as fine particles and persistent organic pollutants. Previous versions of the model have been used since 1989 for atmospheric transport and deposition calculations published in the State of the Environment reports and Environmental Outlook studies in the Netherlands. Current versions are in use for the production of large-scale maps of air pollution in the Netherlands (Hoogerbrugge et al. 2019).

This report is an update of the report *Description and validation of OPS-Pro 4.1,* RIVM report 500045001/2004 (van Jaarsveld, 2004). In this update, some processes have been described in more detail with explanatory figures. Furthermore, model changes, which have taken place since 2004, have been described. A summary of the changes with respect to the previous OPS documentation are listed on page 2 of this document. The various model validation exercises, described in van Jaarsveld (2004) are not repeated here, but instead a list of model comparison and validation studies is provided in Chapter 8. Detailed information on the dry depositon module DEPAC, which is used in OPS, is given in van Zanten et al. (2010).

Contents

1. Model description

1.1   Introduction

Modelling atmospheric processes has been the subject of many studies, resulting in a range of models with various complexities for specific applications. Before selecting a model or a model approach, we have to assess the intended application area carefully. In the present case, the time scale (long-range with a time resolution of a season or a few months) is probably the most important boundary condition. Another important condition is the spatial scale of the receptor area, which is defined as the Netherlands with a resolution of 5 x 5 km^2 or 1 x 1 km^2. The emission area, however, must be at least 2000 x 2000 km^2 to explain the contribution of long-range transport to the levels of pollutants in the Netherlands. When OPS came into use (around 1985), these conditions forced exclusion of an Eulerian model framework, simply because of the required computer capacity. Furthermore, Eulerian models can suffer from large errors on a local scale, due to numerical dispersion. Eulerian models using nested grids should, to a certain extent, be applicable; however, operational models of this type were not available at that time.

An efficient method for calculating long-term averages is arranging situations having similar properties into classes and then calculating representative concentrations for each of the classes. The average value will then follow from a summation of all concentrations, weighted with their relative frequencies of occurrence. Such a method is used for the OPS-model and is described in this chapter. One of the problems that arises from this approach is the choice of a good classification scheme on the basis of relevant parameters. For short-range models, a classification is usually made on the basis of wind direction, wind speed and atmospheric stability (see, for example Calder, 1971; Runca *et al*., 1982). As will be explained in more detail later on, OPS uses a classification based on transport distance, wind direction and a combination of atmospheric stability and mixing height.

The approach used for the OPS-model, can be classified as a long-term climatological trajectory model which treats impacts of sources on a receptor independently. The model is basically a linear model. Because properties that depend on other species are computed using background concentrations taken from a series of OPS concentration maps, one may call it a pseudo non-linear model. The physical background of the model concept and the derivation of relevant meteorological parameters from routine meteorological observations will be described in this chapter.

1.2   Substances

The OPS model works with three groups of substances:
1. Acidifying and eutrophying substances (SO_2, NO_x, NH_3 and secondary products).
2. Non-acidifying (gaseous) substances
3. Particle-bounded substances.

Acidifying and eutrophying substances
Important environmental problems are the so-called acidification and eutrophication of ecosystems through the deposition of acidifying and eutrophying components. In this case a number of relevant processes have to be included in the model approach, since otherwise the model cannot adequately describe spatial differences and/or the development in time. Another reason for a special treatment of these components is the more than average availability of experimental data on emission, conversion and deposition processes. In OPS, the acidifying components include:

sulphur compounds (SO_x)	sulphur dioxide (SO_2)
	sulphate (SO_4^{2-})
oxidised nitrogen compounds (NO_y)	nitrogen oxides (NO and NO_2)
	peroxyacetyl nitrate (PAN)
	nitrous acid (HNO_2)
	nitric acid (HNO_3)
	nitrate (NO_3^-)
reduced nitrogen compounds (NH_y)	ammonia (NH_3)
	ammonium (NH_4^+)

The gaseous SO_2, NO and NH_3 are primary emitted pollutants, while the gaseous NO_2, PAN, HNO_2 and HNO_3 and the non-gaseous SO_4^{2-}, NO_3^- and NH_4^+ are formed from the primary pollutants in the atmosphere under influence of, for example, ozone (O_3) or free OH-radicals. In OPS, the primary oxidised nitrogen pollutant is defined as the sum of NO and NO_2, further denoted as NO_x. The secondary products SO_4^{2-}, NO_3^- and NH_4^+ form mainly ammonia salts having low vapour pressures and consequently appearing as aerosols in the atmosphere (Stelson and Seinfeld, 1982).

Non-acidifying (gaseous) substances
The group of non-acidifying substances uses a generic approach in which the properties of the substance are expressed in general terms such as:
  - a chemical conversion/degradation rate
  - a dry deposition velocity or a surface resistance
  - a wet scavenging ratio.

Particle-bounded substances
A generic approach is followed for substances attached to particles in which the size distribution of the particles fully defines their atmospheric behaviour.

1.3   Model characteristics

The long-term OPS-LT model, which is outlined here, is a long-term Lagrangian transport and deposition model that describes relations between individual sources or source areas, and individual receptors by Gaussian plumes. The model is statistical in the sense that concentration and deposition values are calculated for a number of typical situations (classes) and the long-term value is obtained by summation of these values, weighted with their relative frequencies of occurrence.

The short-term OPS-ST model is used on an hourly basis and computes hourly concentrations and depositions for a limited area (~ 0 - 50 km) only, using steady-state Gaussian plumes. The OPS-ST model will be described in a separate report. The description in this report is for the OPS-LT model, but many processes are modelled in OPS-ST in the same way.

All equations governing the transport and deposition process are solved analytically, allowing the use of non-gridded receptors and sources, and variable grid sizes. OPS-LT assumes that transport from a source to a receptor takes place in straight, well-mixed sectors of height z_i and horizontal angles of 30° (see Figure 1.1).
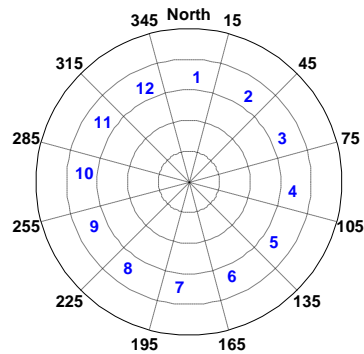
Figure 1.1.   OPS wind rose for 12 wind sectors of 30°; wind direction North = 0°.

Corrections are applied close to the source to account for emission height and vertical dispersion; a correction for the curved nature of real transport paths is used for larger distances (see section 0 for more detail). An important difference with (true) probabilistic long-term models is that the OPS model is driven by actually observed meteorological parameters (hourly or 6-hourly synoptical data).

A schematic overview of the OPS model, consisting of three main parts, is given in Figure 1.2. These parts are:

a.   a primary pre-processor MPARKNMI that reads hourly meteorological observations and interpolates these observations to 6 meteorological regions in the Netherlands.

b.   A secondary pre-processor METPRO that calculates transport trajectories arriving at a receptor on the basis of hourly wind observations. METPRO also derives secondary parameters, which define the atmospheric state along the trajectories from the observed data. This pre-processor classifies hourly meteo data into groups with similar properties and, in this way, describes the necessary statistics for the relevant period.

c.   The OPS-model itself, which computes concentrations and depositions on the basis of various inputs.

Each part is used separately. The pre-processors have to be run once for each period (month, season, year or a number of years) and for each meteorological district that is used in OPS (see Figure 2.1). Results are placed in a database as a set of tables, consisting of frequencies of occurrence of a combination of transport distance, wind direction and stability/mixing height class. The OPS-model selects its necessary climatological data from the database, depending on the location of the receptor, the source-receptor direction and the period of interest.
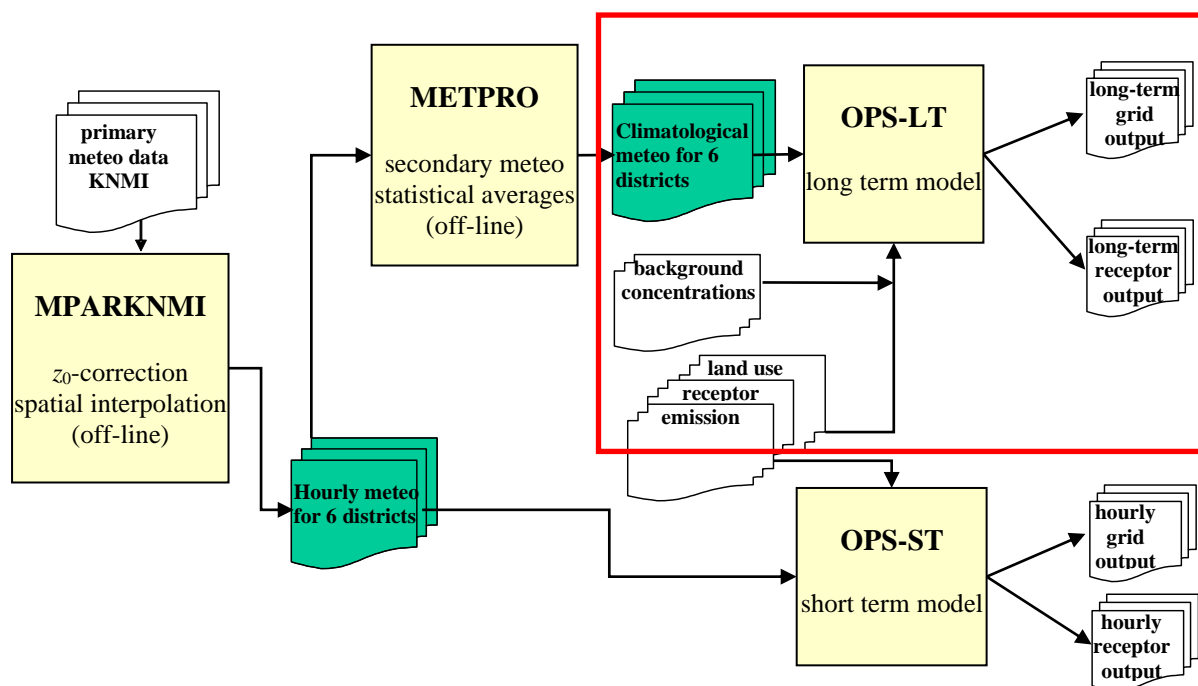
Figure 1.2 Schematic view of the long term and short term OPS models with its pre-processing steps by the programs MPARKNMI and METPRO. Note that most users will only use the OPS-LT part in the red box.

The basic meteorological input consists of wind direction and wind speed at two heights, precipitation data, global radiation (or cloud cover), temperature and snow cover, all measured at one or more locations in the Netherlands.

Long range transport is modelled under the assumption that meteorological conditions in the whole model area at a certain hour are equal to the conditions in the Netherlands at the same hour. Since we combine all wind observations in the Netherlands into an average wind vector, we assume that this vector is representative for an area at least twice the size of the Netherlands (NL ~ 200-300 km). A further argument is the use of observations at greater heights (TV-towers (120-300 m) and a meteorological tower (200 m)), together producing data representative for a larger area. Finally, one may consider that long range transport takes place mainly during higher wind speeds, when wind direction is less variable and transport time is low.

Other inputs into the model are information on receptors and information on sources (coordinates, emission strength, height, horizontal dimensions, etc.). The output of the model includes concentration, dry deposition and wet deposition data, listed either by receptor or in gridded form.

1.3.1 Receptors

The area for which concentrations and depositions can be calculated is determined by the size of the area for which meteorological parameters are known. Since the standard climatological data set used for this model is based on observations from the Royal Netherlands Meteorological Institute (KNMI), the maximum size of the receptor area becomes, in effect, the Netherlands and adjoining regions. The land-use and terrain roughness data maps, covering only the Netherlands in great detail, also impose limitations.

Receptor parameters that need to be specified are coordinates, roughness length and land use. The receptor height is fixed within the OPS model. In terms of the vertical dispersion, the receptor height is set to 0 m. In terms of the influence of dry deposition on the vertical concentration profile, the receptor height is 3.8 m, in other words, the measuring height of the Netherlands' air quality measuring network LML.

The OPS-model reads the land-use type and the roughness length of the receptor location from maps. For specific receptor locations the model selects the land-use properties from the 250 m resolution map. In the case of gridded receptor points, the model selects a corresponding spatial resolution (250, 500, 1000, 5000 m). It is important to note here that the calculation of a grid-cell representative

roughness length is based on a logarithmic weighing of roughness elements, while the grid cell representative land-use type is defined as the most abundant land-use type within that grid cell.

This model does not explicitly take into account the direct influence of obstacles (e.g. buildings) on the dispersion. Instead, the general influence of obstacles is expressed in the terrain roughness variable, assuming that obstacles are homogeneously distributed over the emission-receptor area. The shortest source-receptor distance for which this model may be used is therefore taken as a function of the terrain roughness length. In flat terrain with no obstacles the minimum distance is in the order of 20 m. For a terrain roughness > 0.1 m, the shortest distance is approx. 200 times the roughness length. When the stack is part of a building, the shortest distance is at least five times the height of the building. The model generates no warnings if these rules are violated. One should be aware that in the case of gridded receptor points in combination with point sources, the minimum source-receptor distance requirement cannot always be met.

Receptor points for calculating concentrations and depositions can be chosen:

- ♦ on a regular (Cartesian) grid, with a grid distance to be chosen. The domain may be pre-defined (the Netherlands) or defined by the user.
- ♦ for a number of specific locations to be defined by the user.

The output format differs according to the option chosen. The latter option is especially useful when results have to be compared with observations. The gridded results are formatted in a matrix form, while the results for specific receptor points are formatted as single records for each point.

When the user selects grid output, OPS automatically generates multiple sub-receptors inside a grid cell in order to be able to compute a representative grid cell average. The number of sub-receptors goes to 1 with increasing source-receptor distance.

1.3.2 Trajectories

OPS uses trajectories to assess whether a certain source contributes to the concentration at a certain receptor. A simple example, for two time steps with different wind directions, is shown in Figure 1.3.
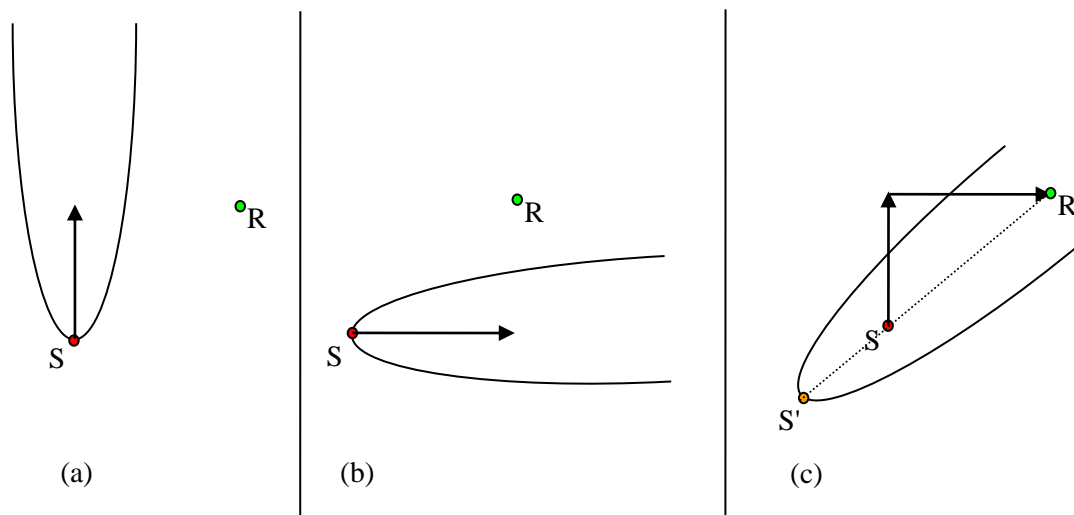
Figure 1.3 Example of computing the contribution of a source S to a receptor R. (a) t = 1: Southern wind, plume starting at S; no contribution to R. (b) t = 2: Western wind, plume starting at S; no contribution to R. (c) t = 2: contribution of source S emitted at t = 1, according to plume starting at S' in the direction S-R. Note that to account for the real travel distance along the trajectory, the source S has been shifted to a virtual location S'.

Each hour, the meteo-preprocessor METPRO traces back the path followed by an air parcel arriving at a receptor point, for four days. The idea is to compute averaged meteo and deposition parameters over this trajectory for four representative distances. METPRO splits such a trajectory into four independent parts:

1. one part representing contributions of local sources S_1 in the direction φ_1
2. one part representing contributions of sources S_2 at an intermediate distance (100 km) from the receptor in the direction φ_2
3. one part for sources S_3 at a long distance (300 km) from the receptor in the direction φ_3
4. one part for sources S_4 at a very long distance (1000 km) from the receptor in the direction φ_4 .

For an arbitrary source, inter- and extrapolation is used between distances and wind directions (see Figure 1.4).

A split-up in transport scale is preferred to a split-up in time scales because the trajectories can be directly related to the real positions of receptors and sources.
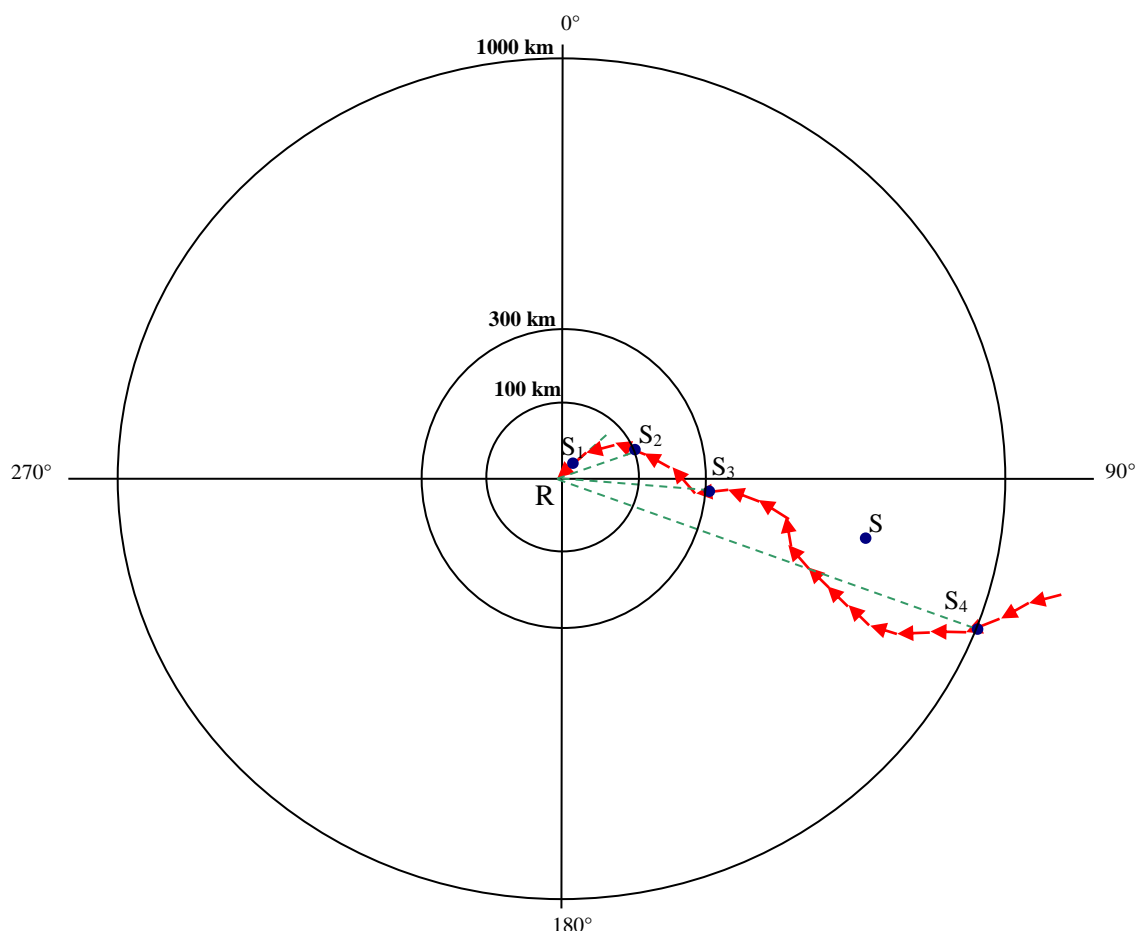
Figure 1.4   *Classification of trajectories in terms of source−receptor distance and source−receptor direction. Receptor R located in the origin. METPRO characterises representative sources S_i (i = 1,4) by transport distance d_i (= 0, 100, 300, 1000 km) and source-receptor angle φ_i (angle between North and dashed line). Note that φ_i is the angle of the average of all wind vectors between S_i and R. For a source S as shown here, OPS interpolates all relevant parameters between classes corresponding with distances d_3 and d_4 and angles φ_3 and φ_4 .*

The local scale represents situations where changes in meteorological conditions during transport are assumed to play no important role. This is usually within 1 or 2 hours after a substance is released into the atmosphere or within 20 km from the point of release. The 1000 km trajectory represents the long-range transport of pollutants with 2-4 days transport time. For most substances the contribution of sources in this range is only 5-10 % (for Western Europe). Statistical properties of trajectories (direction, speed, height) in this range appear to be less sensitive to trajectory lengths, so the properties of these trajectories are also used for transport distances greater than 1000 km. The trajectory of 300 km long is chosen such

that it covers a full diurnal cycle in meteorological parameters, of which the mixing height is the most important. The 100-km trajectory represents transport on a sub-diurnal time scale as an intermediate between the local-and regional-scale transport. Within the 100 km trajectory, transitions in atmospheric stability and mixing height due to night-day transitions occur frequently.

To describe the transport from a source located in a certain wind sector, average properties for all trajectories passing the source area are introduced. An important parameter is the effective path ratio, fp_{eff}, which is calculated for all four distances considered. This parameter represents the ratio between the length of the (curved) path, x_{path}, followed by an air parcel and the straight source-receptor distance x_{sr} :

$$fp_{eff} = x_{path} / x_{sr}. \tag{1.1}$$

The length of the curved path is computed by means of a time-stepping algorithm that takes into account changes in wind speed, wind direction and mixing height during the transport from source to receptor. Individual values for fp_{eff} range from 1 to 3, with a mean value for the 1000-km trajectory of 1.25. This parameter largely determines the effect of removal processes on concentrations under stagnant conditions. For distances larger than 1000 km, an extrapolation is used for fp_{eff} (see Figure 1.5).
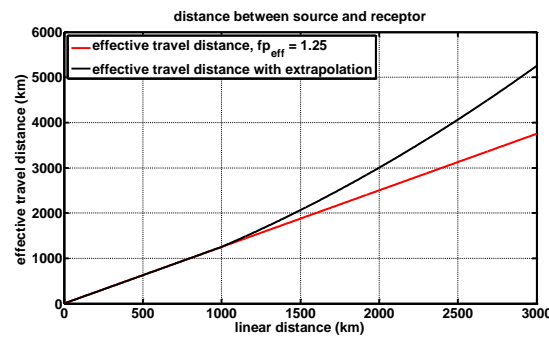
Figure 1.5 Effective travel distance as function of linear distance between source and receptor. In red the effective travel distance using as an example fp_{eff} = 1.25, in black the effective travel distance as computed in OPS, using an extrapolation for distances above 1000 km.

1.3.3 Vertical stratification

Many meteorological parameters show a strong diurnal variation, especially in summertime. This variation is induced by the diurnal cycle in incoming solar radiation, which heats the earth's surface, causing convective turbulent mixing in the lower atmosphere. The variation in the mixing height ranges from about 50 m during nights with a very stable atmosphere, to about 2000 m for days with an unstable atmosphere. The influence of the height of the mixing layer on concentrations is large, since the mixing height actually determines the mixing volume for the material released, especially for larger down-wind distances. An example of the vertical structure of the atmosphere during a three-day period, as it is perceived by the OPS model, is given in Figure 1.6. The behaviour of plumes from high sources with respect to the mixing layer height is also shown.
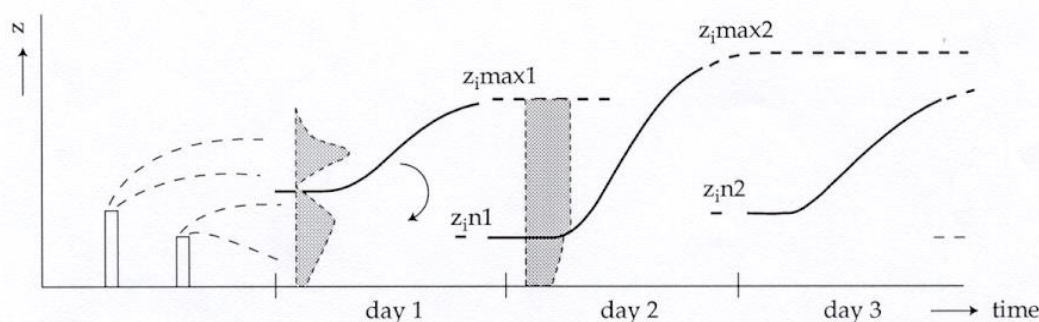
Figure 1.6 Schematic view of the vertical structure of the lower atmosphere as used in the model. The shadowed areas show the vertical concentration distributions at different transport phases. See text below for explanation.

Material released above the mixing layer in the early hours of day 1 will not reach the surface. The vertical dimension of the plume remains small due to absence of turbulence at that height and time (night). A few hours later, the stable night-time situation breaks up when the sun starts to heat the surface again. The plume will then come under the influence of ground-based turbulent movements, which will rapidly mix the plume up through the growing mixing layer. In the late afternoon of day 1, the solar energy reaching the surface will diminish and the convective mixing will stop. The vertical distribution of material at that moment will be considered 'frozen' by the model; while, at the same time a ground-based inversion layer is assumed to be generated. Material under this night-time inversion layer is subject to dry deposition during the night, while material above this layer is not. In the morning of day 2, the contents of the two layers will be re-mixed when the mixing height rises above the maximum level, $z_{i,max1}$, of the day before. If one considers the situation at the end of day 2, it can be said that the material released during the early hours of day 1 is mixed in a layer, $z_{i,max2}$. Local low-level sources, however, will emit at that moment into a layer with height, $z_{i,n2}$. In conclusion, contributions to a receptor from local sources must be calculated using local mixing heights. Contributions from sources far away must be calculated using the maximum mixing height that occurred during transport from the source to the receptor.

1.3.4 Classification with respect to the vertical structure of the boundary layer

To include the effects of different vertical stratifications in the atmosphere, mixing-height classes are used, over which trajectories are distributed according to the maximum mixing height found during transport from source to receptor. The initial plume height in relation to the mixing height determines whether or not a plume will touch the ground shortly after release. Both parameters are a function of the stability at the source site. Therefore, the chosen classification is a combination of stability at the source and maximum mixing height over the trajectory. To account for stability and mixing height effects, 3 classes for stability and 2 classes for mixing height are taken. The criteria for the classes are given in Table 1.1. The atmospheric stability is defined here on the basis of the Monin-Obukhov length. The mixing-height criteria are chosen such that for the range of seasonal variations a reasonably even occurrence of all classes is obtained.

Table 1.1 Criteria for the atmospheric stability, mixing height and transport distance classes. U, N, S stand for Unstable, Neutral and Stable; the indices 1 and 2 denote relatively low and high mixing height respectively.

Class	Atmospheric stability	Monin-Obukhov length L (m)	Trajectory: 0 km	Trajectory: 100 km	Trajectory: 300 km	Trajectory: 1000 km
			Maximum mixing height over trajectory (m)			
U1	Unstable	$L < 0$ [(1)]	< 500	< 800	< 900	< 1000
U2			≥ 500	≥ 800	≥ 900	≥ 1000
N1	Neutral	$L > 100$ [(1)]	< 400	< 400	< 500	< 800
N2			≥ 400	≥ 400	≥ 500	≥ 800
S1	Stable	$0 < L < 100$	< 80	< 150	< 400	< 800
S2			≥ 80	≥ 150	≥ 400	≥ 800

[(1)] the reason that L < -100 is put into the classes U1 or U2 and not into one of the neutral classes, is that we do not want to average out very large positive and very large negative Monin-Obukhov lengths.

This classification scheme for the vertical structure of the boundary layer offers the opportunity to account for source-height effects and temporary transport above an inversion layer. The scheme differs from the one used in earlier versions of the model (Van Jaarsveld, 1990), where the atmospheric stability (Pasquill classification) was determined on the basis of surface-roughness length and Monin-Obukhov length according to Golder (1972).

The development of the maximum mixing height for surface-released air pollutants as a function of down-wind distance is shown in Figure 1.7 for different initial conditions.
The curves in this figure are calculated on the basis of 10-year meteorological data in the Netherlands. It can be concluded that elevated plumes (e.g. 250 m) emitted under stable conditions (classes S1 and S2) remain above the mixing layer for more than 100 km on average. This figure also shows that mixing heights at intermediate distances can be linearly interpolated from the distance classes used here, without making large errors.
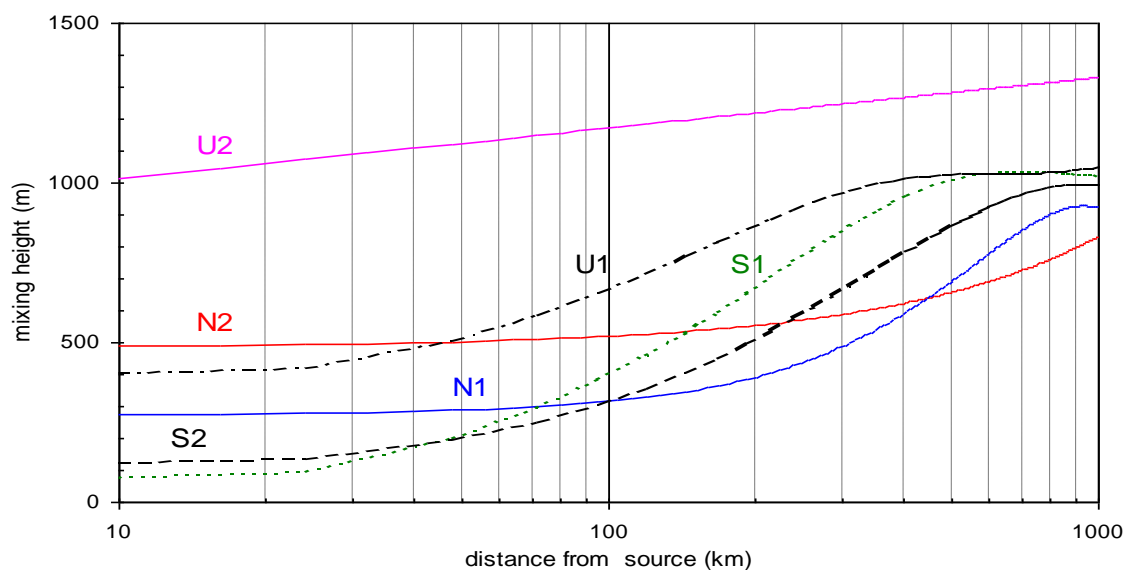
*Figure 1.7 Maximum mixing height, as experienced by an air parcel originally at ground level, as a function of down-wind distance for different stability/mixing height conditions at the moment the air parcel was released. Mixing heights are calculated as described in section **2.4.4** and averaged over a period of 10 years.*

Summing up the total classification scheme used: the horizontal transport from a source (area) to a receptor is determined by parameters related to one of 288 classes (4 distance scales, 12 wind direction sectors and 6 stability/mixing heights). Parameter values needed to describe source-receptor relations at actual distances and directions are obtained by linearly interpolating between the values of adjacent classes. One important disadvantage of the described classification method is that all reactions and conversions which can take place during transport have to be considered as independent from the absolute concentration values. This means that the method is only applicable to reactions which can be approximated as pseudo-first-order reactions.

1.4   References

Calder K.L. (1971) A climatological model for multiple source urban air pollution. Proceedings of the 2nd Meeting of Expert Panel on Air Pollution Modelling. NATO/CCMS. p. I.1-I.33. Report no. 5.

Golder D. (1972) Relations among stability parameters in the surface layer. *Boundary-Layer Meteorol.* **3,** 47-58.

Hoogerbrugge, R and Geilenkirchen, GP and den Hollander, HA and van der Swaluw, E and Visser, S and de Vries, WJ and Wichink Kruit, RJ (2019) Large-scale concentration and deposition maps of the Netherlands: 2019 report. RIVM report 2019-0091 (in Dutch). https://doi.org/10.21945/RIVM-2019-0091
https://www.rivm.nl/publicaties/grootschalige-concentratie-en-depositiekaarten-nederland-rapportage-2019
Also available for other years.

Runca E., Longhetto A. and Bonino G. (1982) Validation and physical parametrization of a Gaussian climatological model applied to a complex site. *Atmospheric Environment* **16**, 259-266.

Stelson A.W. and Seinfeld J.H. (1982) Relative humidity and pH dependence of the vapor pressure of ammonium nitrate-nitric acid solutions at 25 ºC. *Atmospheric Environment* **16**, 993-1000.

Stolk A.P., van Zanten M.C., Noordijk H, van Jaarsveld J.A. van Pul W.A.J. (2009) Meetnet Ammoniak in Natuurgebieden, Meetnetresultaten 2005 – 2007. RIVM Rapport 680710001/2009

Van Jaarsveld J.A. (1990) An operational atmospheric transport model for priority substances; specification and instructions for use. RIVM, Bilthoven, the Netherlands. Report no. 222501002.

Van Jaarsveld J.A. (2004) Description and validation of OPS-Pro 4.1, RIVM report 500045001/2004.

Van Zanten, M.C., F.J. Sauter, R.J. Wichink Kruit, J.A. van Jaarsveld, W.A.J. van Pul (2010) Description of the DEPAC module. Dry deposition modelling with DEPAC_GCN2010. RIVM report 680180001

2. Meteorological data

Air pollution modelling relies heavily on meteorological input data. Processes such as plume rise, dilution, dispersion and long-range transport depend not only on wind speed but also on turbulence characteristics and on the wind field over the area where the pollutant is dispersed. Although parameters such as turbulence may be measured directly in the field, it is not very practical and certainly very expensive. Therefore, most model approaches make a distinction between real observations of primary data (wind, temperature, radiation etceteras) and secondary parameters (friction velocity, Monin-Obukhov length, mixing height etceteras), derived from the set of primary parameters. The OPS model is designed to make use of standard and routinely available meteorological data. The parameters are wind speed and wind direction at two heights, temperature, global radiation, precipitation, snow cover and relative humidity.

2.1   Meteorological districts in the OPS model

The OPS model is intended to describe the local dispersion from specific sources but also the total influence of all relevant sources in Europe on all parts of the Netherlands. This means that - in principle - the meteorological information must be available, along with some spatial detail. For this purpose, six meteorological districts have been chosen, mainly on the basis of the average wind speed regime over the Netherlands. The districts are shown in Figure 2.1.
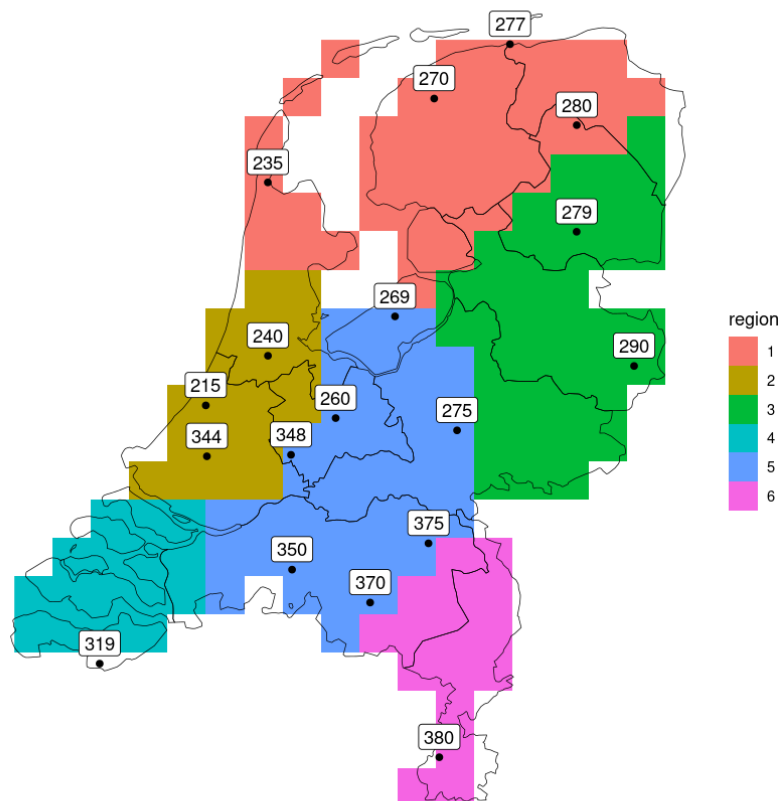
Figure 2.1.   OPS meteorological districts (on a 15 x 15 km grid) and location of KNMI stations.

All meteorological pre-processing is done individually for the six districts and saved separately. A schematic overview of this procedure is given in Figure 2.2. After this processing of the primary data a stage follows, in which secondary parameters are calculated and a climatology of similar situations (classes) is generated.
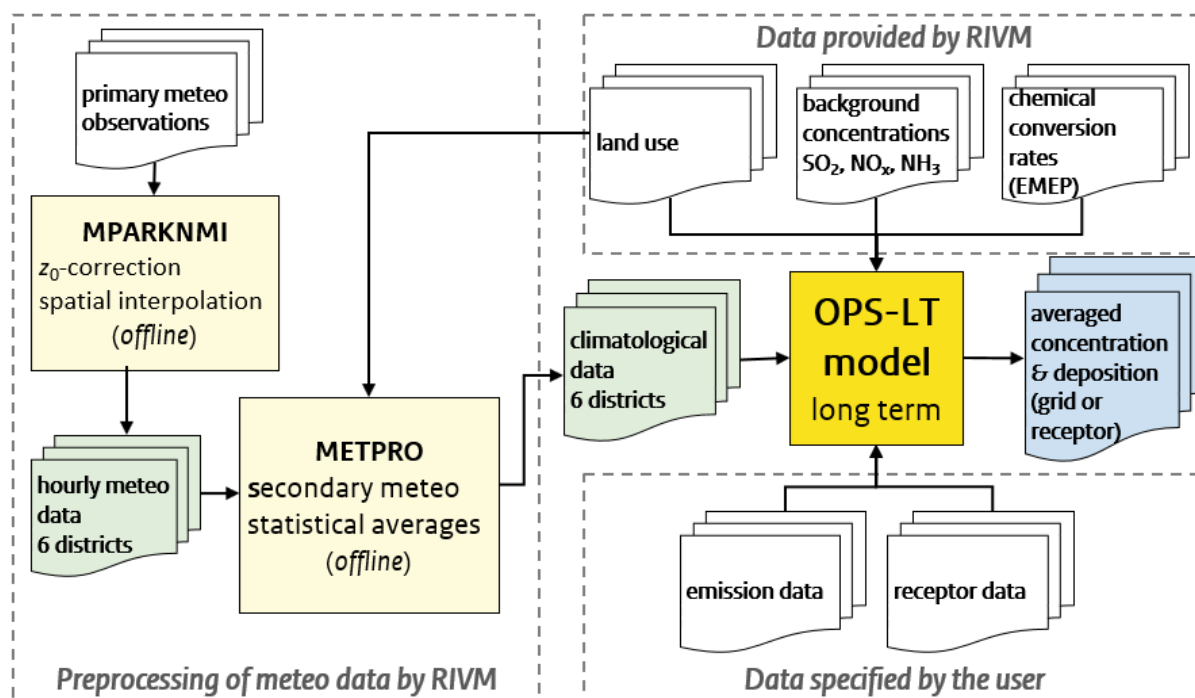
Figure 2.2   Schematic view of the long term OPS model with its pre-processing steps by the programs MPARKNMI and METPRO.

When the OPS model is run, climatological data are loaded from six files, representing six districts. The OPS model interpolates data of three nearest districts, nearest to a receptor, to avoid discontinuities in output.

The purpose of this chapter is to describe the meteorological data and the procedures used to obtain representative values for the different districts.

2.2   Sources of primary meteorological data

Currently, all necessary meteorological input data is obtained from the KNMI. The positions of the selected KNMI meteorological stations are given in Figure 2.1. Detailed information on these stations can be found in section 2.6.

Till 1993, meteorological input data was obtained from the National Air Quality Monitoring Network (LML) database. Between 1976 and 1981, this was mainly wind data measured in the LML network consisting of 46 sites, of which 5 were situated at the top of TV towers. In 1981, the database was expanded with data from the KNMI network on global radiation (7 –17 sites), temperature (14 sites) and precipitation data (11-14 sites). The LML meteorological observations stopped in 1993. From this point on, wind data was also obtained from observations at KNMI stations. Historical wind data, going back to 1981, were obtained from the KNMI archives and also included in the LML database. In this way a homogeneous series of data became available.

2.3   Processing primary data (MPARKNMI)

The primary meteo-preprocessor MPARKNMI reads primary observed meteo data (Table 2.2.1), applies a roughness and height correction for wind speeds, using roughness lengths for each meteorological station, representative for 12 wind sectors of 30°. Then, a spatial interpolation technique is applied, to compute the spatially averaged meteorological parameters that are listed in Table 2.2.2. The averaged parameter is either representative for a "local" scale or a "regional" scale.

The "local" area is defined by the area in which the model is intended to describe the concentration and/or deposition. The local data can be the data of a single station or derived from observations of more stations. In the latter case a representative value has to be determined from the different observations. In general, the local scale is an area with transport length < 50 km.

A "regional" area is a larger area, in principle the whole area from which emissions can influence the air pollution concentration in the local area. For the Netherlands, for example, the regional wind direction is taken as the wind velocity weighted average wind direction of stations over the whole country. Other parameters, such as regional precipitation amount, can simply be obtained by arithmetic averaging of observations in a large area. The regional scale is an area with transport length > 50 km.

If OPS is applied to compute nation-wide concentrations and depositions in the Netherlands, both scales are used: the local scale to define properties at the receptor site, the regional scale to define averaged properties for a trajectory. In this set-up, the local scale parameters are retrieved from the 6 OPS meteo districts, whereas NL averages are used as regional scale parameters.

With respect to certain parameters a single averaged value is used for the whole of the Netherlands (see Table 2.2.2); the main reasons for computing only one value (and not 6 district values) are the following:
- the spatial distribution of the parameter is not very important for the OPS model
- the interpolation to OPS meteo districts is not representative (too much data loss), because few stations are measuring that parameter.

Table 2.2.1 Meteorological parameters and their specifications as input of MPARKNMI. obs. means observation height of KNMI meteo stations.

Parameter	height	Units
temperature	obs.	^{0}C
wind speed	obs.	m/s
wind direction	obs.	degrees
wind speed	200 m	m/s
wind direction	200 m	degrees
global radiation	obs.	J/cm2
precipitation duration	obs.	0.1 h
precipitation intensity	obs.	mm/h
relative humidity	obs.	%

Table 2.2.2 Meteorological parameters and their specifications as output of MPARKNMI. Formats for data derived from hourly KNMI observations.

	Parameter	Scale[3]	Observation height	Units	Format	No data value	required
	once a day :						
a	date (local time)[2]			yymmdd	3i2.2		y
b	snow cover indicator	NL		0=no 1=yes	i2	8	n
c	length of rain events	NL		0.1 h	i4	-88	n
d	precipitation intensity[7]	NL		0.1 mm/h	i4	-88	n
e	precipitation intensity[7]	local		0.1 mm/h	i4	-88	n
	every hour:						
f	global radiation	NL	1.5 m	J/cm^2/h	i4	-88	y
g	temperature	NL	1.5 m	0.1 ^{0}C	i5	-880	y
h	precipitation duration[6]	NL	1.5 m	0.01 h	i4	-88	y
i	precipitation duration[6]	local	1.5 m	0.01 h	i4	-88	y
j	wind direction	NL	200 m[1]	degrees	i4	-88	n
k	wind velocity[4]	NL	200 m[1]	0.1 m/s	i4	-88	n
l	wind direction	NL	10 m	degrees	i4	-88	y[5]
m	wind velocity[4]	NL	10 m	0.1 m/s	i4	-88	y[5]
n	wind direction	local	10 m	degrees	i4	-88	n[5]
o	wind velocity[4]	local	10 m	0.1 m/s	i4	-88	n[5]
p	relative humidity	NL	1.5 m	%	i4	-88	n

[1] 200 m or at a level to be specified

[2] Solar noon is expected to be at 13:00 h

[3] local: average of an OPS meteo district; NL: average of the Netherlands

[4] wind velocity converted to a standard roughness length of 0.03 m

[5] either local (district) or NL data must be available

[6] precipitation duration per hour in 0.01 h = precipitation probability in %

[7] daily averaged precipitation intensity = (amount of rain) / (time during which it rained) [0.1 mm/h]

An overview of MPARKNMI is shown in Figure 2.3.

MPARKNMI
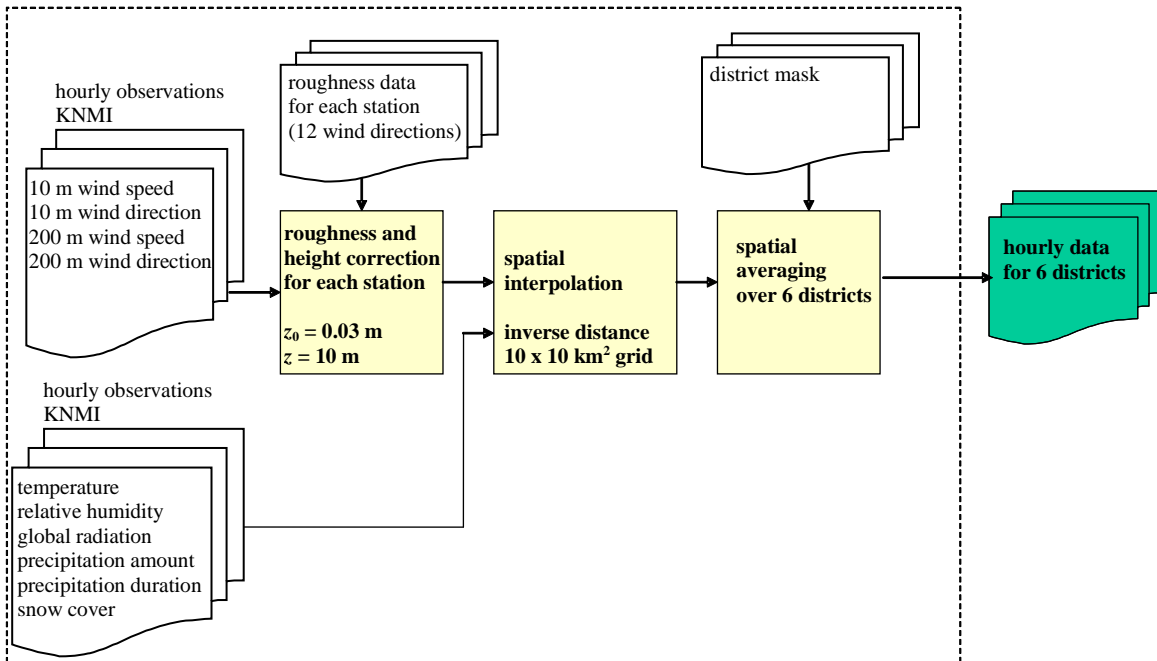
Figure 2.3 Processing of primary meteorological data by MPARKNMI.

2.3.1 Calculating the potential wind speed

The OPS model uses spatially averaged meteorological data rather than point data. Before any form of spatial averaging can take place, it is necessary that all wind data is converted to standard conditions. Not all stations have the same measuring height. Moreover, the terrain conditions are not the same for all the stations. Therefore, wind velocities are converted to a potential wind speed, defined as the wind at 10 m height and at a roughness length of 0.03 m, according to the method described in section 2.4.5.1. Because the roughness length is not the same in all wind directions, conversion is applied as a function of wind direction.

2.3.2 Spatial averaging of meteorological data

The spatial averaging method chosen here is first interpolating the data over the Netherlands, using all the available stations (see Figure 2.1 and Table 2.6) and then calculating district averages. In this way, the data are optimally used and the information of nearby stations is used automatically, if local stations fail. In earlier approaches, a number of stations were selected to be representative for an OPS meteo district. The major drawback of such a method is that, if data sets change, one has to make new selections with the risk of changing trends in the district. Also, the chance that for a given hour none of the selected stations will provide valid information is high, resulting in a high percentage of missing data.

Parameters are interpolated using a 10 x 10 km^2 grid over the Netherlands. Given a set of N observations, the resulting parameter value for a grid cell (k,l) of the grid is:

$$x_{kl} = \frac{\sum_{i=1}^{N} w(i)\, x(i)}{\sum_{i=1}^{N} w(i)} , \qquad (2.1)$$

with $x(i)$: parameter value at station i and $w(i)$: weighing factor for station i, depending on the distance r between the grid point and the position of the measuring station according to:

$$w(i) = \exp\left[\frac{-r}{r_{rep}}\right], \qquad (2.2)$$

Here, r_{rep} is an interpolation distance which, considering the mean distance between the stations, is fixed at 10 km.
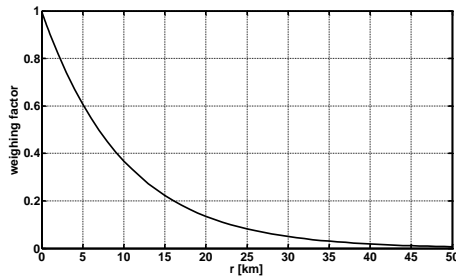
Figure 2.4 Weighing factor as function of distance r.

If the contribution of each station to each grid point has been calculated, then the parameters are spatially averaged to district averages by using a mask according to Figure 2.1.

2.3.2.1 Wind direction
The potential wind speed $\underline{u}$ in combination with the wind direction is split into an u_x and u_y vector and district averages are computed as above for u_x and u_y. The resulting wind direction per district is simply calculated by taking the arctangent of the vectors. If the observations indicate a variable wind direction, the observation is ignored. In such a case, the remaining stations determine the direction of the wind in the district.

2.3.2.2 Wind speed
Spatial averaging of wind speed is done using the same interpolation procedure. Considering the use of wind speed in the model (mainly to derive turbulence parameters), the interpolation is independent of wind direction. The minimum wind speed of individual observations is set at 0.5 m/s. This takes the trigger threshold of the anemometers used into account (in the order of 0.4 m/s) to some extent, and also the fact that wind speed is given in 1 m/s units (before July 1996, wind speeds were specified in knots ≈ 0.5 m/s). Ignoring situations with zero wind speed would introduce a bias in the 'average' wind speed, and therefore will lead to larger errors in modelling than using lower limit values.

2.3.2.3 Other parameters
Interpolation of global radiation, temperature, relative humidity, precipitation duration and precipitation intensity is carried out in the same way as for wind speed. The length of rain events and snow cover are not spatially interpolated, but apply always for the Netherlands as a whole.

2.3.3 Calculation of precipitation characteristics

Precipitation events in the OPS model are described with three parameters:

1. precipitation probability

2. precipitation intensity
3. the average length of a rain event.

In terms of input data for OPS, precipitation probability is required on an hourly basis, while intensity and length of rain event are required as representative values on a daily basis. The KNMI data provide - for each hour - the amount of precipitation and the duration within that hour.

- The hourly precipitation probability (in %) is taken equal to the precipitation duration per hour in 0.01 h.
- The average precipitation intensity for a day is computed as (total amount of rain during a day) / (time during which it rained during a day).
- The average length of a rain event requires a definition of what is considered as a contiguous rain event and what is not. A rain event starts in the first hour in which the precipitation duration is larger than zero and ends if the precipitation duration is zero in a subsequent hour. The length of this event is calculated as the sum of the durations between the starting hour and the ending hour. The average length of a rain event is then calculated as the sum of the lengths of all rain events that end on a certain day divided by the number of rain events that end during that day. This means that precipitation periods that have not yet ended, but continue on the next day, contribute to the average length of a rain event of the next day. A single daily and spatially averaged value is calculated from all the stations that reported precipitation that day.
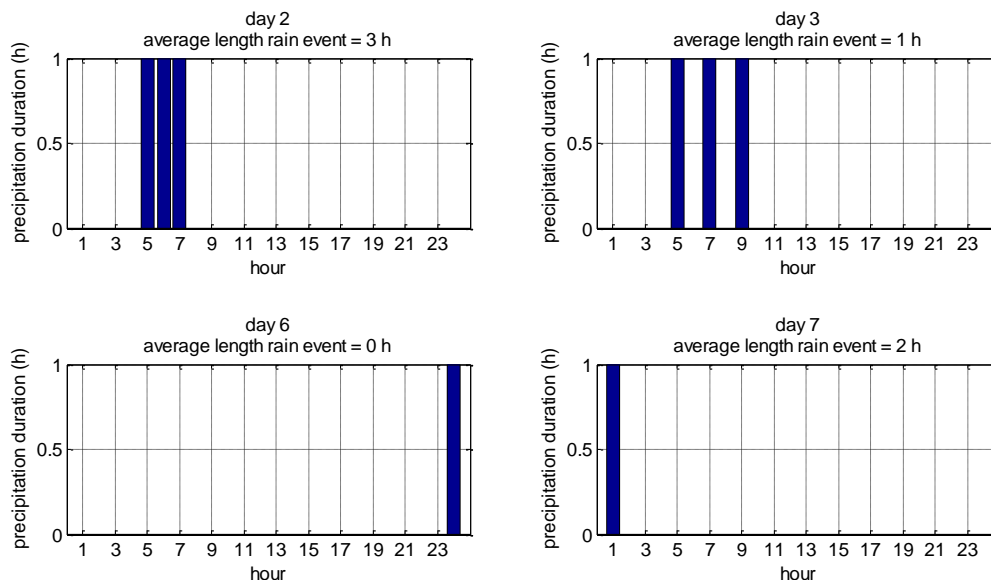
Figure 2.5 Average length of rain event = 3h, for contiguous 3-hour rain (upper left); = 1 h, for 3 separate 1-hour rain events (upper right); = 0h, for a rain event which extends to the next day (lower left); = 2 h, for two hour rain extending over two days (lower right).

2.3.4 Determination of the snow cover indicator

The presence of a snow cover is important for the calculation of dry deposition velocities in the model. If the Netherlands and a large part of Europe are covered with snow, the dry deposition will decrease dramatically and the long-range transport of pollutant may increase sharply. As such, the model focuses on the large-scale effects of snow cover and not on the local scale. The input to the model is therefore an indicator of whether most of the Netherlands (and probably Western Europe) is covered with snow or not. The height of a snow layer is reported by 3-7 stations on a daily basis (see Table 2.7). The snow indicator is set at 1, if at least 80% of these stations report the presence of a snow layer. From 2003 onwards, there are no snow cover data available in the LML database and OPS will overestimate the deposition during large scale snow periods, especially for water soluble species.

2.4   The meteorological pre-processor (METPRO)

The task of the pre-processor METPRO is to calculate secondary meteorological parameters, construct backward trajectories, divide these trajectories into classes and calculate representative averages for a number of parameters. Trajectory distance classes account for the time difference between source and receptor; f. ex. for a distance of 1000 km, there may be several days between the meteorological situation at the source and that at the receptor. METPRO averages meteorological parameters for these distance classes, meaning that averaging takes place over time (over all hours that the plume travels between source and receptor), not over the actual space where the trajectory lies.

The mixing height classes in OPS ('low' and 'high' mixing height) do not contain a single fixed value for the mixing height, but contain averages derived from the actual hourly values in the selected simulation period. This approach ensures a non-critical choice of class boundaries. The main processes in METPRO are shown in Figure 2.6.

METPRO

Hourly loop

Read meteo data and compute secondary meteoparameters (stability parameters, mixing height, …)

Loop over trajectory classes, i.e. distances 0, 100, 300, 1000 km

Compute trajectory (effective distance, direction) and averaged meteo and deposition parameters along a trajectory

Determine the classification of this trajectory in terms of wind direction and stability/mixing height

Add data to current distance, wind direction, stability/mixing height class

Compute parameter averages and frequencies for each class

Figure 2.6 Flow chart of meteo preprocessor METPRO.

2.4.1 Cloud cover

We follow the procedure from Holtslag and van Ulden (1983b). During daytime, the solar elevation φ is computed, depending on the latitude of the location; in OPS the location of De Bilt (latitude 52°) is used. Then the global radiation for cloudless skies [W/m^2] is computed according to Kasten and Czeplak (1980) and Collier and Lockwood (1974, 1975):

$$Q_{clear\,sky} = a_1 \sin(\varphi) + a_2,$$
(2.3)

with

$Q_{clear\,sky}$: clear sky radiation [W/m^2]

a_1 and a_2 empirical constants, $a_1 = 1041$ W/m^2, $a_2 = -69$ W/m^2.

Kasten and Czeplak (1980) give a relation between the measured radiation $Q_{measured}$ [W/m^2] and the clear sky radiation as function of cloud cover N [-]:

$$Q_{measured} = Q_{clear\,sky}\left(1 + b_1 N^{b_2}\right),$$ (2.4)

with
$b_1 = -0.75$, $b_2 = 3.4$ empirical coefficients. From this we can compute the cloud cover:

$$N = \left[\frac{1}{b_1}\left(\frac{Q_{measured}}{Q_{clear\,sky}} - 1\right)\right]^{\frac{1}{b_2}}.$$ (2.5)

During night time, a cloud cover is used equal to 0.9 x cloud cover of two hours before dusk, assuming that we have fewer clouds in the night than before dusk. We do not want to use the cloud cover of 1 hour before dusk, since at dusk measurements of global radiation may be very low and unreliable.
Cloud cover is an input for the scheme of Beljaars and Holtslag, described in the next section.

2.4.2 Derivation of boundary layer parameters

The calculation scheme of Beljaars and Holtslag (1990) is used for the estimation of boundary layer parameters such as surface heat flux, friction velocity and Monin-Obukhov length. Most of the routines in this scheme are based on a parameterization of day and night-time surface energy budgets as published by Holtslag and Van Ulden (1983a); Van Ulden and Holtslag (1985) and Holtslag and De Bruin (1988).
The Monin-Obukhov length L [m] is a vertical length scale, which has become very popular in estimating the stability of the atmosphere. $-L$ reflects the height to which friction forces are dominant over buoyant forces. The surface heat flux, H_0 [W m^{-2}], is the vertical flux of sensible heat that is transferred by turbulence to or from the surface. This parameter determines the heating or the cooling of the lower part of the boundary layer and therefore indirectly affects the depth of the boundary layer. The friction velocity u_* [m/s] determines the production of turbulent kinetic energy at the surface. The relation between L, H_0 and u_* is given by:

$$L = -\frac{T\,\rho_a\,c_p\,u_*^3}{g\,H_0\,\kappa},$$ (2.6)

where κ [-] is the von Kármán constant, established experimentally to be about 0.40, T the absolute temperature [K], g the acceleration of gravity [m s^{-2}], c_p the specific heat of air [J kg^{-1} K^{-1}], and ρ_a the air density [kg m^{-3}]. H_0 can be calculated from the net radiation Q^* [W m^{-2}] using the surface energy budget:

$$H_0 + LE = Q^* - G_s,$$ (2.7)

where LE is the latent heat flux and G_s the soil heat flux. The latent heat flux is modelled by De Bruin and Holtslag (1982), and Holtslag and De Bruin (1988), using a modified Priestly-Taylor model. This model is used in the routines of Beljaars and Holtslag (1990), where H_0 for a given geographical position is parameterized as a function of global radiation or cloud cover. Results of these surface energy parameterizations have been verified with experiments at the Cabauw meteorological tower. The basic equation which, according to surface-layer similarity theory, relates u_* to a vertical wind speed profile $u(z)$ is:

$$u_* = \frac{\kappa\,u(z)}{\ln(\frac{z}{z_0}) - \psi_m(\frac{z}{L}) + \psi_m(\frac{z_0}{L})},$$ (2.8)

where z is an arbitrary height in the surface layer, z_0 the surface layer roughness length of the terrain (for a classification, see Wieringa (1981)). The functions ψ_m, are stability correction functions for momentum, which read as follows (Paulson 1970, Holtslag 1984):

for $z/L < 0$:

$$\psi_m(\frac{z}{L}) = 2 \ \ln \ (\frac{1+x}{2}) + \ln \ (\frac{1+x^2}{2}) - 2 \ \arctan(x) + \frac{\pi}{2}$$
$$\text{with} \quad x = (1 - 16 \ \frac{z}{L})^{1/4}$$

(2.9)

for $z/L > 200$:

$$\psi_m(\frac{z}{L}) = -0.7\frac{z}{L} - 10.72$$

(2.10)

for $0 \leq z/L \leq 200$:

$$\psi_m(\frac{z}{L}) = -0.7\frac{z}{L} - (0.75\frac{z}{L} - 10.72) \cdot \exp(0.35\frac{z}{L}) - 10.72 \ .$$

(2.11)

Equations (2.6)-(2.11) are iteratively solved to obtain u_* and L (Beljaars and Holtslag, 1990). The following minimal values are imposed: $|L| = 5$ m, $u_* = 0.04$ m/s.

From Eq. (2.8) relations can be derived for wind speed profile calculations or for the translation of wind speed observations to situations with different z_0. In section 2.4.5 more details on the wind speed profile and stability correction functions are given.

2.4.3 Pasquill classes

Pasquill (1961) categorised the amount of atmospheric turbulence in 6 classes, ranging from A (strongly unstable) to F (strongly stable). In the OPS-model other measures of atmospheric turbulence are used; however Pasquill classes are still used in OPS, but only for two purposes:
- for the computation of the turning of the wind with height (here we use the eddy diffusivity K_m, see section 2.4.5.3)
- for the plume rise that is used in computing effective dry deposition velocities (see eq. 2.25).

The Pasquill class is determined as a function of the inverse Monin-Obukhov length $1/L$ and the roughness length z_0, according to Golder (1972), see Figure 2.7.
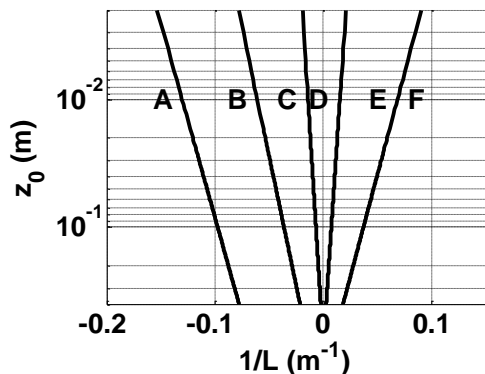

Figure 2.7   *Pasquill classes as function of roughness length z_0 and Monin-Obukhov length L, according to Golder (1972).*

Table 2.2.3 Pasquill classes and corresponding Monin-Obukhov length L [m] and eddy diffusivity of the boundary layer K_m [m²/s]

Pasquill class	characterisation	range of L for $z_0 = 0.1$ m	K_m [m²/s]
A	strongly unstable	[-10, 0]	50
B	unstable	[-28, -10]	40
C	weakly unstable	[-147, -28]	30
D	neutral	[-∞, -147], [135, ∞]	10
E	stable	[27, 135]	3
F	strongly stable	[0, 27]	1

The following adaptations have been implemented in order to remain more closely to the classification of the Dutch National model (TNO, 1976):

$Q^* \leq 0$ W/m², A-D   → D
$Q^* > 0$ W/m², E-F   → D
N > ⅝   → D
E-F, v > 3 m/s, N > ⅜   → D
$Q^* \leq 0$ W/m², 2 m/s < v ≤ 3 m/s, ⅜ < N < ⅝ → E.

2.4.4 Estimation of mixing heights

Although it was possible, in principle, to use temperature profiles from radio soundings for the determination of the mixing layer height, estimation of the mixing height on the basis of surface-layer parameters was preferred. The main reason for this is that the inversion height is usually taken at the height of the dominant temperature jump in the profile, so is valid for 'aged' pollutants, while this model needs the height of the first layer starting at the surface that effectively isolates the surface layer from higher parts of the boundary layer. Moreover, temperature profiles from radio soundings have a limited resolution in the lower boundary layer (Driedonks, 1981).

2.4.4.1 Stable and neutral conditions

Strictly speaking, the nocturnal boundary-layer height is not stationary (Nieuwstadt, 1981). Proposed prognostic models usually take the form of a relaxation process, in which the actual boundary-layer height approaches a diagnostically determined equilibrium value. It turns out that the time scale of the relaxation process is very large and therefore the equilibrium value can be used as an estimator for the actual boundary-layer depth (Nieuwstadt, 1984). For this reason the direct applicability of diagnostic relationships was evaluated. A simple diagnostic relation of the form:

$$z_i = c_1 \frac{u_*}{f_c},$$
(2.12)

as first proposed by Delage (1974), was found to give satisfactory results for both stable and neutral atmospheric conditions. In this equation f_c is the Coriolis parameter and c_1 a proportionality coefficient. From the data set of night-time acoustic sounder observations at Cabauw (Nieuwstadt, 1981), c_1 was estimated at 0.08. Equation (2.12) was also tested using acoustic sounder observations carried out at Bilthoven in 1981 during daytime. Values for c_1 found were 0.086 during neutral atmospheric conditions and 0.092 for neutral + stable cases. For the present model Eq. (2.12) is adopted, with $c_1 = 0.092$ for both neutral and stable cases.

2.4.4.2 Unstable conditions

Adequate diagnostic equations do not exist for the depth of the unstable atmospheric boundary layer (Van Ulden and Holtslag, 1985). It is common practice to use rate equations (Tennekes, 1973; Stull, 1983) for describing the rise of an inversion by buoyancy as well as by mechanical forces. The model adopted here is based on the model of Tennekes (1973) and describes the growth of the convective boundary layer for a rather idealized situation. More details on this approach are given in Van Jaarsveld (1995). In Figure 2.8, model results and observations are compared as a function of time of the day for the ten-day data set of Driedonks (1981) and with LD-40 cloud ceilometer data for two days in 2014 (Dammers et al., 2017). Towards the end of the day the algorithm of the LD40 measurements does not register the collapse of the boundary layer which is visible in the simulated data. No systematic difference is observed in the average course of the mixed-layer height. Considering the way mixed-layer heights are used in the OPS model, namely, as averages for typical situations, one can conclude the current approach to lead to the desired results.
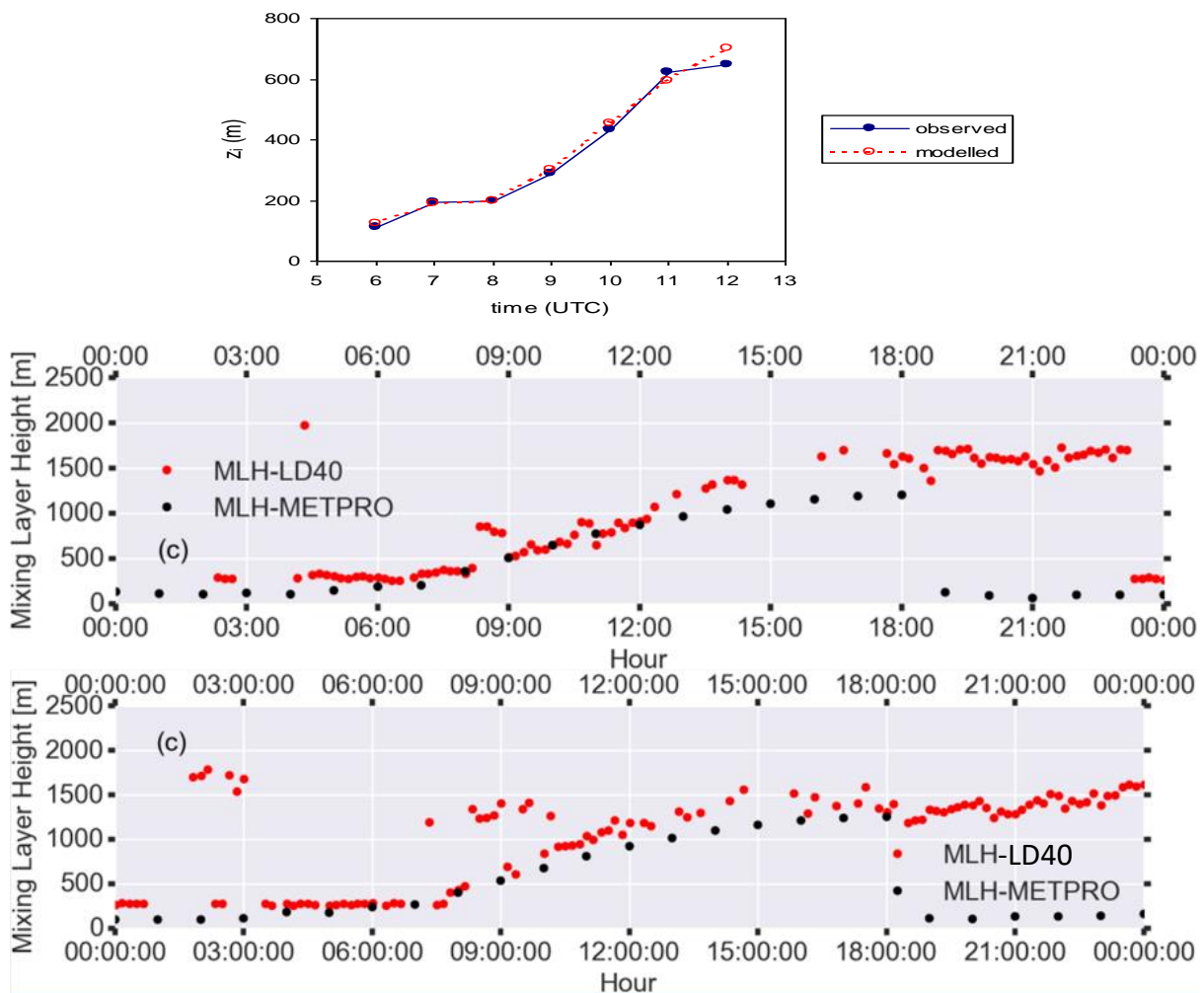

Figure 2.8   *Comparison of modelled and observed mixing-layer heights at Cabauw. Top panel: average of ten convective days, Driedonks (1981). Lower two panels from Dammers et al. (2017); middle panel: July 22, 2014, bottom panel: July 23, 2014.*

2.4.5 The wind profile

Pollutants are emitted at various heights in the atmosphere. Moreover, due to turbulent mixing, the effective transport height of a pollutant may change in time. Wind speed data are usually available for one or two discrete observation levels. What is needed for the description of dispersion and transport of pollutants is a relation between wind speeds at different heights. It is common practice to base this relation for the lower boundary layer on Monin-Obukhov similarity theory. The following general expression for the wind speed at height z can be derived from Eq. (2.8):

$$u(z) = u(z_1) \frac{\left[\ln(\frac{z}{z_0}) - \psi_m(\frac{z}{L}) + \psi_m(\frac{z_0}{L}) \right]}{\left[\ln(\frac{z_1}{z_0}) - \psi_m(\frac{z_1}{L}) + \psi_m(\frac{z_0}{L}) \right]}, \tag{2.13}$$

where z_1 is the height at which a wind observation is available. The functions ψ_m given by Eq. (2.9) - (2.11) are, strictly speaking, only valid for the surface layer $(z_0 << z < |L|)$. However, several authors have derived correction functions describing the wind speed relation up to the top of the mixing layer (Carson and Richards, 1978; Garratt *et al*., 1982; Holtslag, 1984; Van Ulden and Holtslag, 1985). A function which in combination with Eq. (2.13) fits the wind speed observations at the Cabauw tower in stable situations up to 200 m well, is (Holtslag, 1984):

$$\psi_m(\frac{z}{L}) = 2 \ln(\frac{1+x}{2}) + \ln(\frac{1+x^2}{2}) - 2 \arctan(x) + \frac{\pi}{2}, \quad L \le 0 \tag{2.14}$$

$$\text{with} \quad x = (1 - 15 \frac{z}{L})^{1/4},$$

$$\psi_m(\frac{z}{L}) = -17 \left[1 - \exp(-0.29 \frac{z}{L}) \right], L > 0. \tag{2.15}$$

This function is used in the model instead of Eq. (2.9) – (2.11) in computing the wind profile, where it should be noted that for $L \le 0$, the terms $\psi_m(z_0/L)$, present in Eq. (2.8), have been dropped because they are comparatively small.
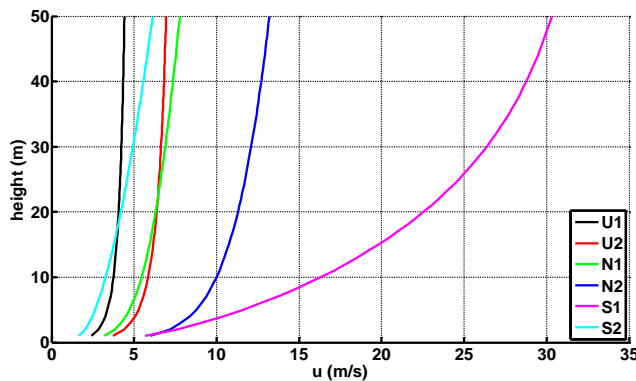
Figure 2.9   *Vertical wind profile computed with eq. 2.8 for* the stability/mixing height classes used in OPS. Values of u^*, L are from *Table 2.5*, $z_0 = 0.03$ m.

.

2.4.5.1 Combining wind observations

An expression similar to Eq. (2.13) can be derived from (2.8) to translate $u(z;z_0)$ measured at measuring height z at a location with roughness z_0 to a potential wind speed $u(z_1;z_0'')$ at a reference level z_1 (= 10 m) representative for a reference $z_0'' = 0.03$ m. The procedure is to convert $u(z;z_0)$ to $u(z_2;z_0)$ (z_2 taken 60 m) and then to convert $u(z_2;z_0'') = u(z_2;z_0)$ to $u(z_1;z_0'')$. The assumption in this is that the wind speed at height z_2 is not influenced by the local surface roughness.
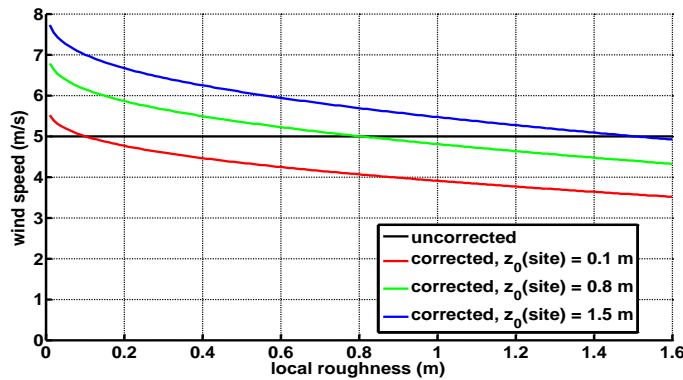
Figure 2.10   Roughness length correction for wind speed, assuming a wind speed of 5 m/s, for three different roughness lengths at the observation site.

This procedure is carried out for each of the observation sites. Roughness lengths for each of the KNMI meteorological sites have been determined by Erisman (1990), using a relation between z_0 and the (short-term) standard deviation of wind directions given by Hanna (1981).

A representative wind speed for a district is calculated in the pre-processor by first normalizing the wind speeds at the different observational sites on the basis of an area-representative roughness length, and then averaging the roughness corrected wind speeds. A representative wind direction follows from the combined x and y components of the roughness-corrected wind vectors.

2.4.5.2 Observed wind speed profiles

Although the logarithmic profile appears to fit observations well, it is used in the present model mainly for extrapolation to levels lower than the observation height (10 m). For the description of (horizontally averaged) transport velocities at different heights (up to 300 m) a relation of the form:

$$u(z) = u(z_1) \left(\frac{z}{z_1} \right)^p ,$$
(2.16)

known as the power law, is used. The major advantage of this relation is that it can be easily fitted to observations. In the present case, p is derived hourly from the 10 m and 200 m observations at the Cabauw meteorological tower. The resulting p values range from 0.13 under unstable conditions ($L > -30$ m) to 0.45 under very stable conditions ($L < 35$ m).

2.4.5.3 Turning of the wind with height

The direction of the wind as a function of height is important for the description of pollutant transport especially if this is done on the basis of surface-based observations. The turning of the wind in the 20 - 200 m layer was studied by Holtslag (1984) and Van Ulden and Holtslag (1985) on the basis of observations at the Cabauw tower. The latter authors give an empirical relation for $A(z)$, the turning angle at height z relative to the surface wind direction, up to 200 m:

$$A(z) = c_6 A(z_{ref}) \left[1 - \exp \left(-c_7 \frac{z}{z_{ref}} \right) \right] ,$$
(2.17)

where $A(z_{ref})$ is the turning angle at reference height z_{ref} ; $c_7 = 1.0$ is an empirical coefficient, c_6 is chosen such that for $z = z_{ref}$, $A(z) = A(z_{ref})$ or $c_6 = 1/(1-\exp(-c_7)) = 1.58$. METPRO provides values of $A(z_{ref})$, based on measurements at the Cabauw tower in the period 1990 – 1996. Typical values of $A(z_{ref})$ at $z_{ref} = 200$ m are 35, 12 and 9 degrees for stable, neutral and unstable situations, respectively.

In METPRO, a trajectory is characterized by a single direction representative for mass flow of the pollutant. This direction is taken at a height equal to half of the maximum mixing height (100-2000 m) of the trajectory. The turning angle above the 150 – 300 m layer is not known from actual observations. On the assumption that the winds become geostrophic at some level above the observation height, an analytical description of the spiral given by Businger (1982) is used:

$$U_g = G\left[1 - \exp(-a_E z)\cos(a_E z) \right] \tag{2.18}$$

$$V_g = G\left[\exp(-a_E z)\sin(a_E z) \right], \text{with } a_E = \sqrt{\frac{f_c}{2K_m}}, \tag{2.19}$$

where K_m is the (bulk) eddy diffusivity of the boundary layer and U_g and V_g the respective velocity vectors in the x and y directions, with the x-axis aligned with the geostrophic wind G. From Eqs. (2.18) and (2.19) the following expression has been derived for the turning angle $A_E(z)$ of the wind at height z relative to the geostrophic wind direction:

$$A_E(z) = \arctan\left[\frac{-\exp(-a_E z)\sin(a_E z)}{1 - \exp(-a_E z)\cos(a_E z)} \right]. \tag{2.20}$$
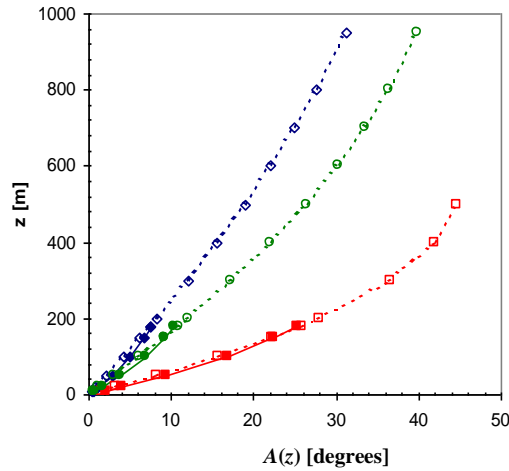
Figure 2.11   Turning of the wind direction with height (Ekman spiral) as a function of height for different stability regimes; A(z) = turning angle relative to the surface wind direction (Eq. 2.20). Results, up to 200 m, obtained using the empirical relation of Van Ulden and Holtslag (Eq. 2.17) are also plotted (solid lines). Red squares: stable conditions ($K_m = 1.5\ m^2\ s^{-1}$; A(z_{ref}) = 27°). Green circles: neutral conditions ($K_m = 11\ m^2\ s^{-1}$; A(z_{ref}) = 11°). Blue diamonds: unstable conditions ($K_m = 25\ m^2\ s^{-1}$; A(z_{ref}) = 8°).

Although the Ekman spiral and Eqs. (2.18) and (2.19) are defined for steady-state situations with small K_m, when using higher eddy diffusivity values, the resulting profiles do not appear to conflict with (mean) profiles, as observed in the lower part of the boundary layer. This is shown in Figure 2.11, where three profiles representative for stable, neutral and unstable conditions in the lower boundary layer are given, together with corresponding profiles, for the lower 200 m, calculated using Equation (2.17). Note that in this figure the turning angle $A(z)$ is plotted relative to the surface wind direction ($A(z) = A_E(z) - A_E(z=0)$) instead of relative to the geostrophic wind.

In the OPS model, the expression of Van Ulden and Holtslag (Eq. (2.17)) is used; for the computation of the trajectories in METPRO, Eq. (2.20) is used, with K_m values from Table 2.2.3.

2.4.6 Trajectories

Backward trajectories are constructed on the basis of hourly wind observations at TV towers. Since at this stage, the actual location of a receptor is not yet known, it is necessary to assume that transport directions and velocities representative for the Netherlands are also valid for a larger area at the same time. Although this is a crude assumption, it may still give satisfactory results for longer term average calculations. The main reason for this is that long-range transport is of importance in persistent situations and those with not too low transport velocities. In these situations, the observations in the Netherlands may be expected to be representative for a much larger area.

The procedure is as follows (see Figure 1.4):

- observed data at the towers are combined into a single x and y wind vector pair representative for a height of 200 m using the methods described in section 2.4.5.
- Wind vectors and other parameters, such as mixing height, are stored for the previous 96 hours (four days).
- A trajectory is determined by tracing back the height corrected wind vectors, starting at the most recent hour with observations and going back in time, using wind vectors of previous hours in the process.
- The back tracking is stopped as a circle with a predefined radius (100, 300 or 1000 km) around the starting point is crossed.
- The wind vectors are height-corrected so as to present the representative height of the mass in the trajectory, which is taken at half the **maximum** mixing height encountered at that stage of transport. Since the maximum mixing height encountered is not known beforehand, an iterative procedure is employed, using updated height-corrected wind vectors, each iteration. This iteration stops if the trajectory does not change anymore.
- The start and end positions of this trajectory determine the direction φ of the trajectory. Other characteristic parameters are determined by appropriately averaging hourly observations along the trajectory.

Easterly directions seem to be systematically overpredicted by the method described here, while north-west directions are underpredicted. It is remarkable that for trajectories which fall fully within the observation area of the towers (e.g. 100 km), these discrepancies are also found (not shown here). Similar results were obtained by comparing these trajectories with 6-hourly 850 hPa trajectories provided by the Norwegian Meteorological Institute, although here a systematic deviation of ~ 20° in transport direction is found. This can be explained by the Ekman spiral (the 850 hPa trajectories are approx. 1500 m above the surface). When corrected for this systematic difference, the standard deviation between the two is of the order of 30°.
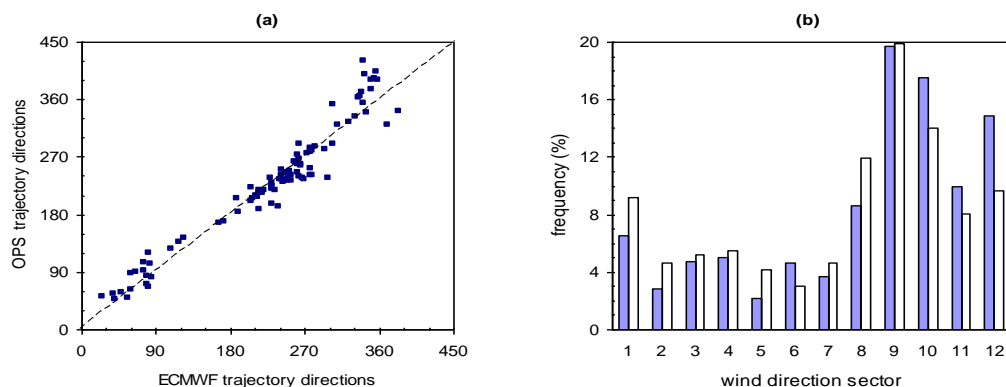
Figure 2.12   Source-receptor directions of backward trajectories derived from ECWMF wind fields versus trajectory directions derived from observations at five towers in the Netherlands. The source-receptor distance was taken as 1000 km. (a): Comparison of individual trajectories arriving at 12:00 UTC, excluding trajectories with $fp_{eff} < 2$. (b): All directions grouped into 30° sectors. Sector 1 represents 345° - 15° (North). Solid bars: ECMWF trajectories. Open bars: OPS trajectories.

In Figure 2.12a, trajectory directions calculated in this way are compared to trajectory directions derived from 3° latitude x 3° longitude resolution wind fields (1000 and 850 hPa) obtained from ECMWF (De Waal and Van Pul, 1995). The latter trajectories are calculated for an average pressure level of 960 hPa (corresponding height above surface ~ 400 m), considered as representative for the average height of transport in the mixing layer. There is hardly any systematic difference between the trajectory directions, as the total set of trajectories is compared. The standard deviation of the differences is of the order of 30° if some much curved trajectories are ignored ($fp_{eff} < 2$, see Eq. 1.1). If directions are grouped into direction classes, then the difference may appear fairly large, as is shown in Figure 2.12b for the full set of trajectories.

Temporal isolation of pollutants from the surface due to mixing-height variations
Due to the classification of trajectories, the properties of the trajectories have to be characterized by a few parameters. In terms of mixing volumes, trajectories are defined by an average transport velocity, u_{tra}, and the maximum mixing height, $z_{i\,max}$, which has appeared during transport. In reality, the mixing height that an air parcel encounters on its way to the receptor point can be lower than this height. Moreover, the parcel may be transported above the mixing layer part of the time. In such a situation, the pollution in the parcel is not removed by dry deposition, a process which only occurs at the surface.
Standard averaging of dry deposition velocities over a trajectory, gives us an average dry deposition velocity

$$\bar{v}_{d\,tra} = \frac{1}{N}\sum_{t=1}^{N} v_d(t),$$ (2.21)

where N is the number of (hourly) intervals and $v_d(t)$ the dry deposition velocity at time t. To account for the effects described above, 'effective' dry deposition velocities ($\tilde{v}_{d\,tra}$) are introduced, which account for the total loss of material on its way from source to receptor and are related to $z_{i\,max}$. The procedure is to follow the air parcel and to integrate the loss of material due to dry deposition, taking into account transport of pollutant mass due to a changing mixing height and keeping track of the mass which is isolated from the surface and does not take part in the deposition process. Mass loss due to deposition is described by the following differential equation:

$$\frac{dM(t)}{dt} = F_d = -v_d(t)C(t) = -v_d(t)\frac{M(t)}{z_i(t)},$$ (2.22)

with $M(t)$: total cross-wind integrated pollutant mass in the mixing layer [g/m²], F_d :deposition flux [g/m²/s], $C(t)$: concentration [g/m³] and $z_i(t)$ the actual mixing height at time t [m].
Integrating over a time step [t, $t+\Delta t$], this differential equation has as solution

$$M(t + \Delta t) = M(t)\exp\left(-\frac{v_d \Delta t}{z_i(t)}\right).$$ (2.23)

Using Eq. 2.23 for successive time steps, the mass at $t = t_{end}$, the total travel time of the trajectory, can be computed. Now the effective dry deposition velocity $\tilde{v}_{d\,tra}$ for the trajectory can be derived from:

$$M(t_{end}) = M(0)\exp\left(-\frac{\tilde{v}_{d\,tra}\, t_{end}}{z_{i\,max}}\right) \Leftrightarrow \tilde{v}_{d\,tra} = -\frac{z_{i\,max}}{t_{end}}\ln\left(\frac{M(t_{end})}{M(0)}\right),$$ (2.24)

where $z_{i\,max}$ is the maximum mixing height over the trajectory.

It is clear that the fraction of the time that pollutants spend above the mixing layer strongly depends on the source height. Therefore the calculation of effective dry deposition velocities is carried out in the pre-processor for two characteristic source heights: a high source (unit strength, 100 m stack height and

plume rise according to Briggs (1975) for a heat content of 20 MW), and a low source (35 m, no plume rise). The latter is representative for sources which always emit within the mixing layer and the former for larger point sources which emit temporarily above the mixing layer.

The effective dry deposition velocities calculated in this way are used in the model in the form of correction factors to the deposition velocity and as such are included in the meteorological data set:

$$f_d(x,h) = \frac{\tilde{v}_{d\,tra}}{\overline{v}_{d\,tra}}, \qquad\qquad\qquad (2.25)$$

where x denotes the source receptor distance and h the source height. f_d has a range of 0.70 - 1.7 with a mean value of 1.2 for the elevated source. For the low source this range is 0.80 - 2.2, with a mean value of 1.4 (sulphur dioxide, 1000 km trajectories). Formally, these correction factors are substance-specific. However, only small differences are found for the usual range of dry deposition velocities. From tests it appears that transport in or above the mixing layer at night explains most of the difference between correction factors for different source heights. The correction factor for low sources is therefore used for non-buoyant plumes up to 100 m.

2.4.7 Summary of the meteorological data set

Table 2.4 gives an overview of the different parameters calculated by the pre-processor, following air parcels from source to receptor at hourly intervals in the period under consideration. Several parameters not yet discussed have been included in the table for reasons of completeness. For every trajectory, representative values for the parameters are determined using parameter-specific averaging methods. The averaging method depends on how the parameter will be used in the model. The trajectories arriving at a receptor during the period considered are distributed over a number of classes, as described in section 0. Average values are calculated for all class – parameter combinations using the same averaging methods. The 4 distance, 12 wind-direction, 3 stability and 2 mixing-height classes for each of the 25 parameters form, collectively, the meteorological data set for the model.

Table 2.4 Parameters calculated by the pre-processor METPRO

	Parameter	unit	A[#]	Remarks
(1)	number of hours that a class has occurred	h	0	
(2)	maximal mixing height over transport distance $z_{i\,max}$	m	1	section 2.4.4
(3)	transport velocity $u(10)$	m/s	1	calculated for $z = z_{i\,max}/2$ and converted to a reference height of 10 m
(4)	boundary layer resistance for SO$_2$ $R_b(SO_2)$	s/m	1	
(5)	aerodynamic resistance at $z = 4$ m + boundary layer resistance $R_a(4) + R_b$	s/m	1	Eq. 5.3 and Eq. 5.7
(6)	aerodynamic resistance at $z = 50$ m + boundary layer resistance $R_a(50) + R_b$	s/m	1	
(7)	deposition correction high sources $f_{d,\,high}$	-	0	Eq. 2.25
(8)	deposition correction low sources $f_{d,\,low}$	-	0	
(9)	effective path length fp_{eff}	m	1	Eq. 1.1
(10)	space heating coefficient	C	0	Eq. 4.1
(11)	rain probability P_p	-	0	derived from hourly or 6-hourly observations: chapter 6
(12)	length of precipitation events τ_w	h	2	
(13)	precipitation intensity R_i	mm/h	2	
(14)	global radiation Q_r	J/cm^2/h	0	measurements
(15)	wind speed power law coefficient P	-	0	section 2.4.5
(16)	surface resistance for SO$_2$ $R_c(SO_2)$	s/m	1	currently not used; R_c values are taken from the DEPAC module in OPS
(17)	percentage of hours that a stability/ mixing height class occurs per 2 hour block, source oriented	%	3	used to manage diurnal emission variations
(18)	percentage of hours that a stability/ mixing height class occurs per 2 hour block, receptor oriented	%	3	used to describe diurnal concentration variations
(19)	friction velocity u_*	m/s	1	section 2.4.2
(20)	temperature T	C	0	measurements
(21)	wind turning with height A	degree	0	section 2.4.5.3
(22)	Monin-Obukhov length L	m	1	section 2.4.2
(23)	sensible heat flux H_0	W/m^2	0	section 2.4.2
(24)	relative humidity	%	0	measurements
(25)	surface resistance for NO$_2$ $R_c(NO_2)$	s/m	1	currently not used; R_c values are taken from the DEPAC module in OPS
(26)	surface resistance for NH$_3$ $R_c(NH_3)$	s/m	1	currently not used; R_c values are taken from the DEPAC module in OPS
(27)	surface resistance for NO$_3$ aerosol $R_c(NO_3)$	s/m	1	from DEPAC module in METPRO

[#] A = averaging method

0: standard averaging within classes

1: reciprocal averaging within classes
- for deposition resistances, this means that we average conductances in m/s
- concentrations are inversely proportional to mixing height and transport velocity

2: standard averaging over rainy hours only

3: no averaging but classification into time-of-day groups

Table 2.5 Some statistical parameter values as a function of the atmospheric stability classes (Data based on KNMI observations over the Netherlands in the period 1990-1999)

Meteorological parameter		Unit	U1	U2	N1	N2	S1	S2	Avg[#]
Frequency of occurrence		%	10	22	18	17	13	20	
Wind speed at 10 m	$u10$	m s^{-1}	2.5	3.9	3.9	6.9	1.3	2.6	2.9
Wind turning 10-200 m	A	degrees	8	0	11	3	27	20	10
Temperature	T	ºC	11	16	9	8	7	8	10
Global radiation	Q_r	W m^{-2}	206	378	20	22	2	3	114
Precipitation probability	P_p		0.041	0.037	0.105	0.202	0.019	0.045	0.077
Precipitation intensity	R_i	mm h^{-1}	1.26	1.53	1.15	1.10	1.06	1.24	1.22
Length of prec. events	τ_w	h^{-1}	1.7	1.5	2.0	2.5	1.7	1.8	2.0
Relative humidity	RH	%	83	67	88	86	92	89	83
Space heating coefficient	stc	ºC	6.6	5.4	10.0	16.2	5.7	8.0	8.7
Sensible heat flux	H_0	W m^{-2}	36	80	-25	-39	-3	-19	6
Friction velocity	u_*	m s^{-1}	0.28	0.43	0.36	0.68	0.53	0.18	0.19
Monin Obukhov length	L	m	-47	-64	196	701	6	32	44
Mixing height	$z_{i\,max}$	m	231	888	290	540	42	146	165
Aerodynamic resistance	$R_a(4)$	s m^{-1}	22	15	21	11	240	46	24
Aerodynamic resistance	$R_a(50)$	s m^{-1}	34	24	45	21	862	133	47

different averaging methods , see Table 2.4.

2.5 References

Beljaars A.C.M. and Holtslag A.A.M. (1990) A software library for the calculation of surface fluxes over land and sea. Environ. Software 5, 60-68.

Briggs G.A. (1975) Plume rise predictions. In: Lectures on Air Pollution and Environmental Impact Analysis. American. Meteorological Society, Boston MA. 59-111.

Businger J.A. (1982) Equations and concepts. In: Nieuwstadt F.T.M. and Dop H. van, editors. Atmospheric turbulence and air pollution modelling. D. Reidel, Dordrecht, the Netherlands.

Carson D.J. and Richards P.J.R. (1978) Modelling surface turbulent fluxes in stable conditions. Boundary-Layer Meteorol. 14, 67-81.

Collier and Lockwood (1974) The estimation of solar radiation under cloudless skies with atmospheric dust, Quart. J. Roy. Met. Sox., 100, 678-681.

Collier and Lockwood (1975) Reply to commentary about the above article, Quart. J. Roy. Met. Sox., 101, 390-392.

Dammers E., Schaap M., Haaima M., Palme M., Wichink Kruit R.J., Volten H., Hensen A., Swart D., Erisman J.W. (2017): Measuring atmospheric ammonia with remote sensing campaign: Part 1 - Characterisation of vertical ammonia concentration profile in the centre of The Netherlands. Atmospheric Environment 169 (2017) 97-112, https://doi.org/10.1016/j.atmosenv.2017.08.067.

De Bruin H.A.R. and Holtslag A.A.M. (1982) A simple parameterisation of the surface fluxes of sensible and latent heat during daytime compared with the Penman-Monteith concept. J. Appl. Meteor. 21, 1610-1621.

De Waal E.S and Pul W.A.J. van (1995) Description of the RIVM trajectory model. RIVM, Bilthoven, the Netherlands. Report no. 722501001.

Delage Y. (1974) A numerical study of the nocturnal atmospheric boundary layer. Q. J. R. Meteorol. Soc. 100, 351-364.

Driedonks A.G.M. (1981) Dynamics of the Well-Mixed Atmospheric Boundary Layer. [PhD thesis]. Royal Netherlands Meteorological Institute, De Bilt, the Netherlands. Scientific report W.R. 81-2.

Erisman J.W. (1990) Estimates of the roughness length at Dutch Air Quality Monitoring Network stations and on a grid basis over the Netherlands. RIVM, Bilthoven, the Netherlands. Report no. 723001003.

Garratt J.R., Wyngaard J.C. and Francey R.J. (1982) Winds in the atmospheric boundary layer - Prediction and observation. J. Atmos. Sci. 39, 1307-1316.

Golder, D.: 1972 Relations Among Stability Parameters in the Surface Layer, Boundary-Layer Meteorology 3, 47-58.

Hanna S.R. (1981) Diurnal variation of horizontal wind direction fluctuations in complex terrain at Geysers, California. Boundary-Layer Meteorol. 21, 201-213.

Holtslag A.A.M. and Ulden A.P. van (1983a) A simple scheme for daytime estimates of the surface fluxes from routine weather data. J. Climate Appl. Meteorol. 22, 517-529.

Holtslag and van Ulden (1983b) De meteorologische aspecten van luvo modellen: eindrapport van het project klimatologie verspreidingsmodellen. WR83-04, KNMI, The Netherlands, http://www.knmi.nl/bibliotheek/knmipubWR/WR83-04.pdf (partly in English).

Holtslag A.A.M. (1984) Estimates of diabatic wind speed profiles from near surface weather observations. Boundary-Layer Meteorol. 29, 225-250.

Holtslag A.A.M. and Bruin H.A.R. de (1988) Applied modelling of the nighttime surface energy balance over land. J. Appl. Meteor. 27, 689-704.

Kasten and Czeplak (1980) Solar and terrestrial radiation dependent on the amount and type of cloud, Solar Energy, 24, 177-189.

Nieuwstadt F.T.M. (1981) The nocturnal boundary layer; theory and experiments [PhD thesis]. Royal Netherlands Meteorological Institute, De Bilt, the Netherlands. W.R. 81 - 1.

Nieuwstadt F.T.M. (1984) Some aspects of the turbulent stable boundary layer. Boundary-Layer Meteorol. 30, 31-55.

Pasquill, F. (1961) The estimation of the dispersion of windborne material, The Meteorological Magazine, vol 90, No. 1063, pp 33-49.

Paulson C.A. (1970) The mathematical representation of wind speed and temperature profiles in the unstable atmospheric surface layer. J. Appl. Meteorol. 9, 856-861.

Stull R.B. (1983) A heat-flux-history length scale for the nocturnal boundary layer. Tellus 35A, 219-230.

Tennekes H. (1973) A model for the dynamics of the inversion above a convective boundary layer. J. Atmos. Sci. 30, 558-567.

TNO (1976) Modellen voor de berekening van de verspreiding van luchtverontreiniging inclusief aanbevelingen voor de waarden van parameters in het lange-termijnmodel. Staatsuitgeverij, the Hague, the Netherlands.

Van Jaarsveld J. A. (1995) Modelling the long-term atmospheric behaviour of pollutants on various spatial scales. Ph.D. Thesis, Utrecht University, the Netherlands

Van Ulden A.P. and Holtslag A.A.M. (1985) Estimation of atmospheric boundary layer parameters for diffusion applications. J. Climate Appl. Meteorol. 24, 1196-1207.

Wieringa J. (1981) Estimation of mesoscale and local-scale roughness for atmospheric transport modelling. In: Wispelaere, C., editor. The 11th Int. Tech. Meeting on air pollution modelling and its application. Plenum Press, New York, 279-295.

2.6 Appendix: meteorological stations

Table 2.6: Overview of KNMI stations from which meteorological data is taken. The local database contains data starting at 1981-01-01 and this 1981 situation is given here.

Station code	Station name	Obs. height (m)	Wind	Global radiation		Rel. hum.	Temp.	Precip. char.	Remarks
				1981	1987				
210	Valkenburg	10						X	
235	De Kooy	10	X	X	X	X	X	X	
240	Schiphol	10	X		X	X	X	X	
250	Terschelling	10							Up to 1990
260	De Bilt	20	X	X	X	X	X	X	
269	Lelystad	10							
270	Leeuwarden	10	X		X	X	X	X	
275	Deelen	10	X		X	X	X	X	
277	Lauwersoog	10							
279	Hoogeveen	10							
280	Eelde	10	X	X	X	X	X	X	
290	Twenthe	10	X		X	X	X	X	
310	Vlissingen	20	X	X	X	X	X	X	
344	Rotterdam	10	X		X	X	X	X	
348	Cabauw	10, 200							1993-1996
350	Gilze Rijen	10	X		X	X	X	X	
370	Eindhoven	10	X		X	X	X	X	
375	Volkel	10	X			X	X	X	
380	Maastricht	10	X	X	X	X	X	X	

Table 2.7: KNMI stations with snow cover data

	210	235	260	270	280	290	310	370	380
1990-1995		x	x		x		x		x
1996-1999		x	x		x				
2000-2002	x	x	x	x	x	x		x	

From 2003, there are no snow cover data available in the LML database.

3. Mass balance and dispersion

3.1   Mass balance equations

The change of a mass M_p [g] over time t [s] for a pollutant in a well-mixed layer due to chemical conversion and deposition can be formulated as follows:

$$\frac{dM_p}{dt} = - k_p\, M_p \tag{3.1}$$

and for a secondary-formed pollutant M_s, with linear dependence on M_p:

$$\frac{dM_s}{dt} = k_c\, M_p - k_s\, M_s\,. \tag{3.2}$$

The rate constants k_p and k_s [s^{-1}] are defined as:

$$k_p = \frac{v_{dp}}{z_i} + k_c + \Lambda_{wp} \tag{3.3}$$

$$k_s = \frac{v_{ds}}{z_i} + \Lambda_{ws}\,, \tag{3.4}$$

where v_{dp} and v_{ds} are dry deposition velocities [m s^{-1}], Λ_{wp} and Λ_{ws} wet scavenging coefficients [s^{-1}], k_c the pseudo first-order chemical reaction constant [s^{-1}], and z_i the mixing-layer height [m]. Subscripts p and s refer to the primary-emitted and the secondary-formed substance respectively. Further chemical reactions involving M_s are not taken into account.

The cross-wind integrated mass flux Q [g s^{-1}] at a distance x [m] from the point of release for a source emitting continuously with a rate of Q_0 [g s^{-1}] can be obtained by solving Eqs. (3.1) and (3.2) after introduction of a horizontal transport velocity u [m s^{-1}] ($u = x/t$):

$$Q_p(x) = Q_0 \exp(- k_p\, \frac{x}{u}) \tag{3.5}$$

$$Q_s(x) = Q_0\, \frac{k_c}{k_p - k_s} \left[\ \exp(- k_s\, \frac{x}{u}) - \exp(- k_p\, \frac{x}{u}) \right]. \tag{3.6}$$
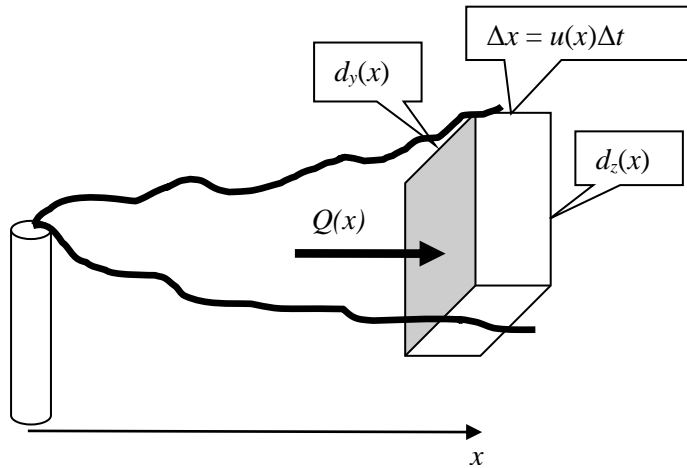
3.2 Dispersion

Figure 3.1   *Mixing volume of plume at distance x, with mass flux Q(x).*

The plume concentration C [g m^{-3}] at a distance x is related to the mass-flux by dividing the mass in the mixing volume (see Figure 3.1) $M(x) = Q(x) \cdot \Delta t$ by the volume with dimensions [m] $\Delta x = u(x)\Delta t$, $d_y(x)$, and $d_z(x)$, the lateral and vertical distance resp. over which the plume has dispersed. This leads to:

$$C(x) = \frac{Q(x)}{u(x)} D_y(x) D_z(x) , \tag{3.7}$$

where $D_y(x)$ and $D_z(x)$ [m^{-1}] represent the lateral and vertical dispersion factor equal to $1/d_y(x)$ and $1/d_z(x)$ resp. The subscripts p and s have been dropped because this and the following expressions are equal for both the primary and the secondary substance. If horizontal transport is assumed to take place in one out of m_s wind direction sectors, then the lateral distance is $\alpha\,x$, with $\alpha = 2\pi/m_s$ the sector angle and it follows that $D_y(x)$ within this sector is given by:

$$D_y(x) = \frac{m_s}{2\,\pi\,x} \tag{3.8}$$

and $D_y(x) = 0$ outside the sector. In the case of a homogeneous vertical distribution of the pollutant in the mixing-layer with height z_i, $D_z(x)$ is simply:

$$D_z(x) = \frac{1}{z_i} . \tag{3.9}$$

For the dry deposition flux $F_d(x)$ [g m^{-2} s^{-1}] we obtain:

$$F_d(x) = -v_d\, C(x) , \tag{3.10}$$

where $C(x)$ and v_d both have to be formally defined for a reference height z above the surface.
The wet deposition flux $F_w(x)$ is defined by:

$$F_w(x) = \frac{Q(x)}{u} D_y(x) \Lambda_w . \tag{3.11}$$

Time-averaged concentration and deposition in a receptor point due to a source at a distance x and in a direction φ is calculated by:

$$\overline{C}(x,\varphi) = \sum_{s=1}^{s_c} \sum_{m=1}^{m_s} \left[\frac{Q(x,s,m)}{u(x,s,m)} D_y(x) D_z(x,s,m)\, f\,(s,m) \right] \tag{3.12}$$

$$\overline{F_d}(x,\varphi) = -\sum_{s=1}^{s_c}\sum_{m=1}^{m_s}\left[\, v_d(s,m)\, C(x,s,m)\, f(s,m)\,\right] \tag{3.13}$$

$$\overline{F_w}(x,\varphi) = \sum_{s=1}^{s_c}\sum_{m=1}^{m_s}\left[\, \frac{Q(x,s,m)}{u(x,s,m)}\, D_y(x)\, \Lambda_w(s,m)\, f(s,m)\,\right], \tag{3.14}$$

where $f(s,m)$ is the distribution function of wind-direction classes m_s and atmospheric stability/mixing height classes s_c for the period over which the averaging has to be carried out. Note that in all the above equations, x refers to the real transport path length and that v_d and Λ_w in Eqs. (3.10) and (3.11) refer to deposition parameters at the receptor site while those in Eqs. (3.3) and (3.4) refer to parameters representative for the total trajectory.

3.3   Vertical mixing close to sources

A serious limitation for models assuming instantaneous vertical mixing in the mixing-layer is that concentrations due to emissions of low-level sources will be underestimated, while the effect of sources emitting at high levels can be overestimated. In Eulerian models this problem can be solved by defining sublayers in the mixing-layer. For one-layer Lagrangian deposition models a correction factor is defined sometimes, representing the fraction of the emission that is directly deposited within the grid cell (Eliassen and Saltbones, 1983; Janssen and Asman, 1988). In some statistical LRT models immediate vertical mixing within the boundary layer is also assumed (Smith, 1981; Venkatram *et al*., 1982). Other authors use vertical distribution functions based on the K-diffusion theory (Bolin and Persson, 1975; Sheih, 1977; Fisher, 1978).

The problem of local dispersion is solved in this model by replacing $D_z(x) = 1/z_i$ in Eq. (3.9) by a Gaussian plume formulation, in which the vertical dispersion (for $z = 0$) is described as a function of source height, mixing height and a stability-dependent vertical dispersion length $\sigma_z(x)$ (the standard deviation from normal on the Gaussian distribution curve) [m]:

$$D_z(x) = \frac{2}{\sqrt{2\pi}\,\sigma_z}\left(\exp\left[\frac{-(2z_i-h)^2}{2\sigma_z^2}\right] + \exp\left[\frac{-(2z_i+h)^2}{2\sigma_z^2}\right] + \exp\left[\frac{-h^2}{2\sigma_z^2}\right]\right), \tag{3.15}$$

where h is the effective source height. Equation (3.15) was selected to describe local vertical diffusion, mainly to achieve some compatibility with the 'National Model' in the Netherlands (TNO, 1976). Equation (3.15) gives the same value as $1/z_i$ within 1.5% for the entire range of h within the mixing layer when $\sigma_z > 1.6\, z_i$, so a gradual change from limited vertical dispersion to full mixing at larger distances is automatically obtained.
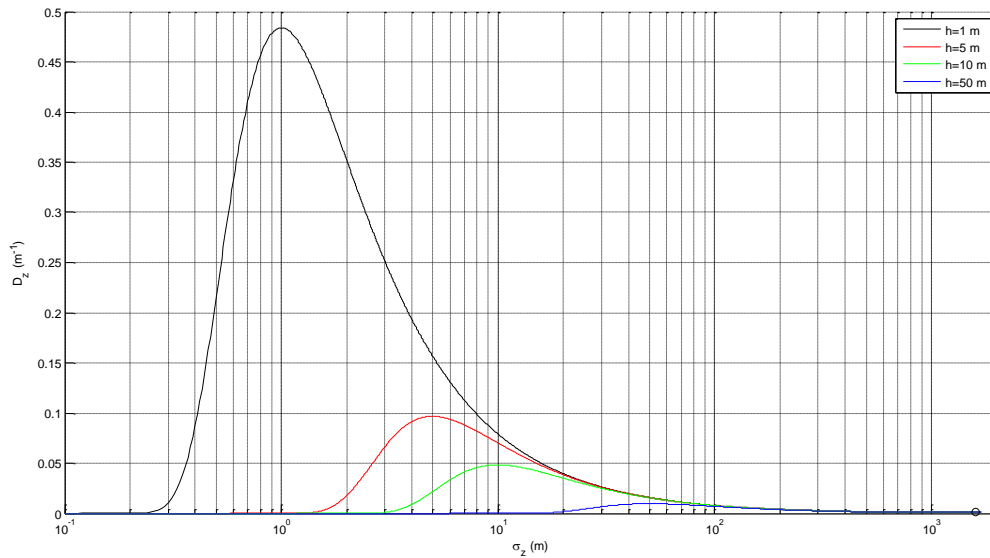
Figure 3.2   Vertical dispersion factor D_z as function of vertical dispersion length σ_z for different values of source height h and a mixing height $z_i = 1000$ m (Eq. 3.15). The circle at the far right denotes the value $D_z = 1/z_i$ (Eq. 3.9).

3.3.1 Dispersion of heavy plumes

Heavy plumes are defined as plumes consisting of large particles that do not follow all micro-scale atmospheric movements completely. This is the case if the size of the particles is so large that they settle downwards with a velocity that is significantly higher than the dry deposition caused by processes as inertial impaction or atmospheric diffusion. The mass weighted centre of such plumes will decrease with transport distance, resulting in an enhanced concentration at the surface compared to similar plumes with no 'falling' particles.

More important than the enhanced atmospheric concentration caused by descending plumes might be the effect on the dry deposition flux. This is due to the strongly non-linear relation between particle size and deposition velocity. A few percent heavy particles may cause a major contribution to the total dry deposition flux.

Large particles usually originate from windblown dust, open fires, incinerators with no filter equipment, sea-salt and so on. In the OPS model a single size-class for heavy plumes is used. This class is reserved for particles larger than 20 µm. For other size classes, the sedimentation effect is incorporated in the dry deposition velocity, but no effect on the plume height is assumed.

The cross-wind integrated concentration (g/m^2) in a heavy plume is described (Onderdelinden, 1985) by a direct source term and an indirect source, reflecting from the earth surface:

$$C(x,z) = \frac{Q}{\sqrt{2\pi}\,u\,\sigma_z} \left(\exp\left[\frac{-(z-h+\delta)^2}{2\sigma_z^2} \right] + \exp\left[\frac{-(z+h+\delta)^2}{2\sigma_z^2} + \frac{4h\delta}{2\sigma_z^2} \right] \right), \quad (3.16)$$

with Q the source strength, h the emission height, δ the plume descent (m):

$$\delta = v_s\,\frac{x}{u}, \tag{3.17}$$

where v_s: settling velocity of heavy particles (m/s), x: down-wind distance from source (m), u: wind speed (m/s).

3.3.2 Local vertical dispersion

For an appropriate determination of the vertical dispersion length, the turbulent state of the atmospheric boundary layer must be assessed. Most widely used is the approach of Pasquill (1961) and Gifford (1961). The Pasquill-Gifford scheme prescribes the quantitative relation between the stability of the atmosphere and insulation in combination with wind speed. The scheme has been deduced from experiments using sources near the ground. First versions of the present model (Van Jaarsveld, 1990) also used the Pasquill-Gifford scheme for dispersion and an empirical method for estimating stability similar to the Pasquill-Turner scheme (KNMI, 1972). Vertical dispersion was described there as

$$\sigma_z = c_{z0}\, a\, x^b, \tag{3.18}$$

with c_{z0} a correction factor for surface roughness and a and b stability-class-dependent dispersion coefficients taken from the Dutch National model (TNO, 1976).
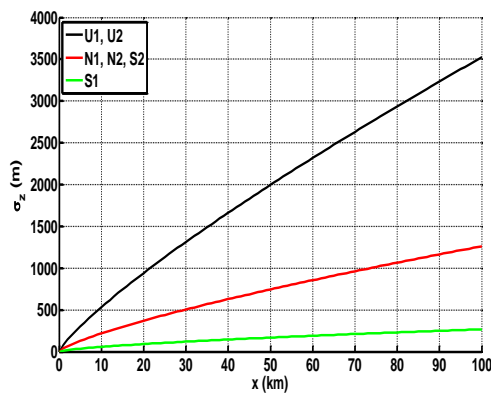

Table 3.1: initial settings of parameters a and b in Eq. 3.18. Note that coefficient a is recalculated based on more sophisticated parameterisations of σ_z.

stability class	a	b
U1, U2	0.2800	0.8200
N1, N2, S2	0.2000	0.7600
S1	0.1200	0.6700

Figure 3.3   Vertical dispersion length σ_z as described by Pasquill as function of x = distance from source, for stability classes {U1, U2}, {N1, N2, S2} and S1; c_{z0} = 1. Stability classes as defined in Table 1.1. Note that the present OPS-model uses more sophisticated parameterisations of σ_z.

Turbulence typing schemes, such as the Pasquill-Turner one, are biased toward neutral stability when convective situations actually exist (Weil and Brower, 1984).

Kretzschmar and Mertens (1984) reviewed the turbulence typing schemes and corresponding dispersion algorithms of a number of Gaussian short-range models. They found that the predicted maximum concentration and also the distance of this maximum concentration differed between the models by one order of magnitude. In the present version of the model, more recent concepts of the description of turbulence and dispersion in the boundary layer have been used. In such a concept the boundary layer is divided into a number of regimes, each characterised by distinct scaling parameters (Holtslag and Nieuwstadt, 1986; Gryning *et al*., 1987). The Holtslag and Nieuwstadt scheme is adopted here in a simplified form. The regimes distinguished are (see also Figure 3.4):

<u>a</u>. a surface layer with a height up to 0.1 z_i,
<u>b</u>. a convective mixing layer ($z_i/L < -10$ and $z/z_i > 0.1$)
<u>c</u>. a near neutral upper layer ($0 > z_i/L > -10$ and $z/z_i > 0.1$) and
<u>d</u>. a second near neutral layer above a stable surface layer ($0 < z_i/L$ and $z/z_i > 0.1$),

where L is the Monin-Obukhov length [m].
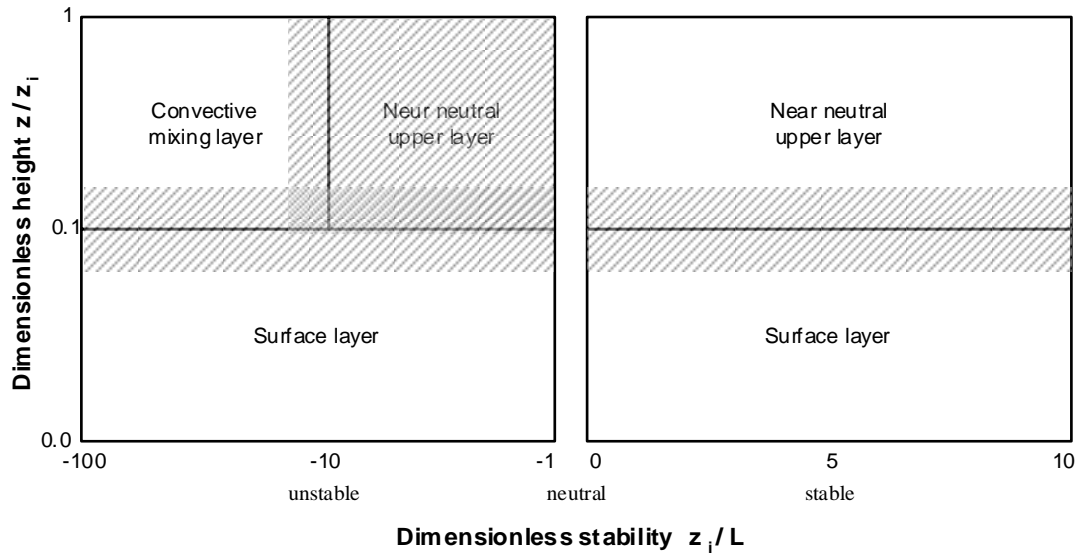
Figure 3.4   The scaling regions of the atmospheric boundary layer distinguished by the present model, and shown as function of the dimensionless height, z/z_i, and the stability parameter, z_i/L (L: Monin-Obukhov length). This scheme is a simplified form of the Holtslag and Nieuwstadt scheme (1986). In the shaded areas, OPS interpolates σ_z.

a. surface layer

The effect of stability on the structure in this layer can be described by the Monin-Obukhov similarity theory. Nieuwstadt and Van Ulden (1978) have shown that the vertical dispersion from a ground-level source in this layer can be adequately described by K-models. The K-model can be derived from the well-known diffusion equation, when horizontal diffusion is neglected:

$$u \frac{\partial C}{\partial t} = \frac{\partial}{\partial z} K_z(z) \frac{\partial C}{\partial z}. \tag{3.19}$$

OPS uses the following parameterisations for K_z:

$$K_z = \frac{\kappa u_* z}{\varphi_h(z/L)} \quad , \text{ for } L > 0 \text{ (Businger, 1973),} \tag{3.20}$$

$$K_z = \frac{\kappa u_* z}{\varphi_h(z/L)} \left(1 - \frac{z}{z_i}\right)^{1.5} \quad , \text{ for } L \leq 0 \text{ (Brost and Wyngaard, 1978),} \tag{3.21}$$

where $\varphi_h(z/L)$ is the non-dimensional temperature gradient:

$$\varphi_h(z/L) = 0.74 \ (1 - 9 \ z/L)^{-1/2} \text{ for } L \leq 0, \tag{3.22}$$
$$\varphi_h(z/L) = 0.74 + 4.7 \ z/L \qquad \text{for } L > 0. \tag{3.23}$$

Note that the von Kármán constant κ in Eq. (3.20) is specified by Businger as 0.35, while for the rest of this work, κ is taken 0.4.

Figure 3.5   Diffusion coefficient K_z (log scale) as function of z (z < 0.1z$_i$) for different meteo classes. Meteo classes and parameters for u*, L, z$_i$ from Table 2.5

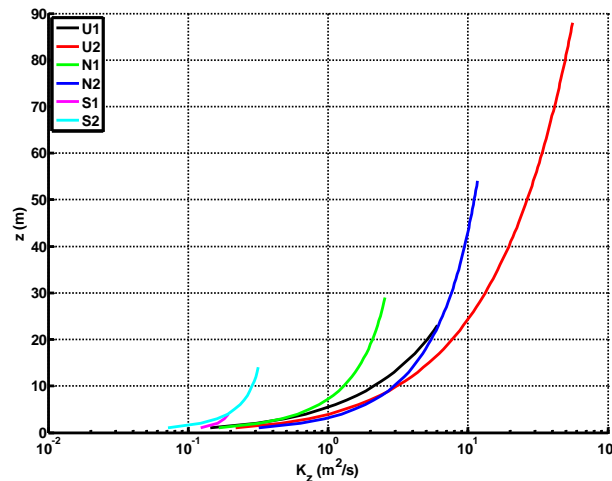The *K*-model is usually solved numerically; however, analytical solutions for surface-layer *K*-models have also been proposed (e.g. Van Ulden, 1978). Instead of using a separate model for the surface layer, *K*-theory in combination with the Gaussian dispersion formulation given in Eq. (3.15) has been applied. In fact, a Gaussian model is an analytical solution of the general diffusion equation for a continuous source in a situation with constant wind speed and diffusion, and where advection in the *x* direction is much more important than diffusion in this direction. Under these conditions σ_z can be related to the turbulent eddy diffusivity K_z (Pasquill, 1962):

$$\sigma_z^2 = 2K_z \, x \, / \, u \; . \tag{3.24}$$

This relation suggests that σ_z increases with distance proportional to $x^{1/2}$, while dispersion experiments show that this is only so for large σ_z. This discrepancy is mainly caused by not taking into account the vertical dimensions of the plume. The larger the plume grows, the more eddies have an effect on it. This is in fact what is suggested by the height dependence of K_z (Eq. 3.20). For (near) surface releases, *u* and K_z should be averaged over the plume height by integration, because the centre of mass may rise above the release height. In the present case, an iterative approach is followed, in which *u* and K_z are taken at a representative height equal to $0.67\sigma_z$ and where *u* is derived from the wind speed at 10 m using the logarithmic profile of Eq. 2.13. In this way, K_z becomes a function of *x*. The advantage of this approach is that effects of release height and z_0 can be explicitly taken into account, the latter through its effects on *u* and *L*. The error that is made by describing a non-Gaussian vertical distribution as Gaussian is not large.

The vertical diffusion from sources near the ground is tested using experimental data derived by Van Ulden (1978) from the 'Prairie Grass experiment' (Barad, 1958). Computed cross-wind integrated concentrations, at distances of 50, 200 and 800 m from the source, compare favourably with the observations as is shown in Figure 3.6. The comparison also indicates that the approach followed here has the same performance as the analytical scheme of Van Ulden (1978).
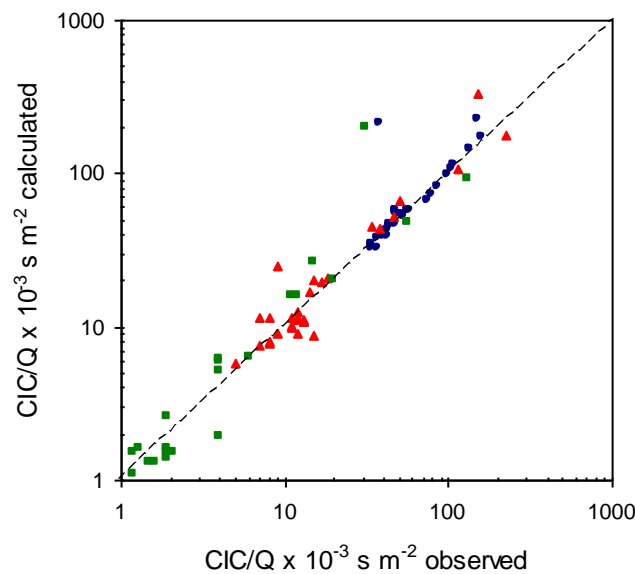
Figure 3.6   Comparison of calculated and measured cross-wind integrated concentration (CIC) divided by the source strength for three down-wind distances. Circles: 50 m. Squares: 200 m. Triangles: 800 m. The observational data, including u and L, are derived from the 'Prairie Grass' data by Van Ulden (1978).*

b. convective mixing layer

The dispersion process in the convective mixing layer is dominated by the asymmetric structure of turbulence (Gryning *et al.*, 1987). Downdraughts in this layer occupy a greater area than updraughts; therefore pollutants released from an elevated source have a higher probability of travelling downward than upward. A Gaussian dispersion approach is not suited for such cases. Several models have been proposed to describe the asymmetric behaviour e.g. the probability density function model (Misra, 1982; Venkatram, 1983; Weil and Brower, 1984) or the impingement model for buoyant sources (Venkatram, 1980). Several advanced short-term short-range models, however, still use Gaussian dispersion for the convective mixing layer. Therefore for the present long-term model, the Gaussian distribution was considered adequate.

Theoretical investigations by Deardorff (1972) and laboratory experiments by Willis and Deardorff (1974; 1978; 1981) indicate that turbulence and dispersion in a convective boundary layer are controlled by two important parameters: mixing-layer height z_i [m] and the convective velocity scale, w_* [m s^{-1}]:

$$w_* = (\frac{g}{T} \frac{H_0}{\rho_a \ c_p} z_i)^{1/3}, \tag{3.25}$$

with

ρ_a : air density [kg m^{-3}]
c_p : specific heat capacity [J kg^{-1} K^{-1}]/
g : acceleration of gravity [m s^{-2}]
T : absolute temperature [K]
H_0 : surface heat flux [W m^{-2}].

Another aspect demonstrated by these experiments and also by large eddy simulations (Wyngaard and Brost, 1984) is that turbulent fluxes can be opposed to local concentration gradients. This phenomenon puts the applicability of eddy diffusion as a basis for dispersion description in this layer on very tenuous ground (Weil, 1985).

Several authors have proposed dispersion parameterisations on the basis of convective velocity scaling. Reviews on this subject are given by Weil (1985) and Briggs (1985). The formulation of Weil and Brower (1984) for convective to neutral cases is taken as suggested by Briggs (1985), reading:

$$\sigma_z = z_i \; X \left[\; (\frac{\sigma_{wc}}{w_*})^2 + (\frac{\sigma_{wm}}{w_*})^2 \; \right]^{1/2}, \tag{3.26}$$

where $X = (x/u)w_*/z_i$, and σ_{wc} and σ_{wm} are the standard deviations of the vertical velocity component due to convective activity and wind shear (mechanical turbulence), respectively. For the convective limit, OPS uses $\sigma_{wc}/w_* = 0.56$ (Kaimal et $al.$, 1976) and the neutral limit, $\sigma_{wm} = 1.26 \; u_*$ (Panowski et $al.$, 1977). A similar formulation is used in the Danish OML model but with $\sigma_{wm} = 1.10 \; u_*$ (Berkowicz et $al.$, 1986).

$\underline{c}$. and $\underline{d}$. $upper$ $near$ $neutral$ $layers$

The characteristics of dispersion in the near neutral upper layer have not been thoroughly investigated. Turbulence in this region is rather homogenous, enabling the use of a Gaussian plume formulation. Following Venkatram (1984) and Gryning et $al.$ (1987) the estimate of the vertical spread is based on Taylor's theory, which relates σ_z to the standard deviations of the vertical wind fluctuations, σ_w. The relation can generally be written as

$$\sigma_z = \sigma_w t \, f_z (t / \tau_L), \tag{3.27}$$

where t is the travel time ($t = x/u$) and τ_L the Lagrangian time scale. A practical relation for f_z that matches the short and long time limits of statistical theory is:

$$f_z \; (t / \tau_L) = 1/(1 + \left(\frac{t}{2\tau_L} \right)^{1/2}). \tag{3.28}$$

Gryning et $al.$ (1987) suggest time scales τ_L of 300 s for $L < 0$ and 30 s for $L > 0$. In OPS, a linear function of (1/L) is used:

$$\tau_L = f_1 - f_2 \left(\frac{1}{L} \right), \text{ with } f_1 = 150 \text{ s}, f_2 = 2000 \text{ sm} \tag{3.29}$$

and cut-off values τ_L of 400 s for $L < 0$ and 10 s for $L > 0$.
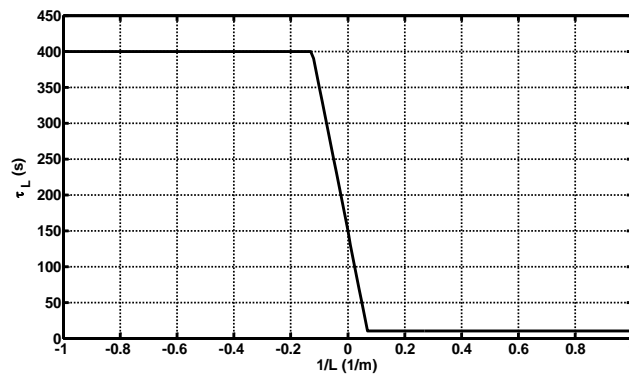

Figure 3.7: Lagrangian time scale τ_L as function of inverse Monin-Obhukov length.

Their adopted expressions for σ_w read:

$$(\sigma_w / u_*)^2 = 1.5 \, [\, z / (-\kappa \, L)]^{2/3} \exp \, (-2 z / z_i) + (1.7 - z / z_i) \qquad (\, L \leq 0 \,) \tag{3.30}$$

$$(\sigma_w / u_*)^2 = 1.7 (1 - z / z_i)^{3/2} \qquad\qquad (L \geq 0). \qquad (3.31)$$

The latter equation was proposed by Nieuwstadt (1984b) for horizontally homogeneous and stationary conditions. Vertical dispersion calculated for the near neutral upper layer matches those of the convective mixing layer at the boundary between the regions (at $z/L = -10$) rather closely.

Procedure in OPS

In OPS, σ_z for is calculated for the surface layer, convective mixing layer and near neutral upper layer, as a function of distance x, Monin-Obukhov length L, friction velocity $u*$ and mixing height z_i (according to 3.24, 3.26, 3.27). Depending on the values of dimensionless height z/z_i and dimensionless stability z_i/L, a specific value of σ_z is used; for regions $0.05 < z/z_i < 0.15$ and $-20 < z_i/L < 0$ an interpolation is used between the σ_z of the surface layer, convective mixing layer or near neutral upper layer.
Then the stability coefficient a in Eq. 3.18 is calculated from

$$a = \frac{\sigma_z}{x^b} , \qquad\qquad (3.32)$$

with values of coefficient b from Table 3.1. This approach makes it possible to use the expression $\sigma_z = a\, x^b$ in the rest of the OPS-model.

Comparison with observations

Computed cross-wind integrated concentrations have been compared with observations obtained in various field experiments with passive tracers. These observations, including the meteorological parameters z_i, u_* and L, have been compiled by Gryning *et al.* (1987). The stack heights in the different experiments were 2 m, 10 m and 115 m and the downwind distance range at which concentrations were measured was 0.2 - 6.1 km. Figure 3.8 shows the results, split into the different stability regimes.

In general, the agreement is satisfactory, especially for the convective mixing layer and the near neutral upper layer. Concentrations in the surface layer seem to be underestimated for the 115-m source (lower part of the scatter diagram) and overestimated for the 2-m source (upper part of the diagram). The latter overestimation is not seen in the comparison with the Prairie Grass data (Figure 3.6).
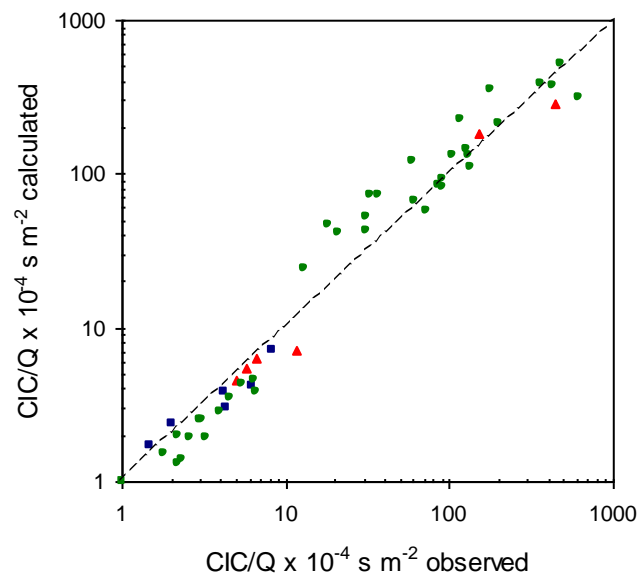
Figure 3.8   Comparison of calculated and measured cross-wind integrated concentration (CIC) divided by the source strength. Circles: surface layer stability regime. Squares: convective mixing layer regime. Triangles: near neutral upper layer regime. Observational data from various experiments, compiled by Gryning et al. (1987).

Initial vertical dispersion

An user provided initial vertical dispserion $\sigma_{z,ini}$ (in meters) is added to the computed vertical dispersion described above. This initial dispersion can be used to model turbulence close to the source, obstacles close to the source, or variations of source heights within an area source.

OPS has been calibrated to model concentrations that agree with the *Standaard Rekenmethode 2* (SRM-2; Wesseling and Van Velze, 2014) in proximity too roads. When modelling road traffic sources, an initial vertical dispersion can be calculated by the user with the calculations described by Wesseling et al. (2014; section "Initiële vertical verspreiding"). These calculations require information about the height of the road above the surface, the angles of the banks of the road, and the presence and height of wind screens. Next, the obtained initial spreads can be provided to the OPS model. If the *ROADS* option is used, OPS computes a new initial dispersion that accounts for the differences in transport modelling between SRM-2 and OPS, using the formula:

$$\sigma_{z,ini} = c_A + c_B \sigma_{z,ini,SRM2}$$

Coefficients c_A and c_B are given in Table 3.2 for different roughness length classes.

Table 3.2. Coefficients that are used to translate an initial dispersion from SRM2 to an initial dispersion in OPS.

Roughness length z_0 (in m)	c_A (in m)	c_B (in m/m)
$z_0 < 0.055$	1.05	1.53
$0.055 \leq z_0 < 0.17$	1.15	2.31
$0.17 \leq z_0 < 0.55$	1.33	2.25
$0.55 \leq z_0$	1.62	6.6

3.4 Area sources

The dispersion of material from a source is described in the preceding sections, for a source with no initial horizontal or vertical dimensions. In practice, however, it is seldom possible to treat all the sources in a certain area as point sources due to lack of detailed information. Also when the source is of the diffusive type, e.g. ammonia evaporating from a pasture, it is much more effective to treat the pasture as a single area source rather than splitting it up in numerous point sources.

When the heights of the different sources show an important variation, it is preferred to include this variation in the source description as an initial vertical dispersion (Martin, 1971). For modelling concentrations inside and outside an area source, expressions like Eq. (3.15) can be applied, but both the vertical and horizontal distribution terms $D_z(x)$ and $D_y(x)$ have to be modified to capture the special properties of the area source.

3.4.1 Horizontal dispersion for area sources

A point source will normally contribute to a receptor in only one wind sector, i, which is determined by:

$$i(\varphi) = \varphi \frac{m_s}{2\pi} + 1, \qquad (3.33)$$

where φ is the source - receptor direction specified in radians and m_s the number of wind-direction sectors which are applied in the model ($m_s = 12$). For area sources, however, contributions from more than one wind sector are possible. The horizontal dimension of an area source is introduced in the model by using the virtual point-source concept, where the virtual origin is put at a distance x_v upwind from the real position of the source (see Figure 3.9). This virtual distance depends on the number of wind-direction sectors:

$$x_v = \frac{m_s \, s_a}{2\pi} = \frac{m_s \, r_a}{\pi}, \qquad (3.34)$$

where s_a is the diameter of the source and r_a its radius. Replacing x by $(x + x_v)$ in Eq. (3.8) introduces the effect of the horizontal dimensions of the source into the description of the horizontal dispersion.
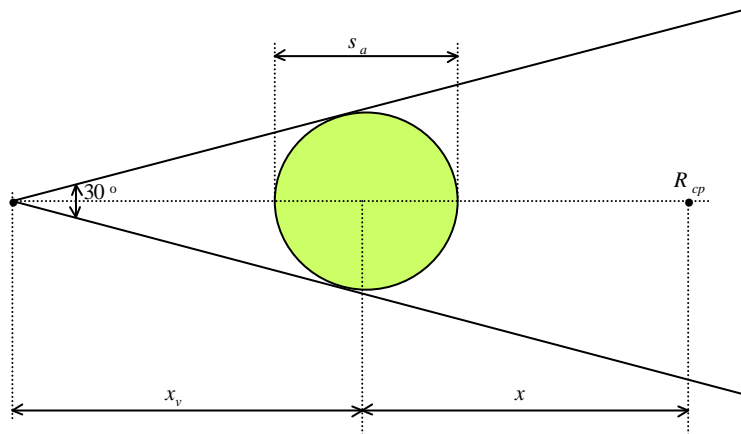

Figure 3.9   Area source represented by a virtual point source.

Another part of the problem is that an area source contributes more often to a given receptor point than a point source does. This is illustrated in Figure 3.10.

Figure 3.10   Wind directions for which an area source contributes to the concentration in a receptor point.

The wind direction angle, for which influence from the area source to concentrations in a receptor point R_{cp} can be expected, is indicated by φ. Since $\gamma = \dfrac{\pi}{2} - \tfrac{1}{2}\alpha = \left(\dfrac{1}{2} - \dfrac{1}{m_s} \right)\pi$, $\delta = \arctan(\dfrac{TR_{cp}}{ST}) =$

$\arctan(\dfrac{\sqrt{(x^2 - r_a^2)}}{r_a})$ and $\tfrac{1}{2}\varphi + \gamma + \delta = \pi$, it follows that

$$\varphi = 2\pi - 2\left(\arctan(\dfrac{\sqrt{(x^2 - r_a^2)}}{r_a}) + \left(\dfrac{1}{2} - \dfrac{1}{m_s} \right)\pi \right). \tag{3.35}$$

An equivalent formulation uses $\beta = \arcsin(\dfrac{ST}{SR_{cp}}) = \arcsin(\dfrac{r_a}{x})$ and $\tfrac{1}{2}\varphi + \gamma + \left(\dfrac{\pi}{2} - \beta \right) = \pi$:

$$\varphi = \dfrac{2\pi}{m_s} + 2\arcsin(\dfrac{r_a}{x}). \tag{3.36}$$

We consider n contributing wind sectors, with

$$n = \dfrac{\varphi}{\left(2\pi / m_s \right)} . \tag{3.37}$$

For very large distances ($x \to \infty$), n approaches 1, so an area source at that distance is seen as a point source. Another extreme case is when the receptor point is at the edge of the area source ($x = r_a$); the number of sectors then becomes: $n = 1 + m_s/2$, which means that using a classification in 12 sectors, the contributions of 7 wind-direction sectors have to be accumulated in determining an average concentration. Equation (3.37) is applied for x down to r_a, where the contribution of the 7 sectors is weighed according to the distance to the central sector (sector upwind from the direction centre of the area source to the receptor). The maximum of seven contributing sectors is also applied for receptors within the area source.

3.4.2 Vertical dispersion for area sources

The virtual point source concept, as used for the description of horizontal dispersion from sources with non-zero horizontal dimensions, is in principle also suitable for the description of vertical dispersion if plumes have initial vertical dimensions. The corresponding virtual distance would then of course differ from x_v given in Eq. (3.34). The vertical plume dimension of a source with non-zero horizontal dimensions cannot be described by the virtual point source concept because $D_z(x)$ is a non-linear function of x. In the following, an effective vertical dispersion parameter is derived which is used in the equation for $D_z(x)$. If one considers an area source as a source representing an infinite number of point sources, then the effective vertical distribution term at a distance x down-wind from the centre of the area source can be written as (see Figure 3.11):

$$D_z(x)_{eff} = \frac{1}{r_2 - r_1} \int_{r_1}^{r_2} D_z(r)\,dr \qquad (r_1 \geq 0), \tag{3.38}$$

where $D_z(r)$ is the vertical distribution term for a point source at distance r down-wind as given by Eq. (3.15). r_1 is taken as zero when $r < \frac{1}{2}\,s_a$.
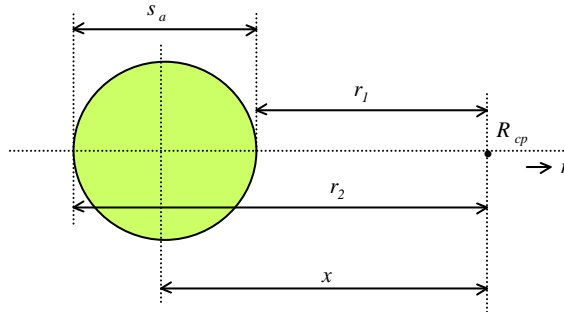

Figure 3.11   Schematic representation of an area source.

Under the condition that reflection against the top of the mixing layer is of minor importance ($\sigma_z(r) << z_i$) and the source height is low ($h << \sigma_z(r)$), then the above expression can be written as:

$$D_z(x)_{eff} = \frac{1}{r_2 - r_1} \int_{r_1}^{r_2} \frac{2}{\sqrt{2\pi}}\,\frac{1}{\sigma_z(r)}\,dr \qquad (r_1 \geq 0). \tag{3.39}$$

In order to introduce an initial vertical distribution and also to express the vertical distribution in a more convenient parameter, the following form is chosen:

$$\frac{1}{\sigma_z(x)_{eff}} = \frac{1}{r_2 - r_1} \int_{r_1}^{r_2} \frac{1}{\sigma_z(r) + \sigma_{zi}}\,dr \qquad (r_1 \geq 0) \tag{3.40}$$

where the initial vertical dispersion length σ_{zi} represents the distribution of source heights within the area source. Setting a vertical dispersion length $\sigma_z(r)$ of the form ar^b, it is not possible to obtain a simple solution to the integral in Eq. (3.40) for all possible values of b. For $b = 1$, however, we can solve the integral:

$$\sigma_z(x)_{eff} = (ar_2 - ar_1)\left[\ \ln\left(\frac{\sigma_{zi} + ar_2}{\sigma_{zi} + ar_1}\right)\right]^{-1}. \tag{3.41}$$

The following expression has been chosen as a practical approximation for a general $\sigma_{z,eff}$:

$$\sigma_z(x)_{eff} = \left(\sigma_z(r_2) - \sigma_z(r_1)\right)\left[\ln\left(\frac{\sigma_{zi} + \sigma_z(r_2)}{\sigma_{zi} + \sigma_z(r_1)}\right)\right]^{-1}.$$

(3.42)

Equation (3.42) is applied inside and outside the area source with a lower limit equal to s_a for r_2 and a lower limit equal to $h/8$ or 0.1 m for σ_{zi}. The resulting $\sigma_{z,eff}$ is used in conjunction with (3.15). When $\sigma_{z,eff}$ is compared with σ_z for a single point source as a function of down-wind distance, then it appears that $\sigma_{z,eff}$ is small and rather constant within the area source, rapidly increasing outside the area source and approaching σ_z at a large distance.

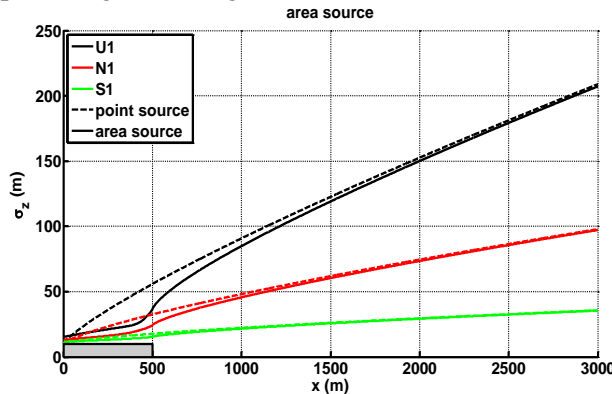*Figure 3.12* $\sigma_{z,eff}$ *as function of down-wind distance x (m) for three meteo classes (Unstable, Neutral, Stable). The dashed lines show σ_z for a point source, the closed lines show $\sigma_{z,eff}$ for an area source. Half the area source is shown as a grey box (500 m radius, height of the box = initial dispersion length $\sigma_{zi} = 10$ m).*

3.5   References

Barad M.L., editor (1958) Project Prairie Grass, a field program in diffusion.Volume 1, Geophysics Research Paper no. 59. Geophysics Research Directorate, Air Force Cambridge Research Center, Cambridge MA, USA.

Berkowicz R., Olesen H.R. and Torp U. (1986) The Danish Gaussian Air Pollution Model (OML): description, test and sensitivity analysis in view of regulatory applications. In: De Wispelaere C., Schiermeier F.A. and Gillani N.V., editors. Air pollution modeling and its application V. Plenum Press, New York. p. 453-482.

Bolin B., Aspling G. and Persson, C. (1974) Residence time of atmospheric pollutants as dependent on source characteristics, atmospheric diffusion processes and sink mechanisms. Tellus 26, 185-195.

Briggs G.A. (1985) Analytical parameterisations of diffusion: The convective boundary layer. J. Climate Appl. Meteorol. 24, 1167-1186.

Brost, R. A., J. C. Wyngaard, 1978: A Model Study of the Stably Stratified Planetary Boundary Layer. *J. Atmos. Sci.*, **35**, 1427–1440. doi: http://dx.doi.org/10.1175/1520-0469(1978)035<1427:AMSOTS>2.0.CO;2

Businger J.A. (1973) Turbulent transfer in the atmospheric surface layer. In: Haugen D.A., editor. Workshop on Micrometeorology. AMS, Boston MA. p. 67-100.

Eliassen A. and Saltbones J. (1983) Modelling of long-range transport of sulphur over Europe: a two-year run and some model experiments. Atmospheric Environment 17, 1457-1473.

Fisher B.E.A. (1978) The calculation of long term sulphur deposition in Europe. Atmospheric Environment 12, 489-501.

Gifford F.A. (1961) Use of meteorological observations for estimating atmospheric dispersion. Nuclear Safety 2, 47-51.

Gryning S.E., Holtslag A.A.M., Irwin J.S. and Sivertsen B. (1987) Applied dispersion modelling based on meteorological scaling parameters. Atmospheric Environment 22, 79-89.

Holtslag A.A.M. and Nieuwstadt F.T.M. (1986) Scaling the atmospheric boundary layer. Boundary-Layer Meteorol. 36, 201-209.

Janssen A.J. and Asman W.A.H. (1988) Effective removal parameters in long-range air pollution transport models. Atmospheric Environment 22, 359-367.

Kaimal J.C., Wyngaard J.C., Haugen D.A., Cote O.R., Izumi Y., Caughey S.J. and Readings C.J. (1976) Turbulence structure in the convective boundary layer. J. Atmos. Sci. 33, 2152-2169.

KNMI (1972) Klimatologische gegevens van Nederlandse stations. Frekwentietabellen van de stabiliteit van de atmosfeer. Royal Netherlands Meteorological Institute, De Bilt, the Netherlands.

Kretzschmar J.G. and Mertens I. (1984) Influence of the turbulence typing scheme upon cumulative frequency distributions of the calculated relative concentrations for different averaging times. Atmospheric Environment 18, 2377-2393.

Martin D.O. (1971) An urban diffusion model for estimating long term average values of air quality. J. Air Pollut. Control Assoc. 21, 16-19.

Misra P.K. (1982) Dispersion of non-buoyant particles inside a convective boundary layer. Atmospheric Environment 16, 239-243.

Nieuwstadt F.T.M. (1984b) The turbulent structure of the stable nocturnal boundary layer. J. Atmos. Sci. 41, 2202-2216.

Nieuwstadt F.T.M. and Ulden A.P. van (1978) A numerical study on the vertical dispersion of passive contaminants from a continuous source in the atmospheric surface layer. Atmospheric Environment 12, 2119-2124.

Onderdelinden (1985): Source depletion model, personal communication in OPS archive.

Panowski H.A. Tennekes H., Lenschow D.H. and Wyngaard J.C. (1977) The characteristics of turbulence velocity components in the surface layer under convective conditions. Boundary-Layer Meteorol. 11, 355-361.

Pasquill F. (1961) The estimation of the dispersion of windborn material. Meteorol. Mag. 90, 33-49.

Pasquill F. (1962) Atmospheric Diffusion. Van Nostrand, New York. p. 77.

Sheih C.M. (1977) Application of a statistical trajectory model to the simulation of sulfur pollution over northeastern United States. Atmospheric Environment 11, 173-178.

Smith F.B. (1981) The significance of wet and dry synoptic regions on long-range transport of pollution and its deposition. Atmospheric Environment 15, 863-873.

TNO (1976) Modellen voor de berekening van de verspreiding van luchtverontreiniging inclusief aanbevelingen voor de waarden van parameters in het lange-termijnmodel. Staatsuitgeverij, The Hague, the Netherlands.

Van Jaarsveld J.A. (1990) An operational atmospheric transport model for priority substances; specification and instructions for use. RIVM, Bilthoven, the Netherlands. Report no. 222501002.

Venkatram A. (1980) Dispersion from an elevated source in a convective boundary layer. Atmospheric Environment 14, 1-10.

Venkatram A. (1983) On dispersion in the convective boundary layer. Atmospheric Environment 17, 529-533.

Venkatram A. (1984) The uncertainty in estimating dispersion in the convective boundary layer. Atmospheric Environment 18, 307-310.

Venkatram A., Ley B.E. and Wong S.Y. (1982) A statistical model to estimate long-term concentrations of pollutants associated with long-range transport. Atmospheric Environment 16, 249-257.

Weil J.C. (1985) Updating applied diffusion models. J. Climate Appl. Meteorol. 24, 1111-1130.

Weil J.C. and Brower R.P (1984) An updated Gaussian plume model for tall stacks. J. Air Pollut. Control Assoc. 34, 818-827.

Wesseling J., and K. van Velze (2014) Technische beschrijving van standaardrekenmethode 2 (SRM-2) voor luchtkwaliteitsberekeningen. RIVM Briefrapport 2014-0109.

Willis G.E. and Deardorff J.W. (1974) A laboratory model of the unstable planetary boundary layer. J. Atmos. Sci. 31, 1297-1307.

Willis G.E. and Deardorff J.W. (1978) A laboratory study of dispersion from an elevated source within a modelled convective planetary boundary layer. Atmospheric Environment 12, 1305-1311.

Willis G.E. and Deardorff J.W. (1981) A laboratory study of dispersion from a source in the middle of the convective mixed layer. Atmospheric Environment 15, 109-117.

Wyngaard J.C. and Brost R.A. (1984) Top-down and bottom-up diffusion of a scalar in the convective boundary layer. J. Atmos. Sci. 41, 102-112.

4. Emission and emission processes

Important for the dispersion of pollutants are the meteorological conditions at the moment substances are released into the atmosphere. Systematic differences can be found for meteorological conditions, the most important being seasonal variations and diurnal cycles. Variations in emissions such as those related to diurnal cycles in traffic density may be taken into account by introducing typical daily variations. In such cases, despite still using yearly mean emission data, the model relates typical daily cycles in wind speed, temperature, radiation, etc. with the user-specified daily cycle in emissions. Although less specific than relating emission to meteorological conditions directly, this approach is believed to describe an important part of the effects.

In some cases, emission rates depend on the meteorological conditions themselves, e.g. emissions due to evaporation of liquids. In such a case, a correlation is likely to exist between emission rates and deposition rates (Van Jaarsveld *et al.*, 2000). This type of interaction is not addressed by means of a generic approach in the OPS model. Only in the specific case of the NH_3 evaporation from field-applied manure and animal housing systems is this process covered (see sections 4.3 and 4.3.7).

The source area for this model has been set at a circle with a radius of 1000 km, with the Netherlands as the centre. The contribution of sources in this area to concentration and deposition in the Netherlands may be calculated for countries individually. The contribution of sources outside this area, but within Europe, can be estimated, but with less accuracy. The calculation of country-specific contributions from this area is probably not meaningful.

4.1 Emissions: behaviour in time

Daily emission variations – generic approach
The time-dependent emission behaviour can only be specified as a daily variation. A number of pre-defined daily variations have been included in the model, where the options are:

0	continuous in time
1	according to the (average) industrial activity over a working day
2	according to the (average) heating activity for space heating (in e.g. houses, buildings); includes a seasonal correction in OPS (see below)
3	according to the (average) traffic intensity
31	according to the (average) traffic intensity of light duty vehicles
32	according to the (average) traffic intensity of heavy duty vehicles
33	according to the (average) traffic intensity of (public transport) buses
4	special value for evaporation emissions of NH_3 and NO_x from animal housings
5	special value for evaporation emissions of NH_3 and NO_x from application of manure and fertiliser
7	according to the (average) heating activity (in e.g. greenhouses). This is the same distribution over the year as option 2, but without the seasonal correction in OPS.

Apart from these pre-defined diurnal variations, the user can define up to 999 own variations, coded -1 to -999.

The daily variation is given in 2-hourly blocks and is specified in the local time zone at the source location; it uses the longitude which has been specified in the preprocessor METPRO. No distinction has been made between winter and summer time.

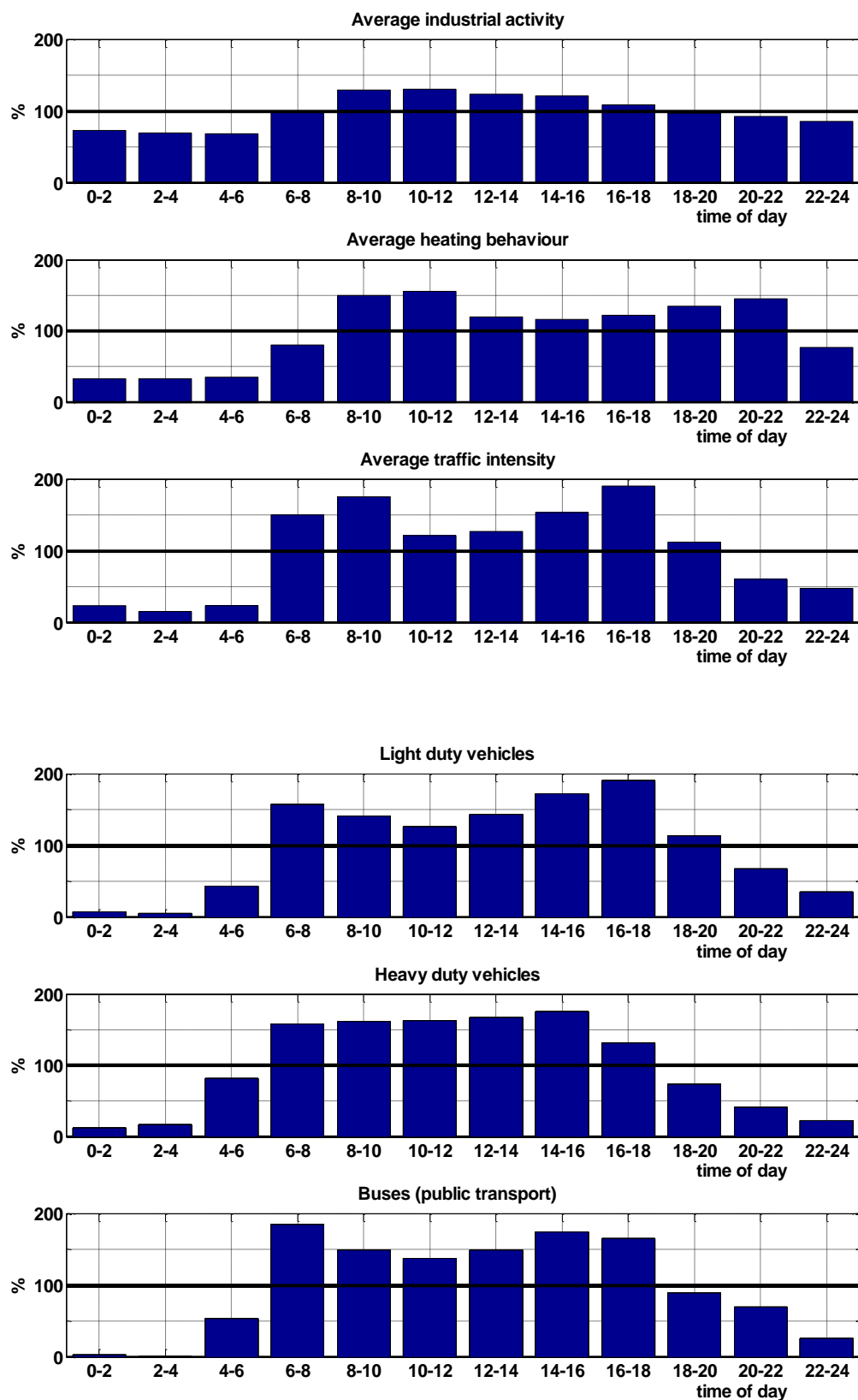Figure 4.1 shows the pre-defined daily emission variations used by the model.

Figure 4.1   Relative emission strength (%) for different source types in the course of the day.

Daily emission variations – specific approach for agricultural ammonia
In case of ammonia emission from animal housings or manure application, the model itself calculates the daily variation of the ammonia emission. To distinguish between emissions from animal housings and manure application, daily variations codes 4 and 5 are used (see sections 4.3 and 4.3.7).

Seasonal emission variations
The OPS model supports only one type of seasonal emission variation, the variation of emission due to space heating in houses and buildings. This seasonal variation is automatically switched on if the daily variation for space heating is selected for an emission source. The seasonal effect on space heating emissions is modelled on the basis of so called degree-day values in combination with a wind speed correction:

$$stc = (19^{\circ} - T_{24})\, (u_{10}/3.2)^{0.5} \qquad\qquad \text{if } T_{24} < 12\ ^{\circ}\text{C} \qquad\qquad (4.1)$$

in which T_{24} is the daily average outdoor temperature in $^{\circ}$C and u_{10} the wind speed at a height of 10 m in m/s (here we use a lower bound of 1 m/s); stc is taken to be zero if $T_{24} \geq 12\ ^{\circ}$C.
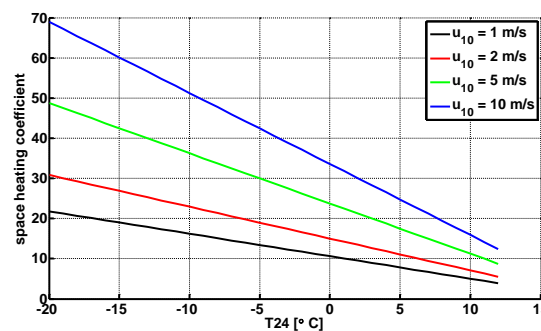

Figure 4.2 Space heating coefficient as function of daily average outdoor temperature for different values of wind speed u_{10}.

Average stc values are calculated with the meteorological pre-processor for each meteorological class and included in the meteorological data set. The correction of the space heating emission is carried out in OPS by first normalising stc with a long-term average value of stc.
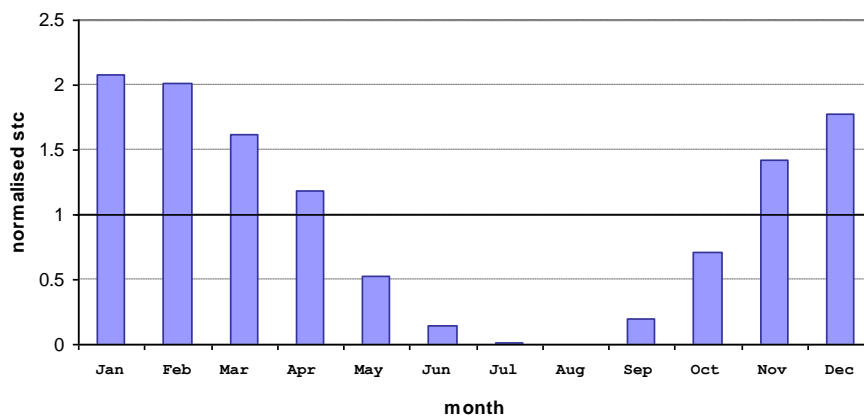

Figure 4.3 Monthly variation in space heating emission relative to long-term average emission.

Figure 4.3 gives the monthly variation in the normalised stc. These results are averages for the 1978-1991 period. Specific yearly mean values of the normalised stc may differ from 1, indicating warmer or colder winter seasons. The effect of seasonal variation may be illustrated in the NO_x emission due to space heating, which is in the order of 5% of the total emissions on a yearly basis. In a specific (cold) winter month an emission of this kind may amount up to 25% of the total emission. If this is combined with the daily emission variation and the phenomenon that dispersion is low when these emissions are high (early morning and evening), the influence of variations in space heating emissions

on atmospheric concentrations are clearly very significant. In order to take advantage of the different time-related variations, it is important to specify space heating and traffic-related emissions as separate source categories in the emission data file.

4.2   Emission speciation

The model distinguishes two types of emissions: gaseous and particulate. In the case of gaseous emissions, the rise of hot plumes is accounted for but the effect of cold and/or dense plumes (e.g. spills of liquefied gases) is not taken into account.

For particulate emissions, the emission is considered to be distributed over six particle-size classes, namely:

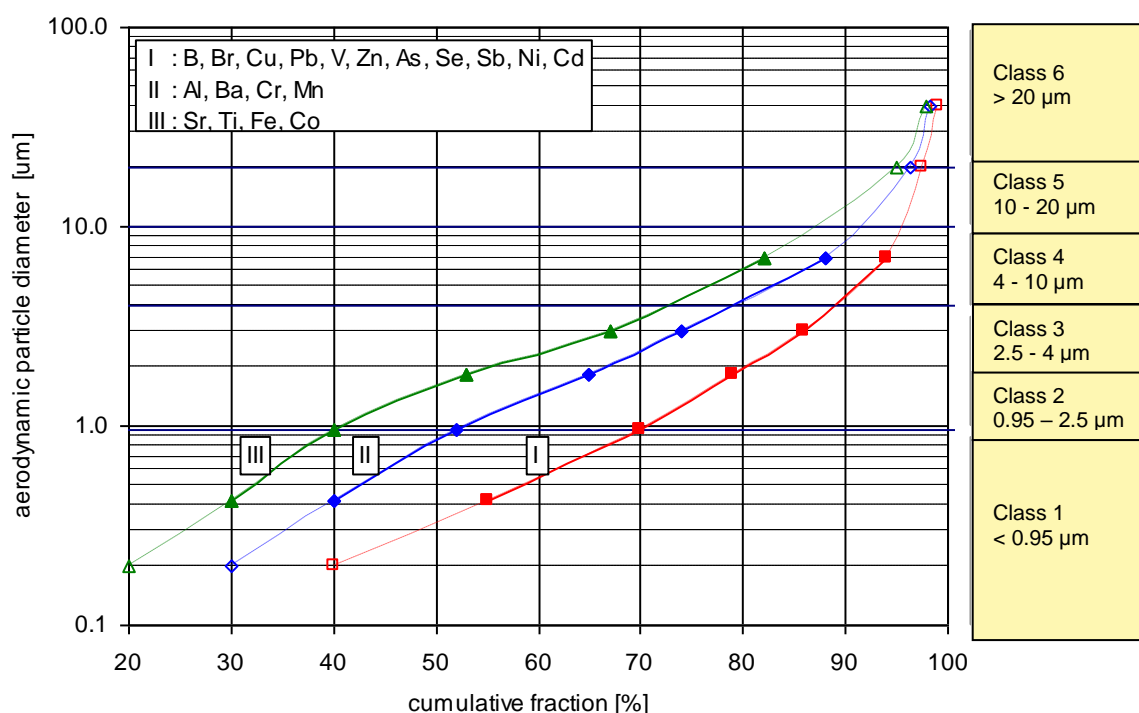| 1	2	3	4	5	6
< 0.95 μm	0.95 – 2.5 μm	2.5 – 4 μm	4 - 10 μm	10 - 20 μm	>20 μm

Figure 4.4. Particle-size distributions for a number of elements measured in background concentrations, and classified into three groups (Potma et al., 1986). After log-normal extrapolation these distributions are also taken to be representative of source emissions. The particle-size classification used in the OPS model is given at the right-hand side.

The model calculates concentration and deposition for these classes separately, with size specific properties for each class. The model is delivered with standard distributions. The distributions fine, medium and coarse (Table 4.1) are intended for modelling the dispersion and deposition of particle bound substances, like heavy metals. In addition to these general distributions, sector-specific distributions are available for PM_{10}. Because the sector-specific distributions might change from year to year - due to changing contributions of the underlying activities to the emission of a sector - they are not published here, but are available from the OPS website. In addition to choosing one of these model-included distributions, the user can specify up to 999 user-defined particle distributions.

In calculating the concentrations and depositions for the heaviest particles (> 20 μm), allowance is made for the fact that the sedimentation velocity of these particles is not insignificant, so that plume descent occurs with distance. This plume descent is not influenced by the stratification of the lower boundary layer. The sedimentation velocity v_s (m/s) is computed according to Stokes law:

$$v_s = \frac{\left(\rho_{particle} - \rho_{air}\right)\left(D_{particle}\right)^2 g}{18\mu_{air}},$$ (4.2)

with

$\rho_{particle}$ density of particle (kg/m^3)
ρ_{air} density of air (kg/m^3)
$D_{particle}$ diameter of particle (m)
g acceleration of gravity (m/s^2)
μ_{air} dynamic viscosity of air (kg /(s m)).

It is important to note that the particle size distribution must be specified for the moment that particles become airborne. Distributions measured in ambient air usually do not show the heavier particles because their atmospheric lifetime is shorter than smaller particles.

Table 4.1 Sedimentation velocity and standard particle-size distributions, for standard particle classes as used in OPS. Sedimentation velocity according to Stokes law for $\rho_{particle}$ = 1000 kg/m^3, ρ_{air} = 1.205 kg/m^3 (T = 20 C), μ_{air} = 1.81 10^{-5} kg /(s m).

particle size class		1	2	3	4	5	6
size range	μm	<0.95	0.95-2.5	2.5-4	4-10	10-20	>20
mass median diameter	μm	0.2	1.6	3	6	14	40
sedimentation velocity Stokes law	cm/s	0.00	0.01	0.03	0.11	0.59	4.81
standard distribution fine	%	70	12	8	5.5	2.5	2
standard distribution medium	%	53	16	12	11.5	4.2	3.3
standard distribution coarse	%	42	19	14	14.5	5.9	4.6

4.3 Emission processes

Emission processes described here are:
- plume rise due to momentum
- plume rise of hot effluent
- final plume rise
- inversion penetration of plumes
- NH$_3$ from land spreading
- NH$_3$ emissions from animal housing systems.

4.3.1 Plume rise due to momentum

Momentum plume rise is determined according to Briggs (1969), Turner et al. (1986). Note that it is only computed for vertical outflow, not for horizontal outflow.
For **unstable** and **neutral** weather conditions the plume rise Δh (m) is

$$\Delta h_{non\,stable} = \frac{3D v_s}{u_s},$$

with u_s the wind speed (m/s) at stack height (with a minimum of 10 m), D the inner diameter of the stack (m) and v_s the exit velocity of the effluent (m/s).

Momentum plume rise for **stable** conditions is then calculated with:

$$\Delta h_{stable} = 0.646 \left(\frac{v_s^2 D^2}{T_s u_s}\right)^{\frac{1}{3}} (T_a)^{\frac{1}{2}} \left(\frac{d\theta}{dz}\right)^{-\frac{1}{6}}.$$

Here, T_s is the temperature of the gas being emitted (K), T_a is the ambient temperature at stack height (K) and $d\theta/dz$ is the potential temperature gradient (K/m). OPS uses 0.006 K/m for this as a typical value for stable conditions. In stable conditions, the minimum value of Δh_{stable} and $\Delta h_{non\ stable}$ is used as the final momentum plume rise.
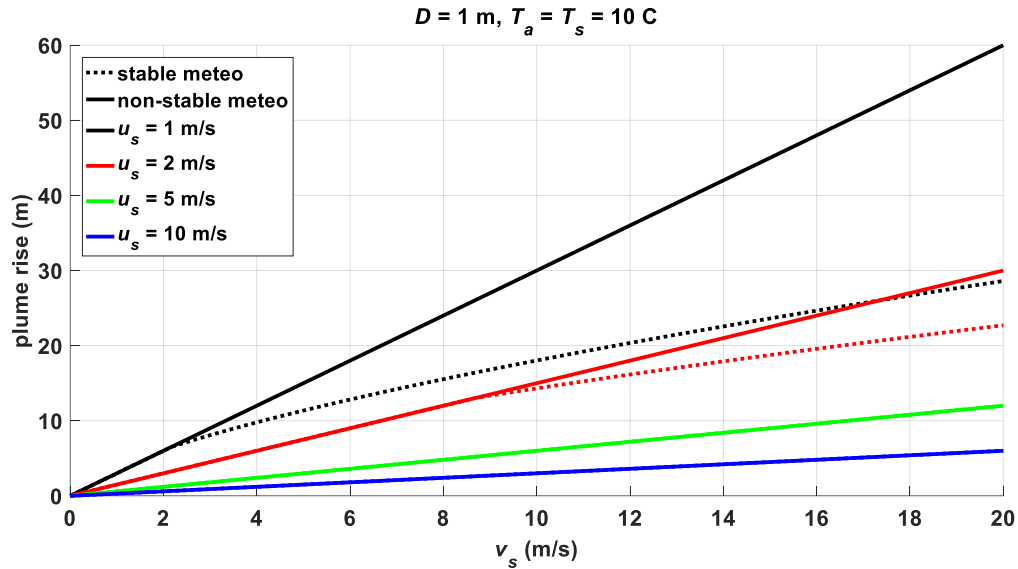

Figure 4.5   Momentum plume rise as function of exit velocity v_s for different values of wind speed u_s for convective/neutral conditions (solid lines) or stable conditions (dotted lines). Stack diameter = 1 m, ambient temperature = effluent gas temperature = 10 C.

4.3.2   Plume rise due to heat

Many models are available for the calculation of the rise of hot effluent from stacks, e.g. final rise models as proposed by Briggs (1971, 1975) or Weil (1985). These models incorporate some of the complex physics of the convective boundary layer. In the past, two approaches have been applied in the OPS model, one based on Briggs (1971) and one based on Briggs (1975). The Briggs (1975) approach is described in Van Jaarsveld (1995). In general terms, the Briggs (1971) approach is not only simpler but proved to provide better results after comparing model results with results of dispersion experiments. For this reason it is selected again for the present model. Note that plume rise due to heat may be present for both vertical and horizontal outflow.

The plume rise Δh for **convective** and **neutral** conditions ($L < 0$ or $|L| > 50$ m) is calculated as Briggs (1971):

$$\Delta h = 38.8 \, \frac{F_b^{3/5}}{u} \qquad for \ F_b \geq 55, \tag{4.3}$$

$$\Delta h = 21.3 \, \frac{F_b^{3/4}}{u} \qquad for \ F_b < 55, \tag{4.4}$$

where u is the ambient wind speed and F_b the stack buoyancy flux [m^4 s^{-3}], which is given by:

$$F_b = \frac{g}{\pi} V_s \left(1 - \frac{T}{T_s}\right) = \frac{g}{\pi} \frac{V_s}{T_s}(T_s - T) = \frac{g}{\pi} \frac{V_0}{T_0}(T_s - T) =$$

$$= \frac{g}{\rho_0 C_{p,0} \pi T_0 10^{-6}} \rho_0 C_{p,0} V_0 (T_s - T) 10^{-6} = c_0 Q_h . \qquad (4.5),$$

with

V_s :   volumetric flow rate of the stack gas [m^3 s^{-1}]
V_0 :   normalised (at T_0) volumetric flow rate of the stack gas [m$_0^3$ s^{-1}]
T :   ambient temperature at stack height [K]
T_s :   temperature of the stack gas [K]
T_0 :   temperature for which the flow rate is normalised (= 273 K)
ρ_0 :   reference density of air (= 1.293 kg/m^3)
$C_{p,0}$:   reference specific heat of air (= 1005 J/(kg K))
Q_h: (normalised) heat output of the stack [MW] = $\rho_0 C_{p,0} V_0 (T_s - T) 10^{-6}$
c_0 :   constant $= \frac{g}{\rho_0 C_{p,0} \pi T_0 10^{-6}} = 8.8$.

Note that the wind speed u, is evaluated at the stack top $h_s + \frac{1}{2} \Delta h$; this means that an iteration is used in order to resolve the interdependency between plume rise and wind speed.

For **stable** conditions ($0 \leq L \leq 50$), the plume rise is given by (Briggs 1975, 1982):

$$\Delta h = 2.6 \left(\frac{F_b}{s\, u}\right)^{\frac{1}{3}} , \text{ with stability parameter } s = \frac{g}{T} \frac{\partial \theta}{\partial z}, \qquad (4.6)$$

where $\partial\theta/\partial z$ is the potential temperature gradient at stack level. $\partial\theta/\partial z$ at stack height may vary, dependent on the stability in the surface layer. For lack of actual observations, an average value of 0.006 K m^{-1} is taken as representative for stable situations (TNO, 1976). Near the source, the plume may not have reached its final plume rise. The initial plume rise is usually evaluated using an $x^{2/3}$ dependence. (e.g. Berkowicz et al., 1986). Under the assumption that, on average, the vertical rise goes faster than the (downward) vertical plume growth, the final plume rise is considered to be instantaneously reached.
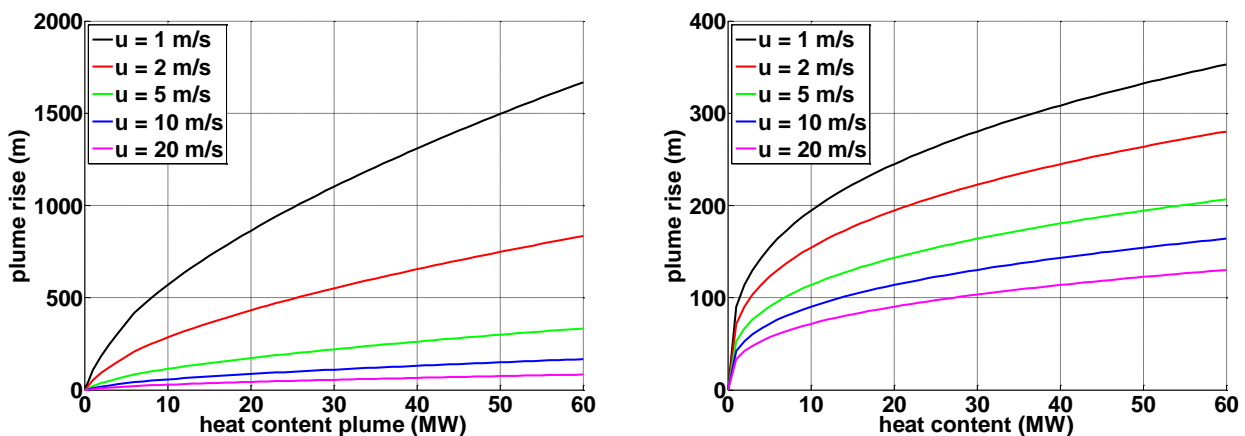
Figure 4.6   Plume rise as function of heat content of the plume for different values of wind speed u. Convective/neutral conditions (left panel) or stable conditions (right panel). Note the different scales for the y-axis for the two panels.

Note that the plume rise described above is for high stacks. For sources emitting at lower elevation, the value of $\partial\theta/\partial z$ can be much larger, especially in stable conditions.

4.3.3   Final plume rise

The final plume rise is the maximum of the plume rise due to heat (buoyancy) and due to momentum. It should be noted that the plume rise formulas for heat are fitted to practical situations with hot effluent. For these kind of sources, these formulas also cover plume rise due to momentum and a separate term for momentum plume rise is therefore not added.

4.3.4   Inversion penetration

The interaction of buoyant plumes with the top of the mixing layer can be described by models such as given by Manins (1979) or Briggs (1985). Both these relations assume a (thin) temperature inversion at mixing height z_i which can only be passed if the dissipation rate of the plume is still high enough after rising from h_s to z_i, but they differ strongly on the degree of penetration. Situations with strong (subsident) temperature inversions at low altitudes sometimes occur, leading to trapping of pollutants emitted by high stacks (Moore, 1987). Temperature jumps at z_i are, however, rather small in most situations, especially under neutral conditions.

In OPS, a classification into stability and mixing-height classes has been chosen (see Table 1.1), mainly to include effects of vertical stratification on a local scale, where each meteo class has a representative ensemble mixing height $z_i(x)$, which is the maximal mixing height that occurred during transport from the source to a receptor at distance x. The following simple distribution scheme has been chosen to model the process of plume penetration and entrainment at the top of the mixing layer:

$$f_m(x) = \frac{z_i(x)-h_1}{\Delta h} + c_i, \text{ if } h_s \leq z_i(x) \text{ and } \Delta h \neq 0 \tag{4.7a}$$

$$f_m(x) = \frac{z_i(x)-h_1}{z_i(x)} + c_i, \text{ if } h_s > z_i(x) \text{ or } \Delta h = 0 \tag{4.7b}$$

$$f_m(x) = \min(\max(f_m(x), 0, 1)), \tag{4.7b}$$

where f_m is the fraction of the plume in the mixing layer ($0 \leq f_m \leq 1$), h_s the stack height [m], Δh the plume rise [m], h_1 the effective emission height $= h_s + \Delta h$ [m]. c_i is an empirical constant representing the trapping effect. For neutral situations c_i is 0.5, indicating no trapping at all. In stable and unstable cases c_i is taken as 0.85.
Formula (4.7a) is derived from a 'top-hat' approximation of the plume distribution and is based on local observations of plumes (Briggs, 1975, 1982, Turner et al., 1986), while the other formulation (4.7b) focuses on the point where half of the mass (or better $c_i \cdot$ mass) is captured by the rising mixing layer height. This is the point where emission height is equal to mixing height.

OPS uses the parameter f_m to incorporate the process of entrainment at the top of the mixing layer into the model; this process mixes mass emitted above the mixing layer into the mixing layer, gradually with increasing distance. The entrainment process starts, according to formula (4.7b), when $f_m = 0$, which is equivalent to $h_1 = (1+c_i) z_i(x)$ and is complete if $f_m = 1$ equivalent to $h_1 = c_i z_i(x)$. In neutral situations ($c_i = \frac{1}{2}$), this is between $1\frac{1}{2} z_i(x)$ and $\frac{1}{2} z_i(x)$ (see Figure 4.7).
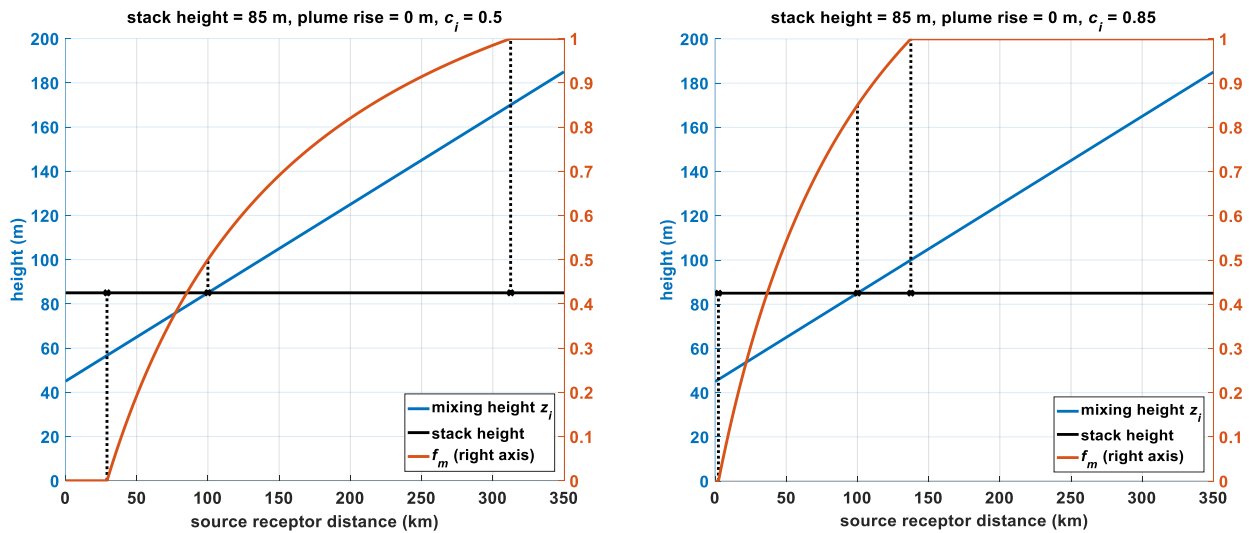
Figure 4.7. Fraction inside mixing layer f_m (red, right axis [0-1]) as function of source receptor distance. Example with rising mixing height (blue) for stable stability class S1 and stack height (black) = 85 m (left axis [0-200]). No plume rise. Left panel: c_i = 0.5, right panel: c_i = 0.85. The three dashed help lines indicate the locations where the fraction of the emitted mass inside the mixing layer = 0 (at $h_1 = (1+c_i) z_i(x)$), c_i (at $h_1 = z_i(x)$) or 1 (at $h_1 = c_i z_i(x)$).

OPS computes the concentration $c(x)$ at a receptor at distance x as follows:

$f_m(x) = 0$ → $c(x) = 0$.

$f_m(x) > 0$ → - set emission strength to a fraction of the original emission strength $= f_m Q_0$;

        - if plume (including plume rise) is released above mixing layer → set emission height of emission $f_m Q_0$ to $h_1 = z_i(x)$;

        - compute c according to Gaussian plume formulas (with reflections at $z_i(x)$).

Note that in fact OPS computes $f_m c$, instead of actually setting the source strength to $f_m Q_0$.

4.3.5   Building effect

The influence of a single building on the emitted plume can be included in the calculations of the concentration and deposition. The building influence is computed using correction factors determined offline on the basis of calculations with ISL3a (Infomil 2020). The building module in ISL3A is based on the sketch in Figure 4.8 and is described in Scholten et al. (1998).
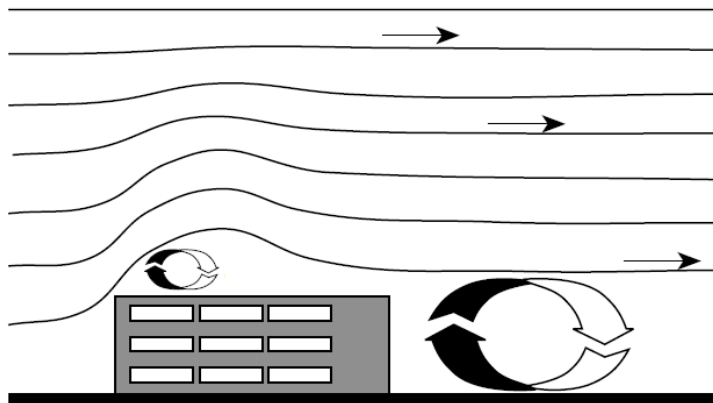
Figure 4.8. Sketch of effect of building on streamlines around the building. From Scholten et al. (1998).

The effect on deposition is assumed to be equal to the effect on concentration (in relative sense). In order to estimate the effects, runs with the Gaussian plume model ISL3A have been performed with and without the presence of a building and for different sets of input parameters. From these runs, distance-dependent, yearly averaged building factors are derived which are put into a table. To include the effect

of the building in an OPS calculation, concentrations and depositions from the OPS-model are multiplied with the factors from this pre-processed table. Further details on the building module in OPS are given in Sauter et al. (2020), available as separate PDF-document *building_effect_ops_yyyymmdd.pdf* .

4.3.6   NH₃ emissions from manure application

The DEPASS model (Dynamic Exchange of Pollutants between Air and Soil Surface) is developed in order to describe the vertical transport and diffusion in both soil and atmosphere, and the exchange of pollutants between the compartments in relation to actual meteorological conditions. The model is described in Van Jaarsveld (1996). The following correction factor (relative to the average emission strength) for the NH₃ emission strength of land-spread manure was derived on the basis of this model and using a regression analysis of emissions and meteorological parameters:

$$EC_{spread} \quad = f_1(P_p)\, f_2(R_a, R_b, T) \tag{4.8}$$

$$f_1(P_p) \quad = \min(\max(0.5, (1.069 - P_p)^2), 1.5) \tag{4.9}$$

$$f_2(R_a, R_b, T) = 1.55 \cdot 10^{-5} \left[(100 / (R_a(4) + R_b))^{0.8} (T + 23)^{2.3} \right]^{1.25}, \tag{4.10}$$

in which P_p is the rain probability [-], T is the ambient temperature [°C], $R_a(4)$ the aerodynamic resistance of the lower 4 m of the atmosphere [s/m] and R_b the pseudo-laminar layer resistance [s/m]. Basically, the effect of wind speed and atmospheric stability is included in the aerodynamic resistance. Note that soil properties, such as pH, are not taken into account here. On average, the factor varies from approx. 0.4 in January to 1.5 in July. Note that for a specific model run, the emission total may change due to this correction factor.
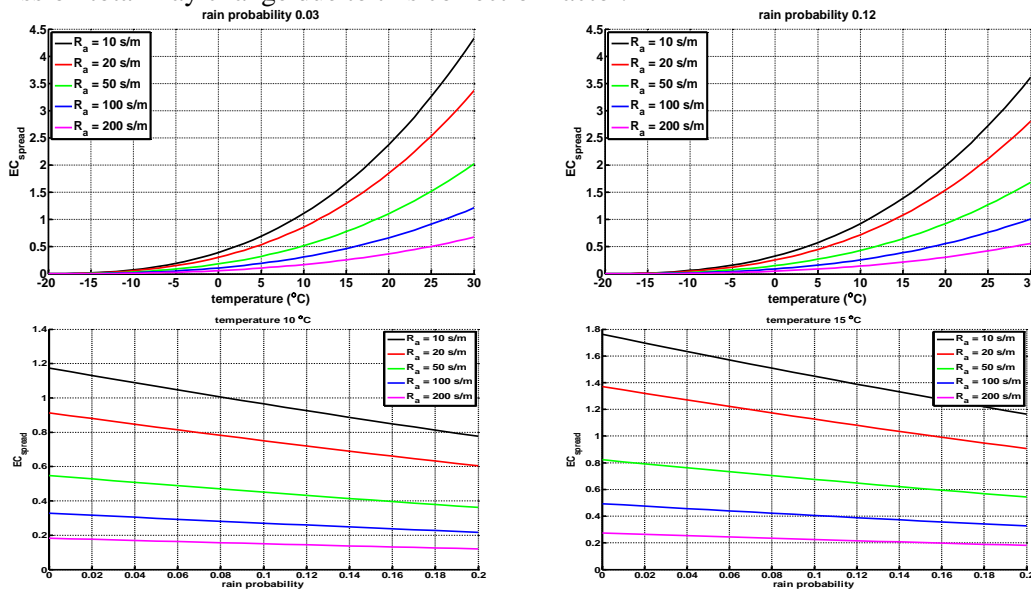

Figure 4.9   Correction factor for the NH₃ emission of land-spread manure (EC_{spread}) as function of temperature (upper panels) or rain probability (lower panels) for different values of R_a. R_b = 25 s/m.

The parameterisation of the relative emission strength of manure applied to the surface, as incorporated in the OPS model, has been first applied in a study on emission−deposition relations in the Netherlands (Van Jaarsveld *et al.*, 2000). The most striking result is the difference between the impact of emissions of animal housing systems and emissions due to land-spreading of manure. This is one of the reasons why the effect of emission reduction measures (mainly incorporating manure into the soil top layer) did not show up in measured ammonia concentrations in the Netherlands.

Besides a correction factor for land-spreading emissions describing variations in volatilisation relative to yearly averages, one might consider an activity correction factor. This is of major importance if the model is used on a monthly basis, because there is a distinct seasonal pattern in the application of

manure to the field. However, such a correction can be applied afterwards and is therefore not included in the present model.

Because the volatilisation of NO_x from applied manure and fertiliser is driven by the same processes as that of NH_3, the relationships derived for NH_3 are also applied to NO_x emissions from these activities.

4.3.7 NH₃ emissions from animal housing systems

For emissions related to animal housing systems, a dependency has been chosen on the basis of measurements of Kroodsma *et al.* (1993) and Groot Koerkamp and Elzing (1996). The correction factor is:

$$EC_{house} = \max(1 + 0.0294\ (\ T - T_{avg}\ ), 0.2) \tag{4.11}$$

where T is the outdoor temperature and T_{avg} the (long-term) average outdoor temperature (T_{avg}=10 °C).
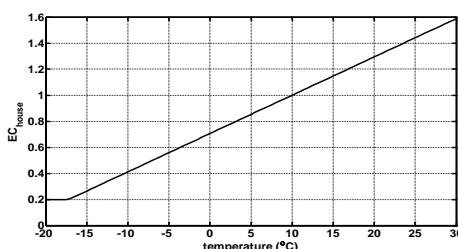

Figure 4.10   Correction factor (relative to the average emission strength) for the NH₃ emission strength of animal housing systems (EC$_{house}$) as function of temperature.

The average correction factor for emissions from animal housing systems is approximately 1.3 in July and 0.7 in January. Note that for yearly runs, the emission total for a year with an average temperature other than 10 °C, changes. This kind of emission is clearly less influenced by meteorology than landspreading emissions. The factor 0.0294 is, in fact, based on relations with indoor temperatures in a mechanically ventilated cattle-housing system. In the present model it is assumed that the temperature variations for indoor and outdoor are equal, which probably leads to an overestimation of the temperature effect. Moreover, there is also no distinction made between housing systems for cows, pigs or poultry, or between naturally or forced ventilated systems. Neither is a dependency of the ventilation rate on outdoor wind speed included.

Because the volatilisation of NO_x from animal housings is driven in the same way as that of NH_3, the relationships derived for NH_3 are also applied to NO_x emissions from animal housings.

4.4 References

Berkowicz R., Olesen H.R. and Torp U. (1986) The Danish Gaussian Air Pollution Model (OML): description, test and sensitivity analysis in view of regulatory applications. In: De Wispelaere C., Schiermeier F.A. and Gillani N.V., editors. Air pollution modeling and its application V. Plenum Press, New York. p. 453-482.

Briggs G.A. (1971) Some recent analyses of plume rise observation. Proceedings. 2nd Intern. Clean Air Congress, H.M. Englund and W.T. Berry (Eds.), Academic Press, New York, 1029-1032.

Briggs G.A. (1975) Plume rise predictions. In: Lectures on Air Pollution and Environmental Impact Analysis. American. Meteorological Society, Boston MA. 59-111.

Briggs G.A. (1982) Plume Rise Predictions. In Lectures on Air Pollution and Environmental Impact Analyses, Second printing of Workshop Proceedings, Boston, Massachusetts, Sept 29-Oct 3, 1975, pp 59-111, American Meteorological Society, Boston.

Briggs G.A. (1985) Analytical parameterisations of diffusion: The convective boundary layer. J. Climate Appl. Meteorol. 24, 1167-1186.

Groot Koerkamp, P.W.G. and Elzing A. (1996) Degradation of nitrogenous components in and volatilization of ammonia from litter in aviary housing systems for laying hens. Transactions of the ASAE, Vol. 39.

Infomil (2020), ISL3A (*In Dutch*), https://www.infomil.nl/onderwerpen/lucht-water/luchtkwaliteit/slag/isl3a/

Kroodsma, W., Huis in 't Veld, J.W.H. and Scholtens, R. (1993) Ammonia emission and its reduction from cubicle houses by flushing. Livestock Production Sci. 35:293-302.

Manins P.C. (1979) Partial penetration of an elevated inversion layer by chimney plumes. Atmospheric Environment 13, 733-741.

Moore D.J. (1987) Conditions in which power stations contribute to high ground level SO2 concentrations in the U.K. Atmospheric Environment 21, 1849-1855.

Potma C.J., Onderdelinden D. and Slanina J. (1986) Bijdrage van een kolengestookte elektriciteitscentrale aan de lokale luchtconcentratie- en depositieniveaus. PEO report NOK-LUK 3, no. 20.70-017.10, RIVM report 22822 02 004, Bilthoven.

Sauter F., van Ratingen S., Zandveld P., Visser S. (2020) Simulating the effect of a building in OPS. RIVM memo, available at www.rivm.nl/ops.

R.D.A. Scholten, J.J. Erbrink en A. van Melle (1998): Beschrijving rekenmodule voor de invloed van een gebouw op de verspreiding van een rookpluim. https://www.infomil.nl/publish/pages/67563/pb30.pdf.

TNO (1976) Modellen voor de berekening van de verspreiding van luchtverontreiniging inclusief aanbevelingen voor de waarden van parameters in het lange-termijnmodel. Staatsuitgeverij, The Hague, the Netherlands.

Turner DB, Chico T, Catalano JA (1986). Tupos, a multiple source gaussian dispersion algorithm using on-site turbulence data. Contract No. EPA 68-02-3750. Atmospheric sciences research laboratory, office of research and development, US Environmental protection agency, Research Triangle park, NC.

Van Jaarsveld J. A. (1995) Modelling the long-term atmospheric behaviour of pollutants on various spatial scales. Ph.D. Thesis, Utrecht University, the Netherlands.

Van Jaarsveld J.A. (1996) The dynamic exchange of pollutants at the air-soil interface and its impact on long range transport In: Air Pollution Modeling and its application XI, edited by Sven-Erik Gryning and Francis Schiermayer.

Van Jaarsveld, J.A., Bleeker, A. and Hoogervorst, N.J.P. (2000) Evaluatie ammoniakredukties met behulp van metingen en modelberekeningen. RIVM rapport 722108025, RIVM, Bilthoven.

Weil J.C. (1985) Updating applied diffusion models. J. Climate Appl. Meteorol. 24, 1111-1130.

5.   Dry deposition

Deposition flux and deposition velocity

The vertical transport of atmospheric contaminants - either in gaseous or in particle form - to or from the underlying surface is governed by a number of processes. Some of these are determined by atmospheric properties common to all contaminants and others by specific physical and chemical properties of the gases in conjunction with properties of the surface. The vertical exchange flux F_d in this model is described as the product of a vertical velocity v_d specified for a height z, and the difference in concentration at this height, χ_a, and the surface or substrate concentration χ_s:

$$F_d = v_d(z)[\,\chi_a(z) - \chi_s\,].$$ (5.1)

For substances which immediately react at the surface with other substances or for substances attached to particles, χ_s may be considered zero. However, for substances such as ammonia or persistent organic pollutants (POPs), χ_s may be so high under specific conditions that the vertical flux is upward (Van Jaarsveld *et al.*, 1994). In that case Eq. (5.1) describes the emission flux. For gases such as nitrogen oxide (NO) this may be the case for most ecosystems (Duyzer and Fowler, 1994). In an electrical analogue $v_d(z)$ can be represented as a contaminant conductivity, which can be expressed as the inverse of resistances:

$$v_d(z) = [\,R_a(z) + R_b + R_c\,]^{-1}.$$ (5.2)

The sequence of the three resistances represents the resistances in the three stages of vertical transport, i.e. (1) for the turbulent layer, the aerodynamic resistance R_a, (2) for the layer immediately adjacent to the surface, the pseudo-laminar layer resistance R_b, and (3) for the receptor the surface resistance R_c.

Note that OPS computes deposition at two different locations:
- along the transport trajectory (using parameters averaged along the trajectory); see section 5.2;
- at the receptor (using local parameters at the receptor's site).

Aerodynamic resistance R_a

The resistance R_a depends mainly on the local atmospheric turbulence. Hicks *et al.* (1989) assume that the atmospheric resistance to transport of gases and small particles is similar to that of heat. Here Wesely and Hicks (1977) are followed; they approximate R_a by:

$$R_a(z) = \frac{1}{\kappa\,u*}[\,\ln\,(\frac{z}{z_0}) - \psi_h(\frac{z}{L}) + \psi_h(\frac{z_0}{L})\,],$$ (5.3)

where $\psi_h(z/L)$ is the stability correction for heat, which is related to the dimensionless temperature gradient φ_h (see Eq. (3.22) and (3.23)):

$$\psi_h\left(\frac{z}{L}\right) = \int_0^{\frac{z}{L}}\left(\frac{1-\varphi_h(\zeta)}{\zeta}\right)d\zeta\ ,$$ (5.4)

which can be approximated by (Beljaars and Holtslag, 1990):

$$\psi_h(\frac{z}{L}) = 2\log\left[0.5\left(1 + \sqrt{1 - 16\frac{z}{L}}\right)\right]\ \text{for}\ L \leq 0,$$ (5.5)

$$\psi_h(\frac{z}{L}) = -0.7\frac{z}{L} - \left(0.75\frac{z}{L} - 10.72\right)\exp\left(-0.35\frac{z}{L}\right) - 10.72\ \text{for}\ L > 0.$$ (5.6)

Strictly speaking, the aerodynamic resistance is the resistance between height z and the zero plane displacement d [m], however, in OPS, d is set to zero.
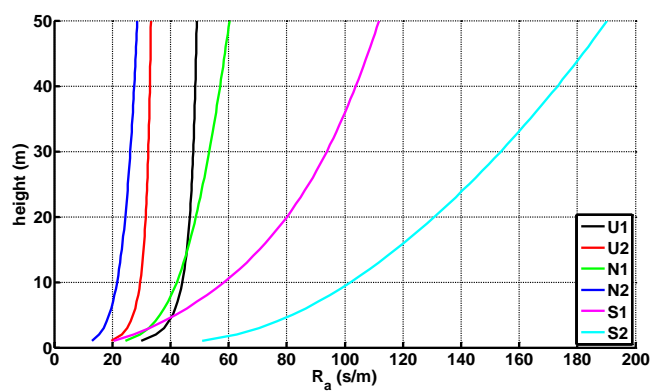
Figure 5.1 vertical profile of aerodynamic resistance for the stability/mixing height classes used in OPS. Values of u*, L are from Table 2.5

Table 2.5, $z_0 = 0.03$ m.

Pseudo-laminar layer resistance R_b

The resistance R_b depends on both turbulence characteristics and molecular diffusion of the contaminant considered. Investigations of the pseudo-laminar layer resistance show that R_b is strongly influenced by the diffusivity of the material being transferred and the rigidity of a rough surface (Garratt and Hicks, 1973; Brutsaert, 1975). The value of R_b is approximated by Wesely and Hicks (1977); Hicks *et al.* (1987):

$$R_b = \frac{2}{\kappa\, u_*}\left(\frac{N_{Sc}}{N_{Pr}}\right)^{\frac{2}{3}}, \tag{5.7}$$

where N_{Sc} and N_{Pr} are the Schmidt and Prandtl numbers respectively. N_{Pr} is ~0.72, while N_{Sc} is defined as: $N_{Sc} = v/D_g$, with v being the kinematic viscosity of air (0.15×10^{-2} m^2 s^{-1}) and D_g the molecular diffusivity in air [m^2 s^{-1}]. The pre-processor of the model calculates R_b for SO$_2$ only. Since the ratio of diffusion coefficients in air for different substances is proportional to the root of their molecule masses M_m, the ratio of their R_b values can be expressed as:

$$R_{b_i} = R_{b_j}\left(\frac{M_{m_i}}{M_{m_j}}\right)^{\frac{1}{3}}, \tag{5.8}$$

where the subscripts $_i$ and $_j$ denote substances *i* and *j*.

Surface or canopy resistance R_c

Substance and receptor characteristics determine R_c, which for vegetation can be seen as the replacement resistance of a number of other resistances such as stomatal, mesophyll, cuticular and water-layer resistances (Erisman, 1992, Wichink Kruit et al., 2007, 2010). In the case of deposition to water or bare soil, R_c represents all resistances due to diffusion and transport in the water or soil column. In OPS, the surface resistance for gases is provided by the DEPAC module (Van Zanten et al., 2010). For PM$_{10}$, deposition velocities are specified as function of the particles size, whereas for some specific acidifying aerosols, the approach of Wesely *et al.* (1985) and Ruijgrok *et al.* (1993) has been followed.

Vertical gradient

Through the depletion of material at the surface, a process of material redistribution within the mixing layer will be induced. This redistribution will be driven by vertical turbulent diffusion or, inversely, limited by the aerodynamic resistance of the lower part of the mixing layer. However in general, the net result of these competing processes is that the concentration at the surface will decrease more than the average concentration in the mixing layer. Vertical concentration gradients can be very strong, especially for substances which have a low surface resistance or during stable atmospheric conditions, when $R_a(z)$ is very large. Measurements at the Cabauw meteorological tower (Van Dop *et al.*, 1980; Onderdelinden *et al.*, 1984) confirm the existence of large gradients. For SO$_2$ under stable night-time conditions, for example, a ratio between the concentration at the 4-m level and the 100-m level of about 0.3 was found.

In a steady-state situation, the vertical deposition flux F_d in the lower part of the boundary layer can be considered as independent of height:

$$F_d(z_2) = F_d(z_1), \tag{5.9}$$

or (assuming $\chi_s = 0$):

$$v_d(z_2)\,\chi(z_2) = v_d(z_1)\,\chi(z_1). \tag{5.10}$$

The concentration ratio between the two levels z_1 and z_2 can then be given as (Van Egmond and Kesseboom, 1983):

$$g_{z_2}^{z_1} \equiv \frac{\chi(z_1)}{\chi(z_2)} = \frac{R_a(z_1) + R_b + R_c}{R_a(z_2) + R_b + R_c} .$$ (5.11)

Scriven and Fisher (1975) describe the relation of v_d with height in a similar way, however, without the stability corrections which are applied for the calculation of $R_a(z)$. For situations where the gradient is not fully developed, i.e. close to a source or when stability goes from unstable to stable, it is assumed that the atmosphere is acting in analogy to an electric capacitor which is unloaded by a resistor. The first-order time constant, τ, for such a circuit can be characterised by a simple $R_c C_c$ value, where R_c is the electrical equivalent for the aerodynamic resistance over a layer and C_c the electrical equivalent for the height of that layer. The concentration profile, which depends on the distance x to the source, can now be given as:

$$\frac{\chi(x, z_1)}{\chi(x, z_2)} = g_{z_2}^{z_1} + \left(1 - g_{z_2}^{z_1}\right)\exp\left(\frac{-t}{\tau}\right),$$ (5.12)

in which:

$$t = \frac{x}{u} \text{ and } \tau = \frac{z_1}{v_d(z_1)} .$$ (5.13)

For reason of simplicity, a single height of 50 m was chosen for z_2 in line with Van Egmond and Kesseboom (1983). This height may be considered as an upper limit for very stable situations since the nocturnal boundary layer height in such situations is also of the order of 50 m (Nieuwstadt, 1984). Values for τ can range from 8 minutes, in the case of unstable atmosphere, to more than 30 minutes in case of stable situations. A value of $z_1 = 4$ m has been fixed as receptor height in the OPS model, representative for the height of most LML stations.
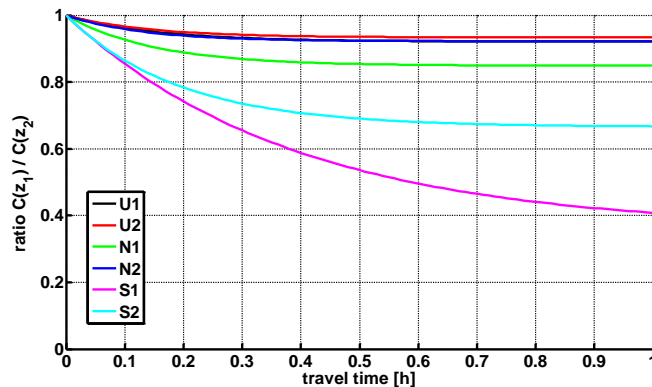
Figure 5.2 vertical concentration gradient (concentration at 4 m compared to 50 m) as function of travel time for the stability/mixing height classes used in OPS. Values of u*, L, R_a are from Table 2.5, R_b is computed according to Eq. 5.7, for $R_c = 100$ s/m, $z_0 = 0.03$ m.

5.1   Land use and roughness length

Land use and roughness length z_0 are important parameters in the modelling of dry deposition. At present, the DEPAC module contains parameterisations for the nine land-use types given in Table 5.1.

Table 5.1 Land-use classes distinguished in DEPAC with percentage of occurrence in the Netherlands.

Code	Land-use type	%
1	Grass land	**37.1**
2	Arable land	**24.3**
3	Permanent crops (orchards)	**1.2**
4	Coniferous forest	**4.2**

5	Deciduous forest	**6.2**
6	Water	**13.2**
7	Built-up area	**11.1**
8	Heather and other nature	**2.4**
9	Bare soil	**0.3**

Land use and roughness length maps are available in several resolutions, the highest at present being 250 x 250 m^2. The OPS model selects the required resolution depending on the chosen output resolution.

The land use data in the DEPAC partition are derived from basic land use data, distinguishing 39 different land use types with a resolution of 25 x 25 m^2 (LGN7, Hazeu et al. 2014). The z_0 maps with the same resolution as the land use maps are created by averaging drag coefficients for the LGN7 land use types in each grid cell. We use here the simplified form of the drag coefficient

$$C_d = \left(\frac{\kappa}{\ln\left(z_{ref}/z_0 \right)} \right)^2 ,$$

(5.14)

with κ the Von Karman constant (= 0.4), z_{ref} = 10 m.

Roughness length values for LGN land use type have been estimated in the HYDRA project (Verkaik, 2001).

Note that DEPAC is called twice in OPS: once for deposition at the receptor's site and once for the deposition along the trajectory. In the latter case, the average percentage of each land use class and average roughness are determined, averaged over 20 points along the trajectory. Up to version 4.5 of OPS, the roughness length for sample points outside the Netherlands was read from an European z_0-map (resolution 10 x 10 km^2) based on Corine Land Cover data (CLC 2000) and land use was assumed to be grass. As of version 4.5, the Dutch land use and roughness maps are extended with the adjacent part of Belgium and Germany to improve the deposition along the trajectory for foreign sources close to the Dutch border. Corine Land Cover data (CLC2006) were used for this extension. Figure 5.3 shows the dominant land use in the DEPAC partition and the roughness length for the Netherlands and neighbouring parts of Belgium and Germany.
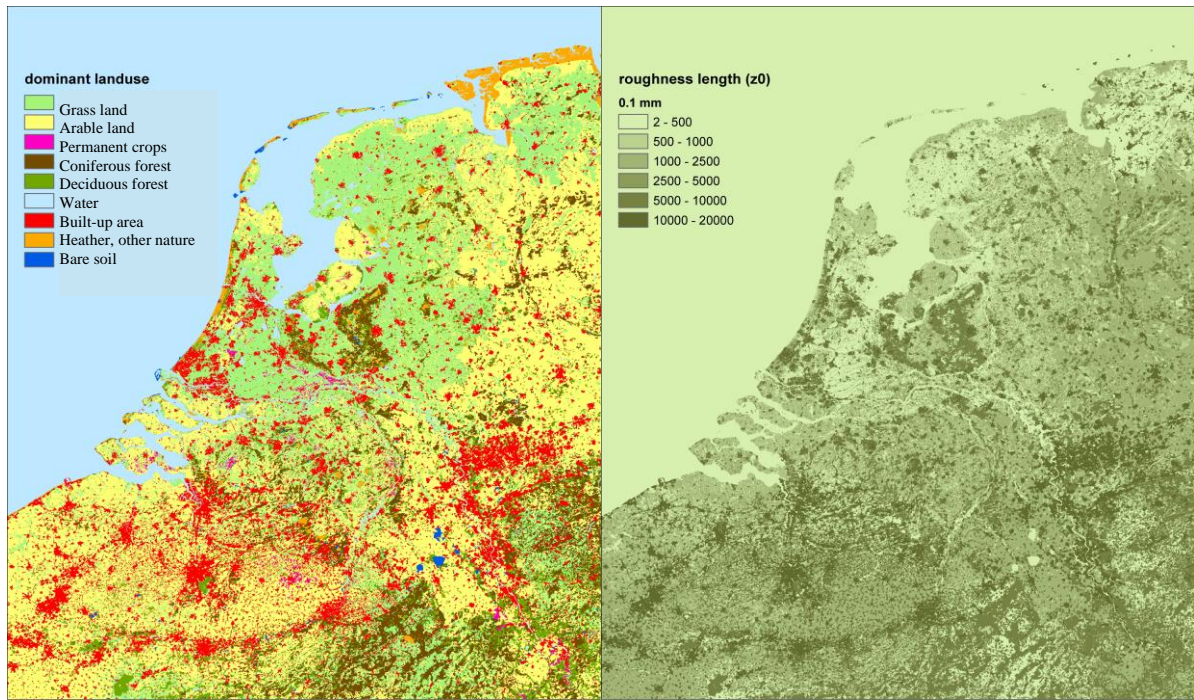
Figure 5.3: Dominant land use (DEPAC partition) and roughness length at 250 x 250 m², derived from LGN7 for the Netherlands and CLC2006 for Belgium and Germany.

For sample points outside the domain of the extended maps z_0-values are still read from the European z_0-map and land use is still assumed to be grass.

5.2   Source depletion

In OPS, the chosen approach to account for the effect of deposition on the concentration in air can be described as 'source depletion with surface correction'. Horst (1977) developed a so-called surface depletion model, in which he introduced small negative sources at the surface - representing the material lost by dry deposition - and calculated the resulting concentration profile as the sum of the contribution of the undepleted source and the contributions of the negative sources. Since the resulting concentration has to be determined numerically, the method is time consuming and as such is not suited for an analytical model as described here.

In a source depletion model, the loss of airborne material due to deposition is accounted for by appropriately reducing the source strength as a function of down-wind distance x. This is what is actually described by the following equation for the depleted source strength (or cross-wind integrated mass flux) $\widetilde{Q}(x)$ [g s⁻¹], a removal rate k [s⁻¹] and average wind speed $\overline{u}$ (averaged over the trajectory) [m s⁻¹]:

$$\widetilde{Q}(x) = Q_0 \exp\left[-k\,\frac{x}{\overline{u}}\right], \tag{5.15}$$

where Q_0 [g s⁻¹] is the undepleted source strength at $x = 0$.

A more general expression for Eq. (5.15) can be derived by computing mass fluxes in a mixing volume as shown in Figure 3.1 (dry deposition only).
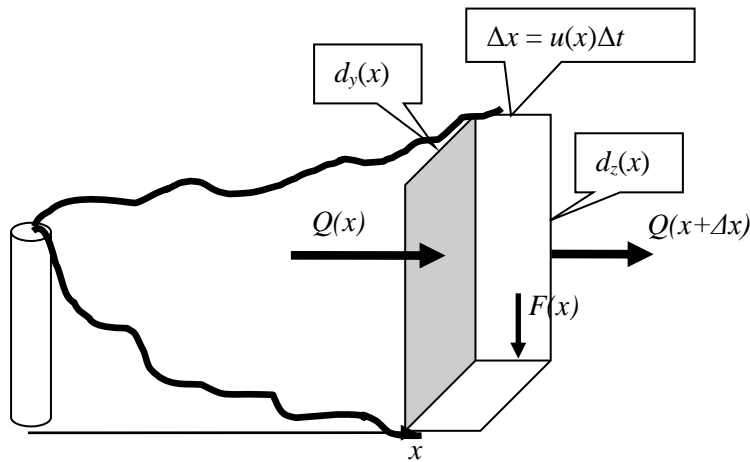
Figure 5.4 Mixing volume of plume at distance x, with mass flux Q(x) and deposition flux F(x); plume dimensions are given by Δx, dy and dz [m].

The decrease in cross-wind integrated mass flux between the left side and the right side of the box is caused by the deposition flux F [g/(m²s)]:

$$\tilde{Q}(x + \Delta x) - \tilde{Q}(x) = F(x)\,\Delta x\, d_y(x) = F(x)\,\Delta x\, \frac{1}{D_y(x)}\ . \tag{5.16}$$

The deposition flux F is (Eqs. 3.7, 3.10):

$$F(x) = -v_d\, C(x) = -v_d\, \frac{\tilde{Q}(x)}{u(x)}\, D_y(x)\, D_z(x)\ . \tag{5.17}$$

This leads to the differential equation

$$\frac{1}{\tilde{Q}(x)} \frac{d(\tilde{Q}(x))}{dx} = -\frac{v_d}{u(x)}\, D_z(x)\ , \tag{5.18}$$

with solution

$$\tilde{Q}(x) = Q_0 \exp\left[-\int_0^x \frac{v_d}{\bar{u}}\, D_z(\xi)\, d\xi \ \right]. \tag{5.19}$$

As pointed out earlier, the expression $D_z(x)$ depends on the ratio σ_z/z_i, (z_i mixing height [m]), resulting in either Eq. (3.9) or (3.15). In addition, the effective transport height has a tendency to increase with distance, also resulting in an increasing transport velocity $\bar{u}$. Therefore, the integral in Eq. (5.19) cannot be solved analytically for the entire range of x, but has to be split in two or more parts, representing the different stages in plume development from source to receptor. For this reason, three stages are distinguished:

I.   Transport within an area source with radius r_a. The vertical dispersion within such a source is characterised by $\sigma_{z,eff}(x)$ (Eq. (3.42)). This effective vertical dispersion parameter is almost independent of the position within the area source (see Figure 3.12). Therefore $D_z(x)$ is approached by:

$$D_z(x) = \frac{2}{\sqrt{2\pi}\ \sigma_{z\,eff}(x = r_a)}\ . \tag{5.20}$$

and the depleted source strength is

$$\tilde{Q}(x) = Q_0 \exp\ [\ -v_d\,(z)\,\frac{x_d}{\overline{u}}\ \frac{2}{\sqrt{2\pi}\ \sigma_{z\,eff}(x=r_a)}\ ],\qquad(5.21)$$

in which $\overline{u}$ is the transport velocity taken at $z = \sigma_{z,eff}(x)$. The effective distance x_d over which deposition takes place within an area source is (assuming that, on average, the receptor lies halfway between the centre and the edge of the area source):

$$x_d = \left(\frac{r_a}{2}\right)\exp(-kt),\qquad(5.22)$$

with k [s^{-1}] the total conversion rate for chemical conversion, wet deposition and dry deposition and t [s] the travel time from area source to receptor: $t = (r_a/2)/u$.

II.   The phase where the plume is not yet uniformly mixed in the mixing layer. This stage starts at x_s = 0 in case of a point source or at $x_s = r_a$ in the case of an area source. A separate description of this phase is especially important for low-level sources because of the enhanced ground-level concentrations close to the source. $D_z(x)$ is given by Eq. (3.15). When the reflection against the top of the mixing layer is neglected at this point (Eq. (3.15) is dominated by the last term anyway), $D_z(x)$ can be written as:

$$D_z\,(x) = \frac{2}{\sqrt{2\pi}\ \sigma_z}\ \exp\left[\frac{-h^2}{2\sigma_z^2}\right]\ .\qquad(5.23)$$

An approximation for the solution of Eq. (5.19) in combination with (5.23) is based on the assumption that $\sigma_z^2 = 2K_z\ x\,/\,u$ (see 3.24), with the turbulent eddy diffusivity K_z [m^2/s], which does not depend on the distance x. In appendix 5.5.1, the following expression is derived for the source depletion ratio between x_s and x:

$$\frac{\tilde{Q}(x)}{Q(x_s)} = \exp\left\{-\frac{2\beta\,v_d(z)\,(x-x_s)}{\overline{u}}\ \frac{x\,C(x)\,u(x)}{Q_0}\ \frac{2\pi}{m_s}\right\},\qquad(5.24)$$

in which $\overline{u}$ is the average transport speed (averaged over the trajectory), $u(x)$ the wind speed at the location of the receptor and at transport height and

$$\beta = \frac{8\sigma_z^2}{\pi h^2\left(1+\sqrt{1+\dfrac{8\sigma_z^2}{\pi h^2}}\right)^2}.\qquad(5.25)$$

III.   The phase where the plume is uniformly mixed in the mixing layer. This phase starts at a distance x_g from the source, where σ_z equals the (local) mixing height z_i. This distance is usually less than 50 km for stacks emitting inside the mixing layer (see Figure 5.5). For high stacks emitting above the mixing layer and in stable situations, this distance can be much larger.
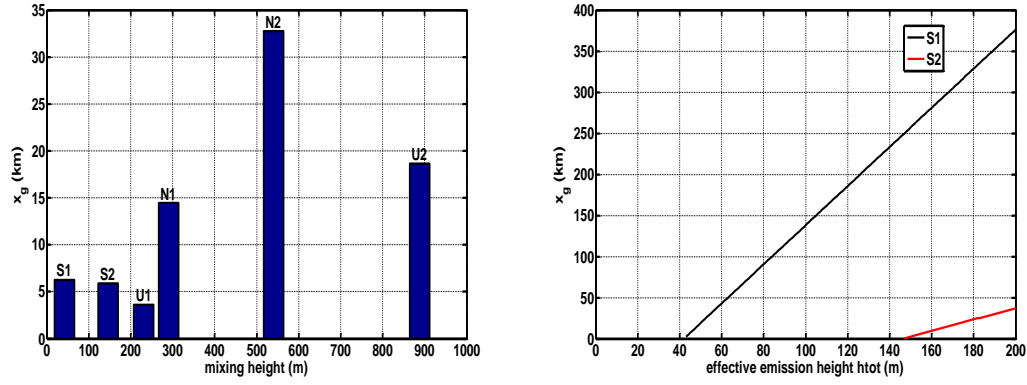
Figure 5.5   Distance x_g (m), where the plume is fully mixed, for different stability classes in OPS; mixing height from Table 2.5. Left panel: for a low stack (height 10 m) emitting inside the mixing layer; x-axis = average mixing height of the meteo class (m). Right panel: for a high stack emitting above the mixing layer, stability classes S1 and S2 (stable classes with mixing heights of 42 and 146 m resp.); x-axis = effective emission height. Here we assumed that the mixing height at 100 km is 2 times the local mixing height.

$D_z(x,h)$ can now be written as:

$$D_z(x) = \frac{1}{z_{i\,max}}$$

(5.26)

and the depleted source strength is

$$\tilde{Q}(x) = Q_0 \exp\left(-v_d(z)\frac{x - x_g}{\overline{u}\,z_{i\,max}} \right),$$

(5.27)

where $\overline{u}$ is the transport velocity taken at $z = z_{i,max}/2$.

As is pointed out earlier in section 1.3.3, the mixing height $z_{i,max}$ is a function of the transport distance x. Transport times can be of the order of days, where several diurnal cycles in mixing height and aerodynamic resistances can occur. To compensate for these effects on the source depletion ratio, $v_d(z)$ is corrected with a factor $f_d(x,h)$ (see Eq. (2.25), which is determined in the meteorological pre-processor.

For the three phases of the plume, various transport velocities are applied, depending on the height of the centre of the plume mass. Also the height for which v_d is specified depends on the phase of the plume. In principle, v_d has to be specified for the lowest height where the vertical concentration distribution is not yet disturbed by the dry deposition process. In phase I (inside area source), v_d is taken at $z = 4$ m. For phase II (Gaussian plume, no gradient due to deposition), v_d is taken at $z = 0$ m, while for phase III (well-mixed) v_d is taken at $z = 50$ m. The vertical profile correction (Eq. 5.12) is started at the beginning of phase II, but has most of its effects in phase III.

The source depletion ratio at a (large) distance from an area source, due to dry deposition, is calculated as the product of the depletion ratios in the different stages of plume development.

5.3   Dry deposition of non-acidifying substances

Dry deposition is simulated in the OPS model by means of the so-called resistance model. Three resistances ([s/m]) in series determine the deposition velocity here:

-   the aerodynamic resistance R_a
-   the laminar boundary layer resistance R_b
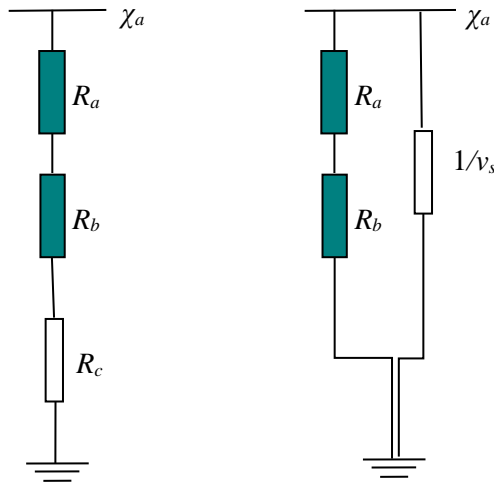-   the surface resistance R_c .

Figure 5.6   Standard resistance approach used in OPS (left panel) and resistance approach for heavy particles (right panel), where there is a separate path with a settling (sedimentation) velocity v_s.

The deposition (or exchange) velocity [m/s] is given by:

$$v_d = (R_a + R_b + R_c)^{-1} \tag{5.28}$$

where R_a and R_b are calculated when the meteorological statistics for a certain period/area are made, and as such form part of these statistics; R_c has to be specified by the user for the substance he/she wishes to calculate as an average over the period to be considered. As an alternative, an average deposition velocity v_d, may be input, whereby the model calculates R_c using average values of R_a and R_b. In this way, the specific R_a and R_b for a particular stability class can still be used. The average v_d, which can be entered in the above manner, has an upper limit, because $R_c \geq 0$ s/m, which means that the upper limit of v_d is in the order of 0.035 m/s.

Dry deposition of particulate substances is entirely related to the dimensions of the particles. The deposition velocities for the particle-size classes have been determined using data from Slinn (1982). Here, the logarithmic class mean has consistently been seen as representative of all particle diameters in a class. In the class with the largest particles (> 20 μm), 40 μm was taken as representative value. If sedimentation plays a role, we use a different resistance approach, shown in the right panel of Figure 5.6, with a sedimentation velocity v_s [m/s], which is computed using Stokes law:

$$v_s = \frac{\left(\rho_p - \rho_{air}\right)D_p^2\, g}{18\mu}, \tag{5.29}$$

with

v_s : sedimentation or terminal settling velocity [m/s]

ρ_p : density of particle ~ 1000 kg/m³

ρ_{air} : density of air = 1.293 kg/m³ (0 °C), 1.205 kg/m³ (20 °C)

D_p : diameter of particle [m]

g   : acceleration of gravity = 9.807 m/s²

μ   : viscosity of air = 1.81·10^{-5} kg /(s m).

The effective deposition velocity is only influenced by the distribution of the substance over the particle-size classes. The deposition velocities concerned (weighted over the various stability/mixing height classes) are given in Table 5.2.

Table 5.2   Dry deposition parameters for 6 particle classes. (2): D = mass median diameter. (3) Rc: canopy resistance. (4): deposition velocity according to Sehmel & Hodgson (1980). (5) sedimentation velocity. (6)-(8) standard particle-size distributions. The canopy resistance Rc has been derived from 1/vd(Slinn) – Ra – Rb, with Ra and Rb aerodynamic and boundary layer resistances, weighed over all stability/mixing height classes (Ra at 4 m height; grass, z0 = 0.15 m).

	class		1	2	3	4	5	6
1.	size range	μm	<0.95	0.95-2.5	2.5-4	4-10	10-20	>20
2.	*D*	μm	0.2	1.6	3	6	14	40
3.	R_c	s/m	3200	700	150	50	2	-17[(1)]
4.	v_d	cm/s	0.03	0.13	0.46	0.9	2.4	5.4
5.	v_s	cm/s	0.00	0.01	0.03	0.11	0.59	4.8
6.	fine	%	70	12	8	5.5	2.5	2
7.	medium	%	53	16	12	11.5	4.2	3.3
8.	coarse	%	42	19	14	14.5	5.9	4.6

(1) not used; for class 6, the resistance scheme according to Figure 5.6, right panel is used.

5.4   Dry deposition of acidifying and eutrophying substances, DEPAC

5.4.1   Dry deposition of gaseous substances

In the case of the gases SO_2, NO, NO_2, HNO_3 and NH_3, the OPS model uses the deposition module DEPAC (DEPosition of Acidifying Compounds) for the parameterisation of the canopy resistance R_c (van Zanten et al., 2010). This module was developed by Erisman *et al.* (1994) on the basis of experimental data such as those derived from the Speulder forest experiments and it uses a resistance analogy in order to model the deposition fluxes (see Figure 5.7). For gases emitted by sources at the surface level, such as NH_3, the resistance analogy can only be used if a non-zero surface concentration is taken into account. Such a concentration is sometimes referred to as the compensation point.

The compensation point concentration may vary strongly with vegetation type and soil properties, and preceding deposition/emission fluxes. In Wichink Kruit et al. (2010, 2012 and 2017), parameterisations of the different compensation points have been proposed and these have been implemented in the deposition module DEPAC (Van Zanten et al., 2010). The compensation point for surface water is related to the water temperature and the molar ratio between NH_4^+ and H^+ in the water (Γ_{water} in DEPAC). Long term average maps of this ratio have been derived for the large water bodies in the Netherlands and the North Sea (Wichink Kruit et al., 2024). These maps are used in OPS.

Codeposition is the process of enhanced NH_3 deposition in the presence of SO_2 due to a higher surface acidity (Flechard et al., 1999). Conversely, the absence of SO_2 can also lead to a decrease in NH_3 deposition. This depends on the (molar) ratio between SO_2 and NH_3. The EMEP model (Simpson et al., 2012) takes into account the codeposition process through a resistance that describes the

exchange with the external leaf surface, based on work by Nemitz et al. (2001). As the DEPAC module in OPS is based on compensation points, the acidity ratio used in the description of the external leaf surface resistance in EMEP, is implemented as a variable in the external leaf surface compensation point in DEPAC.
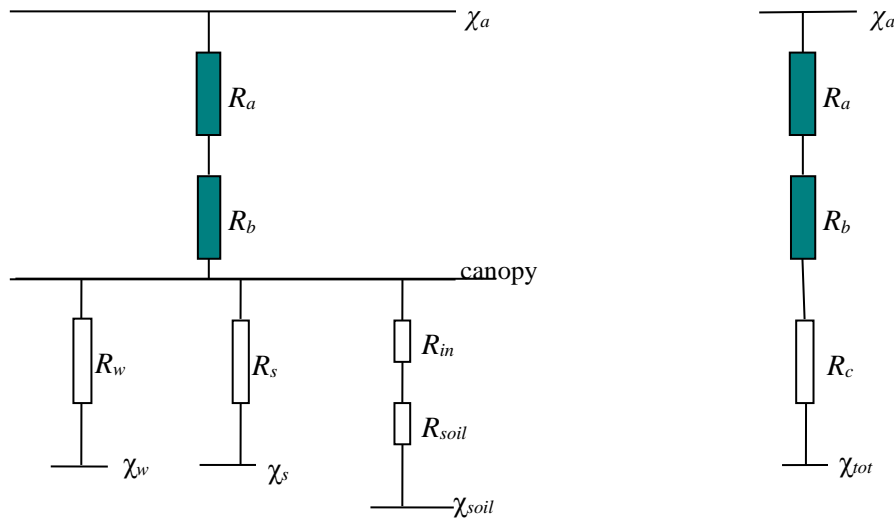

Figure 5.7   Flux/resistance model for dry deposition in the DEPAC module, with atmospheric concentration χ_a, resistances R and compensation points χ. Three pathways are taken into account: through the stomata (subscript s), the external leaf surface (water layer or cuticular waxes, subscript w) and the soil (subscript soil). R_{inc} is the in canopy resistance. Left panel: scheme with separate resistances and compensation points. Right panel: equivalent scheme with a replacement resistance R_c and total compensation point χ_{tot} as defined in text.

Only for NH_3 the full scheme is used; for other components, we assume the compensation points to be zero. If no information is available on the different deposition pathways, we use one replacement resistance R_c.

In this deposition model, R_{stom} represents the stomatal resistance of leaves. R_{inc} and R_{soil} are resistances representing in-canopy vertical transport to the soil that bypasses leaves and branches. R_w is an external resistance that represents transport via leaf and stem surfaces, especially when these surfaces are wet. The canopy resistance R_c and the effective compensation point χ_{tot} are calculated as:

$$R_c = \left(\frac{1}{R_w} + \frac{1}{R_{inc} + R_{soil}} + \frac{1}{R_s} \right)^{-1} , \tag{5.30}$$

$$\chi_{tot} = \left[\frac{R_c}{R_w} \chi_w + \frac{R_c}{R_{inc} + R_{soil}} \chi_{soil} + \frac{R_c}{R_s} \chi_s \right] . \tag{5.31}$$

The DEPAC module contains values or formulae for each of the resistances below the canopy and for various land-use types. The module includes the following gaseous components: SO_2, NO, NO_2, NH_3 and O_3 and provides a canopy resistance on an hourly basis as a function of meteorological parameters, day of the year and time of the day. The day of year is used in the parameterisation of the leaf area index and the surface water compensation point. In OPS-LT, DEPAC is called for day 15 in a 'representative month', which has been tested to represent the average over 12 separate month-runs.

NH$_3$ deposition on land use class 'arable land' varies so much that two representative months are needed (see Table 5.3) of which the resulting resistances are averaged to calculate the yearly deposition. Because there is no reason to assume that the underlying mechanism does not hold for SO$_2$ and NO$_x$, the same months are used for these components.

Table 5.3 Representative month(s) for which DEPAC is called, for different run-types, land use and species.

type of run	land use	species	representative month(s)
year	arable land	SO$_2$, NO$_x$, NH$_3$	April, July
year	other than arable	SO$_2$, NO$_x$, NH$_3$	May
winter	all	SO$_2$, NO$_x$, NH$_3$	November
summer	all	SO$_2$, NO$_x$, NH$_3$	June
month	all	SO$_2$, NO$_x$, NH$_3$	actual month

Meteorological parameters needed as input are: temperature, friction velocity, global radiation, solar elevation, relative humidity and a surface wetness indicator. In OPS-LT, stability/mixing height class averaged values are used. The solar elevation is derived from a fit on hourly data of global radiation Q [W/m^2] in The Netherlands, where cloudy hours are filtered out:

$$sin(\phi) = 2.37 \cdot 10^{-3}Q - 1.86 \cdot 10^{-6}Q^2. \tag{5.32}$$
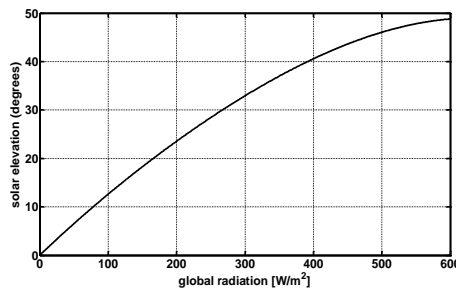

Figure 5.8   Solar elevation (degrees) as function of global radiation [W/m^2].

The surface wetness indicator is needed, because dry deposition velocities of SO$_2$ and NH$_3$ are much higher when the surface is wet. Due to the nature of the OPS-LT model, it is not straightforward to decide if a certain meteo class is to be labelled 'wet' or 'dry'. The following empirical relation connects the average relative humidity *RH* (in %) and precipitation probability P_r to the wetness indicator:

$$nwet = \frac{(0.4\,P_r + 0.017\,RH - 0.4)^5}{3.33}. \tag{5.33}$$

The surface is assumed 'wet' if *nwet* > 0.5, otherwise it is dry. Expression (5.33) is derived from surface wetness observations in the Speulder forest. The switch point of (5.33) for zero P_r, lies around *RH* = 87 %. This means that the surface is supposed to be wet in approx. 50% of the time.
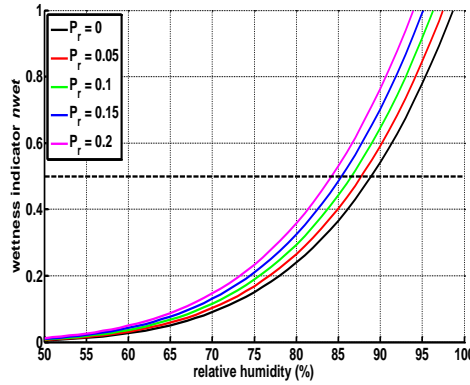
Figure 5.9   Wetness indicator nwet as function of relative humidity RH for different values of precipitation probability Pr. In the source code, nwet is rounded to 0 (dry) or 1 (wet).

Three extra input parameters are needed for the NH_3 compensation point: (1) atmospheric NH_3 concentration averaged over a previous period (e.g. previous year or month); (2) actual atmospheric NH_3 concentration; (3) atmospheric SO_2 concentration averaged over a previous period. The last one is needed fort the codeposition process. Since actual concentrations are not available in OPS-LT, these parameters are represented by the background concentration (see section 7.3). This implies that it is possible that emissions take place via the external leaf pathway, whereas for hour-by-hour calculations (using actual concentrations in the parameterisation of the external compensation point), there is no emission via the external leaf path (deposition is only reduced).

Output of the DEPAC module is the canopy resistance R_c and the total compensation point χ_{tot}. In general, after the call to DEPAC, the (hourly) deposition flux F can be computed as:

$$F = -v_d \cdot (\chi_a - \chi_{tot}), \tag{5.34}$$

with deposition (exchange) velocity

$$v_d = \frac{1}{R_a + R_b + R_c}. \tag{5.35}$$

For OPS-LT however, an alternative expression has been chosen:

$$F = -v_d' \cdot \chi_a, \tag{5.36}$$

$$v_d' = \frac{1}{R_a + R_b + R_c'} = v_d \left(\frac{\chi_a - \chi_{tot}}{\chi_a}\right), \tag{5.37}$$

with R_c' the effective canopy resistance, which is also an output of the DEPAC module:

$$R_c' = \left(\frac{(R_a + R_b)\chi_{tot} + R_c\chi_a}{(\chi_a - \chi_{tot})}\right). \tag{5.38}$$

In the rare case that R_c' is negative (re-emission over the whole of the stability/mixing height class), OPS-LT resets R_c' to a large value of 1000 s/m.

Up to OPS version 4.3.16, the DEPAC routine is called with as argument the **dominant** land use of the grid cell for which the local deposition has to be calculated. This can give rise to inconsistencies between the aerodynamic resistance R_a and the canopy resistance R_c in case of grid cells with varying land use, because the former is based on the grid **averaged** roughness value z_0. From OPS-version

4.5.2 on, DEPAC is called for each of the land use classes occurring over a trajectory or in the receptor grid cell, upon which the average dry deposition velocity v_d is calculated from the resulting R_c values as follows:

$$\overline{v_d} = \sum_i f_i \frac{1}{R_a + R_b + R_{c,i}} .$$

(5.39)

with $R_{c,i}$ the (effective) R_c value of land use class i and f_i the fraction of occurrence of class i in the concerned grid cell.

Further details on DEPAC, such as the parameterisation of different resistances and compensation points, are given in Van Zanten et al. 2010.

5.4.2   Dry deposition of NO_x

In this model NO_x represents the sum of NO, NO_2, PAN and HNO_2. The DEPAC module provides estimates of the canopy resistances of NO and NO_2; for HNO_2, dry deposition velocities similar to those of SO_2 have been suggested by Wesely (1989). Erisman (1992) estimated the average dry deposition of HNO_2 in the Netherlands at less than 6 % of the total dry deposition of all oxidised nitrogen components. Dry deposition properties for PAN are assumed to be the same as for NO_2. The canopy resistance for NO_x is now calculated as:

$$R_c(NO_x) = \frac{1}{a} - R_a - R_b$$

(5.40)

with

$$a = \frac{r_{n,eff}}{R_c(NO_2) + R_a + R_b} + \frac{1 - r_{n,eff}}{R_c(NO) + R_a + R_b} + \frac{f_{HNO_2}}{R_c(HNO_2) + R_a + R_b} ,$$

(5.41)

where $r_{n,eff}$ is the NO_2/NO_x ratio and f_{HNO2} is the fraction of HNO_2 in NO_x taken at a fixed value of 0.04. R_a is calculated for a height of 4 m. The atmospheric resistances R_a and R_b are included in this calculation only as weighting factors because the calculation of a species weighted R_c has to be carried out on the basis of deposition velocities and not on resistances.

5.4.3   Dry deposition of acidifying aerosols

The route to forming particles containing SO_4^{2-}, NO_3^- and NH_4^+ runs through direct gas-to-particle conversion and evaporation of cloud droplets in which conversion has previously taken place. Newly formed particles are usually smaller than 0.01 μm (Aitken particles). If the gas condenses on existing particles (e.g. heterogeneous processes), the median size of these particles will also be relatively small, because small particles have the highest specific surface area. Through processes such as coagulation, small particles will grow and finally be concentrated in a 0.1– 1 μm range, the so-called accumulation mode. Most theoretical models suggest a deposition velocity v_d between 0.05 - 0.2 cm/s for this size range and relatively smooth surfaces ($z_0 < 0.1$ m). Data from the literature suggest that for rough surfaces such as forests, the dry deposition velocity will be significantly higher, for example, in the order of 1 cm/s (Voldner *et al*., 1986; Erisman *et al*., 1994).

A different approach has been followed for acidifying aerosols such as SO_4^-, NO_3^- and NH_4^+ than for aerosols or particles in general. One reason is that there is more experimental data available which makes it possible to distinguish between vegetation types; another reason is that particle-sizes are usually small

since the particles have been formed in the atmosphere and are thus independent of industrial processes or cleaning equipment.

Basically, the dry deposition of particles is modelled using empirical relations. These relations describe the vertical movement of small particles at or within the canopy. The empirical relations can be fitted into a common resistance approach according to Figure 5.10.
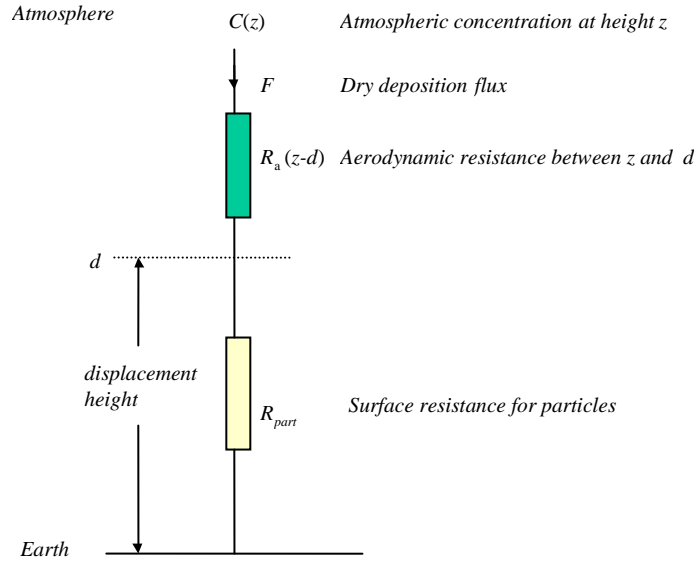
Atmosphere $C(z)$ *Atmospheric concentration at height z*

                              F *Dry deposition flux*

                              $R_a(z\text{-}d)$ *Aerodynamic resistance between z and d*

d

displacement height

                              R_{part} *Surface resistance for particles*

Earth

Figure 5.10   Resistance model for acidifying aerosols.

In this model the effects of all canopy-related processes are included in R_{part}. Together with the aerodynamic resistance it can be included in a dispersion model just as the resistance model for gases. The dry deposition velocity for small particles is then calculated as:

$$v_{d\_part} = \frac{1}{R_a(z-d) + R_{part}},$$
(5.42)

with d the displacement height [m]. In OPS, the displacement height is neglected ($d = 0$ m).

For roughness lengths below 0.5 m, the particle 'canopy' resistance is modelled according to Wesely *et al.* (1985):

$$R_{part}^{-1} = \frac{u*}{500}\left(1+\left(\frac{300}{-L}\right)^{\frac{2}{3}}\right) \qquad if \quad L < 0$$
(5.43)

$$R_{part}^{-1} = \frac{u*}{500} \qquad\qquad\qquad if \quad L > 0,$$
(5.44)

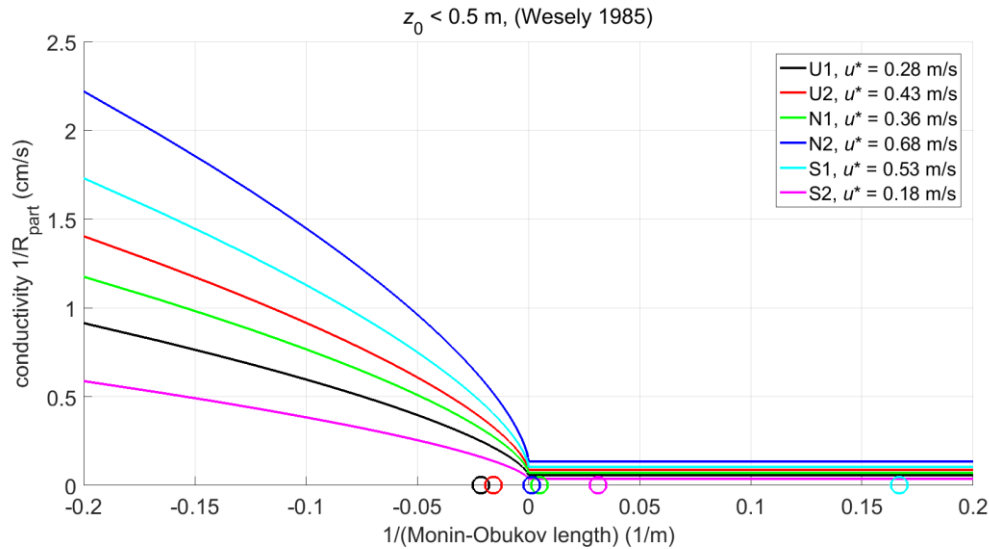with friction velocity $u*$ [m/s] and Monin-Obukhov length L [m].

Figure 5.11   Conductivity $1/R_{part}$ for particles as function of $1/$(Monin-Obukhov length); roughness length < 0.5 m. Values for u from Table 2.5, values for $1/L$, indicated by circles at x-axis, from the same table.*

For forested areas and areas with roughness lengths above 0.5 m, R_{part} is parameterised according to Ruijgrok *et al*. (1993):

$$R_{part}{}^{-1} = \frac{E\,(u*)^2}{u_h} \; , \tag{5.45}$$

where u_h represents the wind speed at canopy height (m s^{-1}) and E a particle collection efficiency:

$$E = a\,(u*)^b \;\; , \text{ for RH} \leq 80\,\% \tag{5.46}$$

$$E = a\,(u*)^b \left(1 + c\,\exp^{\left(\frac{RH-80}{20}\right)} \right), \text{ for RH} > 80\,\%, \tag{5.47}$$

with *RH* the relative humidity [%] and *a, b, c* coefficients defined in Table 5.4.

Table 5.4 Coefficients of the collection efficiency parameterisation.

	a		*b*		*c*	
	Dry	Wet	Dry	Wet	Dry	Wet
SO_4	0.05	0.08	0.28	0.45	0.18	0.37
NO_3	0.063	0.10	0.25	0.43	0.18	0.37
NH_4	0.05	0.066	0.23	0.41	0.18	0.37

5.4.4   Dry deposition of NO_3^- + HNO_3

The model describes the transport of only one secondary substance. In the case of nitrogen oxides the secondary substance consists of $NO_3{}^{total}$ (= NO_3^- + HNO_3), which has very different dry deposition velocities and therefore very different atmospheric lifetimes. NO_3^- aerosol is the dominant species under European conditions. The model uses a dry deposition velocity adjusted to f_{HNO3}, which is an empirically determined $HNO_3/NO_3{}^{total}$ ratio (Eq. 7.12). Similar to the dry deposition of NO_x, the canopy resistance for $NO_3{}^{total}$ is determined by:

$$R_c(\text{NO}_3\text{t}) = \frac{1}{b} - R_a - R_b \,, \tag{5.48}$$

with

$$b = \frac{f_{\text{HNO}_3}}{R_c(\text{HNO}_3) + R_a + R_b} \; + \; \frac{1 - f_{\text{HNO}_3}}{R_c(\text{NO}_3) + R_a + R_b} \,, \tag{5.49}$$

where $R_c(\text{NO}_3)$ is computed as R_{part} above. $R_c(\text{HNO}_3)$ is taken as 10 s/m under all conditions.

5.5 Appendix

5.5.1 Derivation of the source depletion ratio for phase II of a plume

We start from the expression for the depleted source strength (Eq. 5.19) and for the dispersion factor $D_z(x)$ for phase II of the plume (Eq. 5.23):

$$\tilde{Q}(x) = Q_0 \exp\left[-\int_0^x \frac{v_d(z)}{\bar{u}} D_z(\xi)\, d\xi\right] = Q_0 \exp\left[-\int_0^x \frac{v_d(z)}{\bar{u}} \frac{2}{\sqrt{2\pi}\,\sigma_z} \exp\left[\frac{-h^2}{2\sigma_z^2}\right] d\xi\right] \,.$$

Acccording to Eq. 3.24, $\sigma_z^2 = 2K_z t = 2K_z \dfrac{\xi}{u}$, with travel time [s] $t = \xi/u$ and turbulent eddy diffusivity K_z [m^2/s], that does not depend on the distance ξ.

Substitution of σ as function of ξ in the integral (for convenience we drop the subscript z):

$$\sigma^2 = \frac{2K_z \xi}{u} \Rightarrow 2\sigma\, d\sigma = \frac{2K_z}{u} d\xi$$

$$\tilde{Q}(x) = Q_0 \exp\left[-\frac{u}{K_z} \int_0^{\sigma(x)} \frac{v_d(z)}{\bar{u}} \frac{2}{\sqrt{2\pi}} \exp\left[\frac{-h^2}{2\sigma^2}\right] d\sigma\right]$$

Define:

$$I = \int_0^{\sigma(x)} \exp\left[\frac{-h^2}{2\sigma^2}\right] d\sigma$$

and substitute

$$y = \frac{h}{\sqrt{2}\,\sigma}, \, dy = \frac{-h}{\sqrt{2}\,\sigma^2} d\sigma = \frac{-\sqrt{2}}{h} y^2 d\sigma :$$

$$I = \frac{h}{\sqrt{2}} \int_{\frac{h}{\sqrt{2}\sigma}}^{\infty} \frac{\exp\left[-y^2\right]}{y^2} dy \,.$$

Integration by parts and using the abbreviation $p = \dfrac{h}{\sqrt{2}\,\sigma}$ leads to

$$I = \frac{h}{\sqrt{2}} \int_p^{\infty} \exp\left(-y^2\right) \cdot \left(\frac{1}{y^2}\right) dy = \frac{h}{\sqrt{2}} \left[\exp\left(-y^2\right)\left(\frac{-1}{y}\right)\right]_p^{\infty} - \int_p^{\infty} (-2y)\exp\left(-y^2\right)\left(\frac{-1}{y}\right) dy =$$

$$= \frac{h}{\sqrt{2}} \left\{ \frac{\exp(-p^2)}{p} - 2 \int_p^\infty \exp(-y^2)\, dy \right\} .$$

The integral term, can be approximated as follows:

$$\int_p^\infty \exp(-y^2)\, dy = \frac{1}{2} \sqrt{\pi}\ \mathrm{erfc}(p) \approx \frac{\exp(-p^2)}{p + \sqrt{p^2 + \dfrac{4}{\pi}}} \ , \text{ for } p > 0.$$

(Abramowitz & Stegun (1970), 7.1.13).

$$I = \frac{h}{\sqrt{2}} \left\{ \frac{1}{p} \exp(-p^2) - \frac{2\exp(-p^2)}{p + \sqrt{p^2 + \dfrac{4}{\pi}}} \right\} = \frac{h}{\sqrt{2}} \exp(-p^2) \left\{ \frac{1}{p} - \frac{2}{p + \sqrt{p^2 + \dfrac{4}{\pi}}} \right\} =$$

$$= \frac{h}{\sqrt{2}} \exp(-p^2) \left\{ \frac{\left(p + \sqrt{p^2 + \dfrac{4}{\pi}}\right) - 2p}{p\left(p + \sqrt{p^2 + \dfrac{4}{\pi}}\right)} \right\} = \frac{h}{\sqrt{2}} \exp(-p^2) \left\{ \frac{\sqrt{p^2 + \dfrac{4}{\pi}} - p}{p\left(p + \sqrt{p^2 + \dfrac{4}{\pi}}\right)} \right\} =$$

$$= \frac{h}{\sqrt{2}} \exp(-p^2) \left\{ \frac{\left(\sqrt{p^2 + \dfrac{4}{\pi}} - p\right)\left(p + \sqrt{p^2 + \dfrac{4}{\pi}}\right)}{p\left(p + \sqrt{p^2 + \dfrac{4}{\pi}}\right)^2} \right\} = \frac{h}{\sqrt{2}} \exp(-p^2) \left\{ \frac{p^2 + \dfrac{4}{\pi} - p^2}{p\left(p + \sqrt{p^2 + \dfrac{4}{\pi}}\right)^2} \right\} =$$

$$= \frac{h}{\sqrt{2}} \frac{\exp(-p^2)}{p} \left\{ \frac{\dfrac{4}{\pi}}{\left(p + \sqrt{p^2 + \dfrac{4}{\pi}}\right)^2} \right\} = \frac{h}{\sqrt{2}} \frac{\beta \exp(-p^2)}{p} , \text{ with}$$

$$\beta = \frac{\dfrac{4}{\pi}}{\left(p + \sqrt{p^2 + \dfrac{4}{\pi}}\right)^2} = \frac{\dfrac{4}{\pi}\dfrac{1}{p^2}}{\left(1 + \sqrt{1 + \dfrac{4}{\pi}\dfrac{1}{p^2}}\right)^2} = \frac{8\sigma^2}{\pi h^2 \left(1 + \sqrt{1 + \dfrac{8\sigma^2}{\pi h^2}}\right)^2} .$$

The depleted source strength can be written as:

$$\tilde{Q}(x) = Q_0 \exp\left[-\frac{u}{K_z} \frac{v_d(z)}{\bar{u}} \frac{2}{\sqrt{2\pi}} I\right] = Q_0 \exp\left[-\frac{u}{K_z} \frac{v_d(z)}{\bar{u}} \frac{2}{\sqrt{2\pi}} \frac{h}{\sqrt{2}} \frac{\beta \exp(-p^2)}{p}\right].$$

Substitute $K_z = \frac{1}{2} \frac{u}{x} \sigma^2$ and $p = \frac{h}{\sqrt{2}\,\sigma}$:

$$\tilde{Q}(x) = Q_0 \exp\left[-\frac{2x}{\sigma^2} \frac{v_d(z)}{\bar{u}} \frac{2}{\sqrt{2\pi}} \frac{h}{\sqrt{2}} \frac{\sqrt{2}\sigma}{h} \beta \exp\left(-\frac{h^2}{2\sigma^2}\right)\right] =$$

$$= Q_0 \exp\left[-\frac{4x}{\sqrt{2\pi}\,\sigma} \frac{v_d(z)}{\bar{u}} \beta \exp\left(-\frac{h^2}{2\sigma^2}\right)\right].$$

The source depletion ratio is:

$$\frac{\widetilde{Q}(x)}{Q(x_s)} = \exp\left\{-v_d(z)\frac{x-x_s}{\overline{u}}\frac{4\beta}{\sqrt{2\pi}\,\sigma_z}\exp\left[\frac{-h^2}{2\sigma_z^2}\right]\right\}$$

$$= \exp\left\{-v_d(z)\frac{x-x_s}{\overline{u}}2\beta\,D_z(x)\right\},$$

Substituting Eq. (3.7):

$$D_z(x) = \frac{C(x)\,u(x)}{Q_0\,D_y(x)} = \frac{C(x)u(x)}{Q_0}\frac{2\pi x}{m_s}\,,$$

we get:

$$\frac{\widetilde{Q}(x)}{Q(x_s)} = \exp\left\{-\frac{2\beta\,v_d(z)\,(x-x_s)}{\overline{u}}\frac{x\,C(x)\,u(x)}{Q_0}\frac{2\pi}{m_s}\right\}.$$

in which $\overline{u}$ is the average transport speed (averaged over the trajectory) and $u(x)$ the wind speed at the location of the receptor and at transport height.

The advantage of the latter expression is that we now have an expression in $C(x)$ instead of σ_z. The error introduced by neglecting mixing height reflections will be greatly reduced in this way.

5.6   References

Abramowitz, Milton; Stegun, Irene A., eds. (1970), Handbook of Mathematical Functions with Formulas, Graphs, and Mathematical Tables, New York: Dover Publications, SBN 486-61272-4, see also http://people.math.sfu.ca/~cbm/aands/

Beljaars A.C.M. and Holtslag A.A.M. (1990) A software library for the calculation of surface fluxes over land and sea. *Environ. Software* **5**, 60-68.

Brutsaert W.P. (1975) The roughness length of water vapour, sensible heat and other scalars. *J. Atmos. Sci.* **32**, 2028-2031.

Duyzer J.H. and Fowler D. (1994) Modelling land atmosphere exchange of gaseous oxides of nitrogen in Europe. *Tellus* **46B**, 353-372.

Erisman J.W. (1992) Atmospheric deposition of acidifying compounds in the Netherlands. [PhD thesis]. Utrecht University, the Netherlands.

Erisman J.W., Pul W.A.J. van and Wyers G.P (1994) Parameterization of surface resistance for the quantification of atmospheric deposition of acidifying pollutants and ozone. *Atmospheric Environment* **28**, 2595-2607.

Flechard, C.R., Fowler, D., Sutton, M.A., Cape, J.N., 1999. A dynamic chemical model of bi-directional ammonia exchange between semi-natural vegetation and the atmosphere. *Quarterly Journal of the Royal Meteorological Society* **125**, pp. 2611-2641. https://doi.org/10.1002/qj.49712555914

Garratt J.R. and Hicks B.B. (1973) Momentum, heat and water vapour transfer to and from natural and artificial surfaces. *Q. J. R. Meteorol. Soc.* **99**, 680-687.

Hazeu G.W., Schuiling C., Dorland G.J., Roerink G.J., Naeff H.S.D. & Smidt R.A. (2014) Landelijk Grondgebruiksbestand Nederland versie 7 (LGN7). Vervaardiging, nauwkeurigheid en gebruik. Rapport 2548, Alterra Wageningen UR, Wageningen. (http://content.alterra.wur.nl/Webdocs/PDFFiles/Alterrarapporten/AlterraRapport2548.pdf)

Hicks B.B., Baldocchi D.D. Meyers T.P., Hosker Jr. R.P. and Matt D.R. (1987) A preliminary multiple resistance routine for deriving dry deposition velocities from measured quantities. *Water Air Soil Pollut.* **36**, 311-330.

Hicks B.B., Matt D.R. and McMillen R.T. (1989) A micrometeorological investigation of surface exchange of O_3, SO_2 and NO_2: a case study. *Boundary-Layer Meteorol.* **47**, 321-336.

Horst T. W. (1977) A surface depletion model for deposition from a Gaussian plume. *Atmospheric Environment* **11**, 41-46.

Nemitz, E., Milford, C., Sutton, M.A., 2001. A two-layer canopy compensation point model for describing bi-directional biosphere-atmosphere exchange of ammonia. *Quarterly Journal of the Royal Meteorological Society* **127**, 815-833.

Nieuwstadt F.T.M. (1984) Some aspects of the turbulent stable boundary layer. *Boundary-Layer Meteorol.* **30**, 31-55.

Onderdelinden D., Jaarsveld J.A. van and Egmond N.D. van (1984) Bepaling van de depositie van zwavelverbindingen in Nederland. RIVM, Bilthoven, the Netherlands. Report no. 842017001.

Onderdelinden (1985): Source depletion model, personal communication in OPS archive.

Ruijgrok W., Nicholson K.W., and Davidson C.I. (1993) Dry deposition of particles. In: Lövblad G., Erisman J.W. and Fowler D., editors. Models and methods for the quantification of atmospheric input to ecosystems. Nordic Council of Ministers, Copenhagen.

Scriven R.A. and Fisher B.E.A. (1975) The long range transport of airborne material and its removal by deposition and washout - I. General considerations. *Atmospheric Environment* **9**, 49-58.

Sehmel G.A. and Hodgson W.H. (1980) A model for predicting dry deposition of particles and gases to environmental surfaces. AIChE Symposium Series 86, 218-230.

Simpson, D., Fagerli, H., Jonson, J.E., Tsyro, S., Wind, P., Tuovinen J.-P., 2003. Transboundary Acidification, Eutrophication and Ground Level Ozone in Europe. *Unified EMEP Model Description. EMEP Status Report 1/2003 Part 1, EMEP/ MSC-W Report.* Norwegian Meteorological Institute, Oslo, Norway, 74 pp.

Slinn W.G.N (1982) Predictions for particle deposition to vegetative surfaces. *Atmospheric Environment* **16**, 1785-1794.

Van Dop H., Ridder T.B., Tonkelaar J.F. den and Egmond N.D. van (1980) Sulfur dioxide measurements on the 213 metre tower at Cabauw, the Netherlands. *Atmospheric Environment* **14**, 933-946.

Van Egmond N.D. and Kesseboom H. (1983) Mesoscale air pollution dispersion models I: Eulerian Grid Model. *Atmospheric Environment* **17**, 257-265.

Van Jaarsveld J.A., Pul W.A.J. van and Leeuw F.A.A.M. de (1994) Modelling the long range transport and deposition of persistent organic pollutants over Europe and its surrounding marine areas. In: Gryning S.E. and Millán M.M., editors. *Air pollution modelling and its application X.* Plenum Press, New York. p. 143-155.

Van Zanten M.C., Sauter F.J., Wichink Kruit R.J., van Jaarsveld J.A., van Pul W.A.J.: Description of the DEPAC module, Dry deposition modelling with DEPAC_GCN2010, *RIVM report 680180001*, RIVM, Bilthoven, 2010

Verkaik, J.W. (2001): A method for the geographical interpolation of wind speed over heterogeneous terrain, KNMI report, http://www.knmi.nl/samenw/hydra/documents/geograph/interpol.pdf

Voldner E.C., Barrie L.A. and Sirois A. (1986) A literature review of dry deposition of oxides of sulphur and nitrogen with emphasis on long-range transport modelling in North America. *Atmospheric Environment* **20**, 2101-2123.

Wesely M.L. and Hicks, B.B. (1977) Some factors that effect the deposition rates of sulfur dioxide and similar gases on vegetation. *J. Air Pollut. Control Assoc.* **27**, 1110-1116.

Wesely M.L., Cook D.R., Hart R.L. and Speer R.E. (1985) Measurements and parameterization of particulate sulfur dry deposition over grass. *J.Geophys. Res.,* **90**(D1):2131-2143.

Wesely M.L. (1989) Parameterization of surface resistances to gaseous dry deposition in regional scale numerical models. *Atmospheric Environment* **23**, 1293-1304.

Wichink Kruit, R.J., W.A.J. van Pul, R.P. Otjes, P. Hofschreuder, A.F.G. Jacobs and A.A.M. Holtslag (2007) Ammonia fluxes and derived canopy compensation points over non-fertilized agricultural grassland in The Netherlands using the new gradient ammonia - high accuracy - monitor (GRAHAM). Atmospheric Environment 41: 1275-1287.

Wichink Kruit, R.J., W.AJ. van Pul, F.J. Sauter, M. van den Broek, E. Nemitz, M.A. Sutton, M. Krol and A.A.M. Holtslag (2010) Modeling the surface-atmosphere exchange of ammonia. Atmospheric Environment, Vol. 44, 7: 877-1004.

Wichink Kruit, R. J., M. Schaap, F.J. Sauter, M.C. van Zanten, and A.J. van Pul (2012) Modeling the distribution of ammonia across Europe including bi-directional surface-atmosphere exchange, Biogeosciences, 9, 5261-5277, https://doi.org/10.5194/bg-9-5261-2012.

Wichink Kruit, R. J., Aben, J., de Vries, W., Sauter, F., van der Swaluw, E., van Zanten, M. C., and van Pul, W. A. J.: Modelling trends in ammonia in the Netherlands over the 1990-2014, Atmos. Environ., 154, 20-30, https://doi.org/10.1016/j.atmosenv.2017.01.031, 2017.

Wichink Kruit, R.J., A. Bleeker, C. Jacobs, P. Meijer, M. Poelhuis, K. Siteur, A. Stolk, E. van der Swaluw, R. Verweij, W. de Vries, A. van Pul (2024). Ammoniak van Zee. Samenvatting van het onderzoek naar de onderschatting van de ammoniakconcentraties langs de kust. RIVM Rapport 2024-0095.

6. Wet deposition

Although the wet deposition process is complex, an attempt has been made to use as simple a parameterisation as possible, which can be applied more-or-less universally for both long-range transport and more local deposition. Two main scavenging processes are distinguished in this model: below-cloud scavenging and in-cloud scavenging. Below-cloud scavenging is important for scavenging from plumes close to sources in situations where there is no interaction with clouds yet. The rate limiting process is formed by diffusion of the substance through the pseudo-laminar air layer around the falling raindrop (Levine and Schwartz, 1982). In general, in-cloud processes are responsible for the highest wet deposition loads (Hales, 1978).

6.1   In-cloud scavenging

Natural storms are complex in their microphysical and dynamical structure and relations between concentrations in precipitation and the surrounding air are very variable (Barrie, 1992). Modelling of the precipitation process in transport models is usually done using either linear scavenging ratios or a numerical approach, including all the physical and chemical details of the process; there are hardly any solutions in between. The present model describes the in-cloud scavenging as a statistical process rather than as single events. The process is viewed as a discontinuous flow reactor, in which chemicals in air entering a precipitation system are transferred to other chemicals and/or precipitation. At a large distance from the source, where the pollutant is well vertically mixed and has also had the opportunity to penetrate into the cloud base, the scavenging rate of a pollutant Λ_{in} (h^{-1}) is given by:

$$\Lambda_{in} = \frac{W\,R_i}{h}\,,$$ (6.1)

where R_i is the precipitation intensity [m h^{-1}], W the ratio between the (initial) concentration in precipitation and the (initial) concentration in air [-], both on a weight/volume basis and at the ground level. Parameter h is the height over which wet deposition takes place [m]:

$$h = \begin{cases} 2\sigma_z, & \text{plume completely above the mixing layer} \\ z_i, & \text{otherwise,} \end{cases}$$ (6.2)

with σ_z the vertical dispersion length of the plume [m] and z_i the mixing height [m].

This formulation, when used with an empirically determined W, integrates, in fact, all the processes in and below the cloud.

User specified substance
Either a scavenging ratio W [-] or a scavenging rate Λ_{in} [h^{-1}][1] is to be specified by the user. W may have been determined either empirically from concentrations in rainwater and air or theoretically via Henry's constant.

SO_2
Scavenging ratios for SO_2 have been determined from experiments. Haul (1978) derived a ratio of $8\cdot10^4$ from hourly measurements of SO_2 and rainfall rates in the UK. Other authors used simultaneous observations of SO_2 and SO_4^{2-} in air and precipitation to estimate scavenging ratios of both SO_2 and SO_4^{2-} (e.g. Misra *et al.*, 1985; Chan and Chung, 1986). Chan and Chung report annual scavenging ratios of $4.3\cdot10^5$ (SO_4^{2-}), $4.6\cdot10^4$ (SO_2), $4.7\cdot10^5$ (NO_3^-) and $4.7\cdot10^5$ (HNO_3) for rural sites in the province of Ontario, Canada. Barrie (1981) expresses the scavenging ratio of SO_2 on the basis of equilibrium chemistry:

---

[1] in OPS input file to be specified in %/h

$$\log_{10}(W(\mathrm{SO_2})) = \log_{10}(K_e) + \mathrm{pH},$$ (6.3)

where K_e is an equilibrium constant related to the temperature in the following empirical relation: $K_e = 6.22 \times 10^{-8} \exp(4755.5/T)$ (mol l^{-1}). For pH = 4.75 and T = 283 K this results in $W = 7.5 \times 10^4$. A model study carried out by Scire and Venkatram (1985) supports the order of magnitude of these figures.

In OPS, the parameterisation of the SO_2 scavenging ratio is based on background concentrations of NH_3 and SO_2. An expression using NH_3/SO_2 concentration ratios that approaches Eq. (6.3) to a large extent is:

$$W(\mathrm{SO_2}) = 5 \cdot 10^4 \left(\frac{[\mathrm{NH_3}]}{[\mathrm{SO_2}]} \right),$$ (6.4)

where $[NH_3]$ and $[SO_2]$ are local concentration levels expressed in ppb (van Jaarsveld, 2004).

NO$_x$

NO and NO_2 have low water solubilities and their aqueous-phase nitrite and nitrate reactions are expected to be of only minor importance (Seinfeld, 1986). However, nitrogen compounds not explicitly taken into account in OPS, e.g. nitrous acid HNO_2, may contribute significantly to nitrate forming in the aqueous phase. These contributions to the wet deposition of NO_x are included in the model by assuming an HNO_2 scavenging ratio of $3.3 \cdot 10^5$ and an average HNO_2 fraction in NO_2 of 4%. The average NO_2 scavenging ratio = 0.04 x $3.3 \cdot 10^5 = 1.3 \cdot 10^4$. The scavenging ratio depends linearly on the NO_2/NO_x ratio; assuming an average NO_2/NO_x ratio of 0.65, the effective scavenging ratio for NO_x in OPS is $2 \cdot 10^4 \cdot [NO_2]/[NO_x]$.

NH$_3$

NH_3 is relatively well soluble in water. Due to reactions in droplets, the effective uptake of NH_3 is highly improved and, in fact, limited by the diffusivity of NH_3 in air. Measurements of NH_4^+ concentrations in precipitation confirm the effectiveness of the scavenging process. There is a clear (spatial) correlation between NH_3 concentrations in air and NH_4^+ concentrations in precipitation (Van Jaarsveld et al., 2000). The OPS model uses an in-cloud scavenging ratio $W = 1.4 \cdot 10^6$.

particles

OPS uses fixed scavenging ratios for each particle class, based on van Jaarsveld & Onderdelinden (1986), ranging from $2.4 \cdot 10^5$ for small particles to $9 \cdot 10^6$ for coarse particles (see Table 6.2).

For SO_4^{2-}, NO_3^- and NH_4^+ aerosols, scavenging ratios $W(\mathrm{SO_4^{2-}}) = 2.0 \cdot 10^6$, $W(\mathrm{NO_3^-}) = W(\mathrm{NH_4^+}) = 1.4 \cdot 10^7$ are used, which means that within the duration of a single precipitation event, most of the particles will be scavenged. Similar high scavenging ratios have been derived from field experiments. The particle size dependency, as noted for below-cloud scavenging, is probably less pronounced for in-cloud scavenging.

6.2 Below-cloud scavenging

This process is only taken into account in the first few kilometres down-wind from a source; in the further transport stage, the scavenging process is treated as an in-cloud process parameterised with a bulk scavenging ratio. For short transport distances - where there is generally still no interaction between a plume and clouds - the scavenging of gases is determined by the flux of pollutant to falling raindrops. Local below-cloud scavenging of secondary-formed products is ignored, because the contribution to total scavenging will be very low.

6.2.1 Below-cloud scavenging of gases

This model uses the parameterisation of Janssen and Ten Brink (1985), who related the below-cloud scavenging rate Λ_b [h^{-1}] to the precipitation intensity using the drop-size spectrum of Best (1950); we assume also that in-cloud scavenging is more efficient than below-cloud:

$$\Lambda_b = \min(\alpha_1 D_g^{\alpha_2} R_i^{\alpha_3}, \Lambda_{in}),$$ (6.5)

where D_g is the molecular diffusion coefficient of the species in air (cm^2 s^{-1}) and α_1, α_2 and α_3 parameters depending on the drop-size distribution. For a lower limit of the drop-size distribution of 0.125 mm, α_1 has a value of 1.21, $\alpha_2 = 0.744$ and $\alpha_3 = 0.628$; D_g is expressed in cm^{2}s^{-1}, R_i (for the given values of α's) in mm h^{-1} and Λ_b in h^{-1}. The below-cloud scavenging rate during precipitation for a highly soluble gas like HCl will, according to Eq. (6.5), amount to 0.45 h^{-1} ($D_g = 0.19$ cm^2 s^{-1} and $R_i = 1.5$ mm h^{-1}). In contrast to elevated SO$_2$ plumes, irreversibly soluble gases such as HCl show a maximum wet deposition flux within a few hundred metres. This is also in agreement with results of the washout experiments of Ten Brink et al. (1988).

User specified substance
The below-cloud scavenging rate of gases readily soluble in water is entirely parameterised by a molecular diffusion coefficient in air (D_g in cm^2.s^{-1}), which can be specified by the user. If not specified by the user, the model estimates D_g from (Durham et al., 1981):

$$D_g = k\, M^{-0.5},$$
(6.6)

where M is the molecular weight [g/mol] and k is a conversion constant ($k = 1$ cm^2 s^{-1} g$^{1/2}$ mol$^{-1/2}$). Washout of sparingly soluble gases is not incorporated in this model because of its small contribution to the total wet deposition.

SO$_2$
In the case of SO$_2$, the process of uptake is controlled by the (slow) conversion to bisulphite (HSO$_3^-$) in the falling raindrop, which means that the SO$_2$ concentration in the drop is in (near) equilibrium with the surrounding air (Barrie, 1978; Ten Brink et al., 1988). The approach used in this model for below-cloud equilibrium scavenging, avoids the washout peaks near sources as observed for irreversibly soluble gases (Ten Brink et al., 1988), but ignores vertical redistribution of plumes. At larger distances from a source, in-cloud scavenging will dominate the total wet deposition anyway (Hales, 1978). The molecular diffusion coefficient for SO$_2$ used in OPS is 0.136 cm^2 s^{-1} (Barrie, 1978).

NO$_x$
Local below-cloud scavenging is assumed to be of minor importance for NO$_x$, because primary emitted NO$_x$ species have low water solubility.

NH$_3$
Eq. 6.5 is used, with molecular diffusion coefficient $D_g = 1/\sqrt{M(\mathrm{NH_3})} = 1/\sqrt{17} = 0.24$ cm^2 s^{-1}.

6.2.2 Below-cloud scavenging of particles

Wet scavenging of aerosols is an efficient process (Slinn, 1982). Falling raindrops collide with aerosol particles and collect them. Basic mechanisms are impaction, interception and Brownian motion, indicating that there is a strong dependency on particle size as well as drop size. For the below-cloud scavenging rate Λ_b [h^{-1}] of particles an expression given by Janssen and Ten Brink (1985) has been adopted, which is similar to that of gases:

$$\Lambda_b = \alpha_4\, \varepsilon\, R_i^{\alpha_5}$$
(6.7)

where α_4 and α_5 are drop-size distribution dependent parameters and ε is the particle-droplet collision efficiency, which is a function of both particle size and droplet size. For the same conditions as defined for Eq. (6.5), α_4 has a value of 1.326 and $\alpha_5 = 0.816$. The ε values used have been given by Slinn (1982) as a function of droplet size and range for 1 mm droplets from unity for large particles (> 10 μm) down to 10^{-4} for particles in the 0.1-1 μm diameter range. In Figure 6.1, ε is plotted as a function of particle size and drop size using semi-empirical relations given by Slinn (1982). See also Table 6.2 for ε values for the 6 particle classes in OPS .
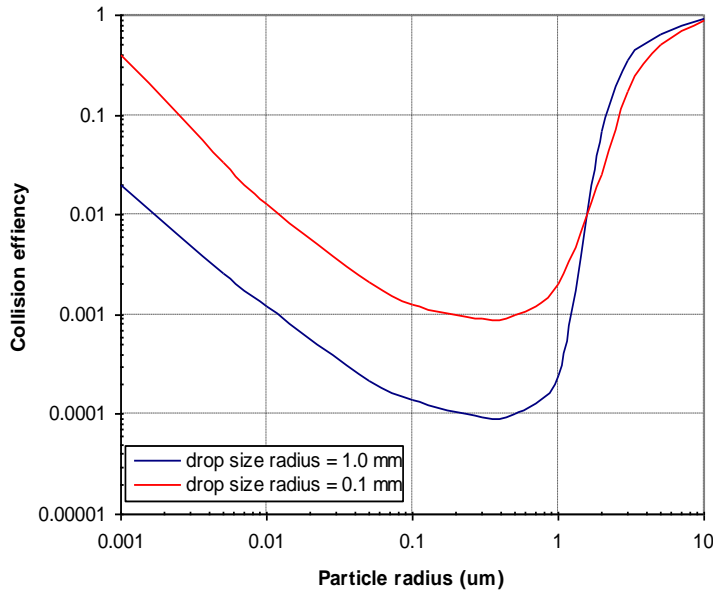
Figure 6.1 Semi-empirical relation between the collision efficiency ε and collected particle sizes for two drop sizes (Slinn, 1982).

For the below cloud scavenging rate of SO_4^{2-}, NO_3^- and NH_4^+ aerosols we use Eq. (6.7), with ε = 0.31 (corresponding to particle size class 4 in Table 6.2).

6.3 Effects of dry and wet periods on average scavenging rates

The scavenging rates $\Lambda = \Lambda_{in}$, Λ_b [h^{-1}] as defined so far, refer to situations during precipitation events. What really needs describing is the wet deposition as an average for a large number of cases, including situations with no precipitation at all and situations with extended rainfall. When significant amounts of a pollutant are removed by single precipitation events, then we cannot simply use a time-averaged scavenging rate but have to account for the statistical distribution of wet and dry periods (Rodhe and Grandell, 1972). Here, it is assumed that rain events occur according to a Poisson distribution. The change in airborne pollutant mass M in time due to wet deposition is then found as (Van Egmond et al., 1986):

$$\frac{\mathrm{d}M}{\mathrm{d}t} = -\frac{M}{(\tau_w + \tau_d)}[1 - \exp(-\Lambda\tau_w)],$$

(6.8)

with τ_w being the average length of rainfall periods and τ_d the average length of dry periods, related to the probability of wet deposition P_p by $P_p = \tau_w/(\tau_w + \tau_d)$.

P_p and τ_w are determined from hourly observations of rainfall amount and duration at 12 stations, where rainfall duration is measured with a 6-min resolution. In the current version of the model, P_p and τ_w are used with no spatial variation. Dependency on wind direction and stability is however, taken into account. It should be pointed out in this context that values for τ_w and P_p are derived from Eulerian rainfall statistics, while they are used for a characterisation of wet deposition in a Lagrangian reference frame. Hamrud et al. (1981) found little difference between Eulerian and Lagrangian statistics by following trajectories along observation sites. Because they based their conclusions on data with a 6-h resolution, it is not certain that these findings are also valid for our case with the higher time resolution. Due to lack of

information, we assume that for large distances the Lagrangian (τ_w) and Eulerian ($\tau_{w,\ Euler}$) lengths of rainfall periods are equal.

Monthly mean P_p values calculated from 12-year KNMI observations vary from 0.040 in August to 0.10 in December; $\tau_{w,Euler}$ values vary from 1.3 h in August to 2.5 h in March. Rodhe and Grandell (1972) found much higher $\tau_{w,Euler}$ values in Sweden: 9 h in winter and 4 h in summer. However, they based their calculations on two-hourly values of precipitation amounts. If the model is fed by 6-hourly synoptical data, then it is not possible to calculate τ_w from the data. In such a case, fixed monthly values are used, derived from the above mentioned KNMI data.

In OPS, the following expression for τ_w is used:

$$\tau_w = \max\left(\tau_{w,Euler}\,[\,1 - \exp(-\frac{0.4\frac{x}{u}}{\tau_{w,Euler}})\,],\ 0.1 \right). \tag{6.9}$$

The effect of this expression at short distances x is that $\tau_w \approx 0.4\frac{x}{u}$; for large distances, τ_w is equal to $\tau_{w,Euler}$.
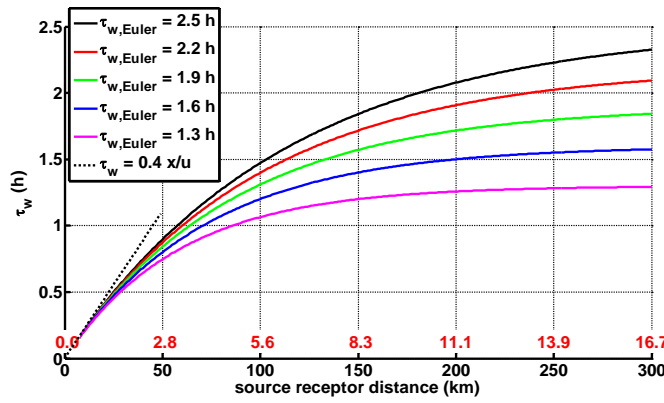

Figure 6.2   Average length of rainfall periods τ_w as function of source receptor distance for different values of $\tau_{w,Euler}$ (ranging from 1.3 to 2.5 h).Wind speed 5 m/s. In red the travel times in h.

The resulting effective scavenging rate Λ_{eff} [h^{-1}] is given by:

$$\Lambda_{eff} = \frac{P_p}{\tau_w}\,[\,1 - \exp(-\Lambda\,\tau_w)\,]. \tag{6.10}$$

At short distances x, we have $\tau_w \approx 0.4\frac{x}{u}$; this means that scavenging is not during the whole rain period, but only during 0.4 times the travel time. In this case, τ_w is small and

$$\Lambda_{eff} = \frac{P_p}{\tau_w}\,[\,1 - \exp(-\Lambda\,\tau_w)\,] \approx \frac{P_p}{\tau_w}\,[\,1 - (1 - \Lambda\,\tau_w)\,] = \Lambda P_p \quad \text{('continuous drizzle approach').}$$
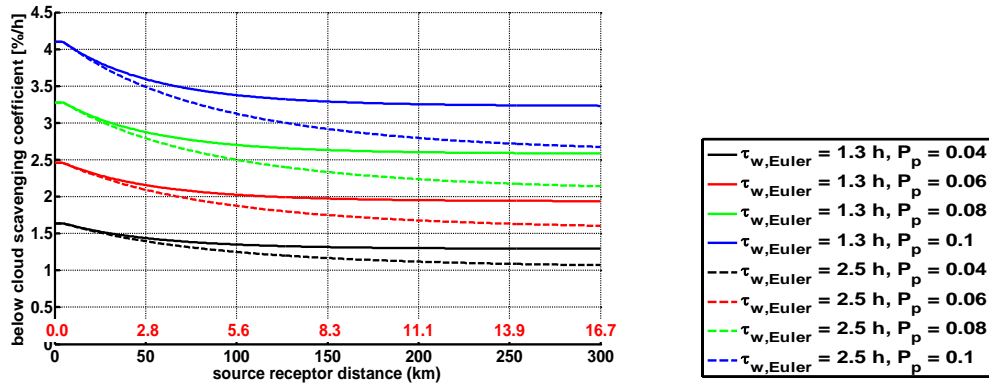
Figure 6.3   Below cloud scavenging coefficient [%/h] as function of source receptor distance for different values of $\tau_{w,Euler}$ and precipitation probability P_p. Rain intensity 1 mm/h, wind speed 5 m/s, molecular diffusion coefficient of NH₃. In red the travel times in h.

The approach for calculating effective deposition rates on the basis of Poisson-distributed dry and wet periods as given here is checked against average rates obtained from an hour-by-hour approach in section 4.2 of van Jaarsveld (1995). Van Jaarsveld also shows that for short distances the drizzle approach is acceptable.

This model requires as input, W at the beginning of a shower (Eq. 6.1). On the basis of Poisson distributed dry and wet periods, Van Jaarsveld and Onderdelinden (1986) have given a relation between this W and W's derived from measurements of average concentrations in air and rain:

$$W_{avg} = \frac{z_i}{R_i\,\tau_w}\,[\,1 - \exp(-\frac{W\,R_i}{z_i}\,\tau_w)\,]\,.$$ (6.11)

This relation sets a clear upper limit on average scavenging ratios. Assuming $z_i = 1000$ m, $R_i = 1.3 \cdot 10^{-3}$ m/h, $\tau_w = 2.7$ h and $W \to \infty$, W_{avg} will be $2.8 \cdot 10^5$. Much higher W_{avg} values derived from measurements may indicate erroneous results. For substances very effectively scavenged ($\Lambda \to \infty$), Λ_{eff} will become equal to $1/(\tau_w + \tau_d)$. This means that wet deposition will be determined by the number of rain events in a certain period rather than by the amount or duration of rainfall.

6.4   Combined in-cloud and below-cloud scavenging

The combined below- and in-cloud scavenging rate is usually much higher than the below-cloud scavenging rate. On the other hand, in-cloud scavenging can only have effect if the pollutant is able to penetrate clouds. Plumes from high stacks and especially those with additional plume rise will be sucked more into convective clouds than surface-based plumes. The time scale on which plumes reach the cloud base is tentatively taken as the time in which the vertical dimension of plumes will grow equal to the difference between the effective plume height and the assumed cloud base height, where the cloud base height is taken equal to the mixing height. In addition, a processing time within the cloud is assumed before full in-cloud scavenging can take place. This time can be translated into an additional shift Δz in the distance between stack and cloud base. This results in the following expression for the wet scavenging rate of irreversibly (superscript i) soluble substances $\Lambda_{w,eff}^{i}$ [h^{-1}], describing the gradual change from below-cloud scavenging ($pr = 0$), to in-cloud scavenging ($pr = 1$):

$$\Lambda_{w,eff}^{i} = \Lambda_{in,eff}\,pr + \Lambda_{b,eff}\,(1 - pr),\quad ,\; pr = \exp\left[-\frac{(h' + \Delta z)^2}{2\,\sigma_z^2\,c_w}\right]$$ (6.12)

with $\Delta z = 5$ m and where h' and c_w are defined as:

point sources: $\qquad h' = \max(0, z_i - h); \qquad\qquad c_w = 1$

within area sources: $h' = z_i - h + \sigma_z \left(\dfrac{s_a/2 - x}{s_a/2} - 1\right); c_w = 3$, $\qquad$ (6.13)

outside area sources: $h' = z_i - h - \dfrac{s_a^3}{1600\ x^2}; \qquad\qquad c_w = 1.$

For short travel times $t = x/u$ [h] (shorter than 1 hour, close to the source), we use an extra correction to correct for the fact that in a very small plume with high concentrations there is no instantaneous wet scavenging of all material:

$$pr = pr \cdot t, \quad 0 < t < 1\,\text{h}. \qquad\qquad (6.14)$$
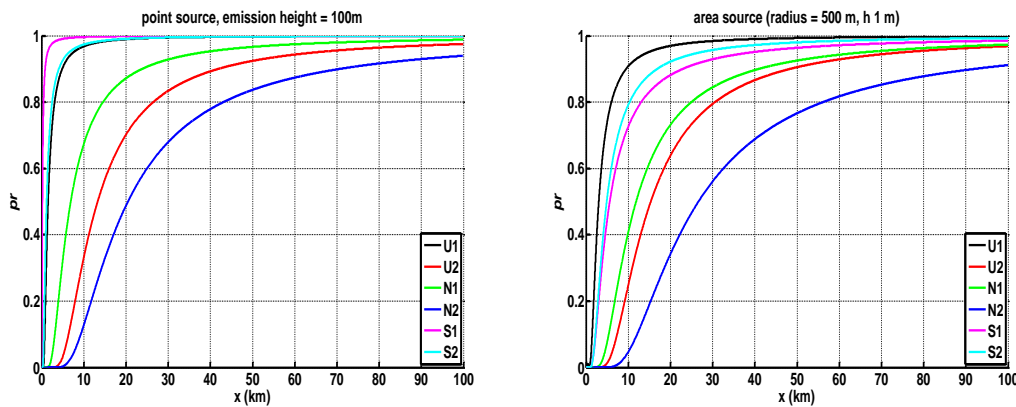

Figure 6.4:   Distributing factor pr (according to Eq. 6.12) between below-cloud and in-cloud scavenging as function of source-receptor distance x for different meteo classes U: unstable, N: neutral, S: stable. σ_z computed as a x^b, (see eq. 3.18), mixing height as in Table 2.5. pr = 0 → below cloud scavenging, pr = 1 → in-cloud scavenging. Left panel: point source with emission height 100 m, right panel: area source with emission height of 1 m. Note that in the case of a point source in meteo class S1, the emission is above the mixing height.

6.5   Scavenging of reversibly soluble gases

When concentrations in air and droplets are in (near) equilibrium during the scavenging process due to limited solubility and/or slow reactions in the drop, a correction for the concentration in air at the ground is used for the scavenging rate of reversibly (superscript r) soluble substances $\Lambda_{w,eff}^{r}$ [h^{-1}]:

$$\Lambda_{w,eff}^{r} = \Lambda_{w,eff}^{i}\ \frac{C(z=0)}{\overline{C(z)}}, \qquad\qquad (6.15)$$

where $\overline{C(z)}$ is the average mixed-layer concentration. This solution ignores any vertical redistribution of plumes as is the case when the equilibrium is not instantaneous. An example of a reversibly soluble gas is SO_2. This gas is slowly converted to bisulphite (HSO_3^{-}) in falling raindrops and the SO_2 concentration in the drops is in (near) equilibrium with the surrounding air (Barrie, 1978). The approach followed here implies that as long as elevated SO_2 plumes do not touch the ground close to the source, they have no impact on wet deposition. This is confirmed by washout experiments (Ten Brink et al., 1988). NH_3 is treated as an irreversibly soluble gas, because NH_3 inside the droplets is assumed to be quickly converted to NH_4^{+}.

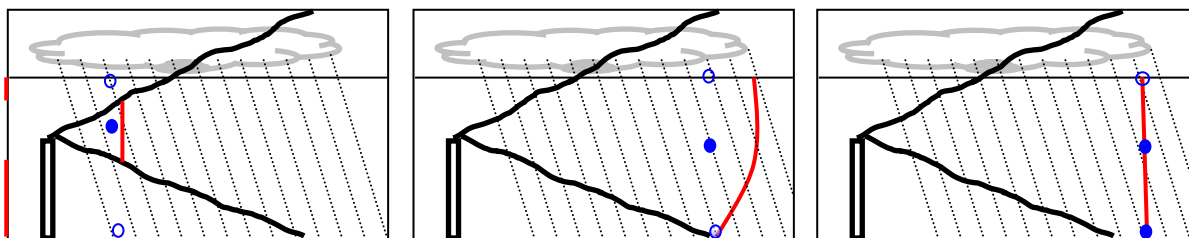For three examples of this equilibrium process, see Figure 6.5.

Figure 6.5: Wet deposition process for reversibly soluble gases; cloud base at the mixing height. In black the stack and plume, in red the vertical concentration profile, the blue dots are droplets. In the left panel, the plume has not yet reached the ground and pollutant caught inside the droplet evaporates below the plume: ratio $C(z=0)/\overline{C(z)} = 0$ → no net wet deposition. In the middle panel, the droplet gets saturated with pollutant in the upper part of the plume; in the lower part, due to a lower concentration outside of the droplet, the pollutant in the droplet evaporates and the net wet deposition decreases by the ratio $C(z=0)/\overline{C(z)}$. In the right panel, we have a well mixed plume ($C(z=0)/\overline{C(z)}=1$) and now the concentration remains the same in the lower part of the plume.

6.6   Overview of wet scavenging parameters

Table 6.1 Wet scavenging parameters for acidifying components as applied in OPS

Component	below-cloud scavenging	in-cloud scavenging
		scavenging ratio W (Eq. 6.1)
Primary:		
SO_2	yes, reversible (Eq. 6.5, 6.15)	$5 \cdot 10^4 \cdot [NH_3]/[SO_2]$
NO_x	no	$2 \cdot 10^4 \cdot [NO_2]/[NO_x]$
NO	no	0
NO_2	no	0
HNO_2	no	$3.3 \cdot 10^5$
PAN	no	0
NH_3	yes, irreversible (Eq. 6.5) $D_g = 0.24$ cm^2 s^{-1}	$1.4 \cdot 10^6$
Secondary:		
SO_4^{2-} aerosol	yes, Eq. 6.7, $\varepsilon = 0.31$	$2.0 \cdot 10^6$
NH_4^+ aerosol	yes, Eq. 6.7, $\varepsilon = 0.31$	$1.4 \cdot 10^7$
NO_3^{total}	yes, Eq. 6.7, $\varepsilon = 0.31$	$1.4 \cdot 10^7$
NO_3^- aerosol	yes, Eq. 6.7, $\varepsilon = 0.31$	$1.4 \cdot 10^7$
HNO_3	no	$1.4 \cdot 10^7$

[#] $[SO_2]$ and $[NH_3]$ are average background concentrations (ppb) in the area between source and receptor.

Table 6.2   Wet deposition parameters for 6 particle classes, as used in OPS.

particle size classes		1	2	3	4	5	6
size range	µm	<0.95	0.95-2.5	2.5-4	4-10	10-20	>20
mass median diameter	µm	0.2	1.6	3	6	14	40
standard distribution fine	%	70	12	8	5.5	2.5	2
standard distribution medium	%	53	16	12	11.5	4.2	3.3
standard distribution coarse	%	42	19	14	14.5	5.9	4.6
in-cloud scavenging ratio	(-)	$2.4\ 10^5$	$1\ 10^6$	$1\ 10^6$	$5\ 10^6$	$9\ 10^6$	$9\ 10^6$
collision efficiency ε (Figure 6.1, Slinn, 1982)	(-)	$1.2\ 10^{-4}$	$3\ 10^{-4}$	$5\ 10^{-4}$	0.31	0.9	1

It might be clear that any form of reactive scavenging in this model is based on empirical parameters. Extrapolating to situations very different from those where parameters were derived can lead to significant errors in the computed wet deposition.

6.7   References

Barrie L.A. (1978) An improved model of reversible SO_2-washout by rain. *Atmospheric Environment* **12**, 407-412.

Barrie L.A. (1981) The prediction of rain acidity and SO_2 scavenging in eastern North America. *Atmospheric Environment* **15**, 31-41.

Barrie L.A. (1992) Scavenging ratios: black magic or a useful scientific tool? In: Schwartz S.E. and Slinn W.G.N, editors. *Precipitation scavenging and atmosphere-surface exchange*, Volume 1. Hemisphere Publ. Corp., Washington. p. 403-419.

Best A.C. (1950) The size distribution of raindrops. *Quart. J.R. meteor. Soc.* **76**, 16-36.

Chan W.H. and Chung D.H.S. (1986) Regional-scale precipitation scavenging of SO_2, SO_4, NO_3, and NHO_3. *Atmospheric Environment* **20,** 1397-1402.

Durham J.L., Overton J.H.,and Aneja V.P. (1981) Influence of gaseous nitric acid on sulfate production and acidity in rain. *Atmospheric Environment* **15**, 1059-1068.

Hales J.M. (1978) Wet removal of sulfur compounds from the atmosphere. *Atmospheric Environment* **12**, 389-399.

Hamrud M., Rodhe H. and Grandell J. (1981) A numerical comparison between Lagrangian and Eulerian rainfall statistics. *Tellus* **33**, 235-241.

Haul P.R. (1978) Preliminary estimates of the washout coefficient for sulphur dioxide using data from an East Midlands ground level monitoring network: Short communication. *Atmospheric Environment* **12**, 2515-2517.

Janssen A.J. and Brink H.M. ten (1985) De samenstelling van neerslag onder een rookgaspluim: modellering, berekening en validatie. Netherlands Energy Research Foundation, Petten, the Netherlands. Report ECN-170.

Levine S.Z. and Schwartz S.E. (1982) In-cloud and below-cloud scavenging of nitric acid vapor. *Atmospheric Environment* **16**, 1725-1734

Marshall J.S. and Palmer M.W.M. (1948) The distribution of raindrops with size. *J. Meteorol.* **5**, 165-166.

Misra P.K., Chan W.H., Chung D. and Tang A.J.S. (1985) Scavenging ratios of acidic pollutants and their use in long-range transport models. *Atmospheric Environment* **19**, 1471-1475.

Rodhe H. and Grandell J. (1972) On the removal time of aerosol particles from the atmosphere by precipitation scavenging. *Tellus* **XXIV**, 442-454.

Scire J.S. and Venkatram A. (1985) The contribution of in-cloud oxidation of SO_2 to wet scavenging of sulfur in convective clouds. *Atmospheric Environment* **19**, 637-650.

Seinfeld J.H. (1986) *Atmospheric chemistry and physics of air pollution.* John Wiley & Sons, New York.

Slinn W.G.N (1982) Predictions for particle deposition to vegetative canopies. *Atmospheric Environment* **16**, 1785-1794.

Ten Brink H.M., Janssen A.J. and Slanina J. (1988) Plume wash-out near a coal-fired power plant: measurements and model calculations. *Atmospheric Environment* **22**, 177-187.

Van der Swaluw, Eric, Asman, Willem A.H., van Jaarsveld, Hans, Hoogerbrugge, Ronald (2011). Wet deposition of ammonium, nitrate and sulfate in the Netherlands over the period 1992–2008, Atmospheric Environment, Volume 45, Issue 23, July 2011, Pages 3819-3826, 10.1016/j.atmosenv.2011.04.017.

Van Egmond N.D., Jaarsveld J.A. van and Onderdelinden D. (1986) The Dutch aerosol study: general overview and preliminary results. In:Lee S.D, Schneider T., Grant, L.D. and Verkerk P.J., editors. In: *Aerosols: Research, Risk Assessment and Control Strategies*. Lewis Publ., Chelsea, USA. p. 269-282.

Van Jaarsveld and Onderdelinden (1986): Modelmatige beschrijving van concentratie en depositie van kolen relevante componenten in NL veroorzaakt door emissies in Europa, PEO report NOK-LUK 3, RIVM report 2282 02 002, Bilthoven, the Netherlands.

Van Jaarsveld J. A. (1995) Modelling the long-term atmospheric behaviour of pollutants on various spatial scales. Ph.D. Thesis, Utrecht University, the Netherlands

Van Jaarsveld, J.A., Bleeker, A. and Hoogervorst, N.J.P. (2000) Evaluatie ammoniakredukties met behulp van metingen en modelberekeningen. RIVM rapport 722108025, RIVM, Bilthoven.

Van Jaarsveld J.A. (2004) Description and validation of OPS-Pro 4.1, RIVM report 500045001/2004.

7.   Chemical transformation

In the OPS model, the chemical transformation process is modelled as a reaction which transforms a primary emitted species into one or more secondary species, which are transported in the same plume. No special local (near the emission source) dispersion and deposition effects are taken into account for reaction products, because these products will be formed gradually after the primary pollutant is emitted into the atmosphere. Conversion rates can be parameterised as functions of parameters such as global radiation, temperature, time of day or others included in the climatological data set created by the pre-processor.

The set-up of the present model permits only a description of a reaction rate by a pseudo first-order reaction rate constant k_c. The differential equation for the pollutant concentration C is then given by:

$$\frac{\partial C}{\partial t} = k_c C. \tag{7.1}$$

k_c is not necessarily a constant, but can be taken as a function of time of day, radiation, temperature etc. A value for k_c can be provided by chemically more detailed models or can be parameterized as a function of background concentration maps.

7.1   Non-acidifying substances

The chemical conversion rate k_c for gaseous substances can be given as a constant and/or as a variable related to the solar radiation measured in a certain period. This conversion rate can be specified using two parameters:

a - a constant conversion rate [% h^{-1}]
b - a variable conversion rate, dependent on the solar radiation [% h^{-1} W^{-1} m^2].

b varies from one stability/mixing height class to the other. The model calculates the conversion rate k_c [% h^{-1}] for a given class according to:

$$k_c = a + b\,Q_r, \tag{7.2}$$

where Q_r is the global solar radiation [W m^{-2}], which has been incorporated in the meteo-statistics as a function of the meteorological class. Long-term average values of Q_r in the Netherlands are given in Table 7.1.

Table 7.1   Average global radiation [W m^{-2}] per (local) stability class

	U1	U2	N1	N2	S1	S2
Global radiation Q_r [W m^{-2}]	206	378	20	22	2	3

When running the model for multiple sources, the effective value of the conversion rate cannot be precisely determined beforehand as solar radiation and its variation over the day depend on the stability/mixing height class. The model calculates this effective value from a mass-weighted averaging of the conversion rates of the separate classes and emission sources, and is as such included in the model output.

In contrast with the acidifying compounds, the conversion process is envisaged here exclusively as a removal term. Dispersion and deposition of the reaction product(s) are not included.

7.2   Acidifying and eutrophying species

7.2.1 Introduction

As already described in the introductory section, the acidifying and eutrophying components include:

sulphur compounds (SO_x)	sulphur dioxide (SO_2)
	sulphate (SO_4^{2-})
oxidised nitrogen compounds (NO_y)	nitrogen oxides (NO and NO_2)
	peroxyacetyl nitrate (PAN)
	nitrous acid (HNO_2)
	nitric acid (HNO_3)
	nitrate (NO_3^-)
reduced nitrogen compounds (NH_y)	ammonia (NH_3)
	ammonium (NH_4^+)

The gaseous SO_2, NO_x (emitted largely in the form of NO, a small fraction is emitted as NO_2) and NH_3 are primary emitted pollutants, while the gaseous NO_2, PAN, HNO_2 and HNO_3 and the non-gaseous SO_4^{2-}, NO_3^- and NH_4^+ are formed from the primary pollutants in the atmosphere under influence of, for example, ozone (O_3) or free OH-radicals. In OPS, the primary oxidised nitrogen pollutant is defined as the sum of NO and NO_2, further denoted as NO_x. The secondary products SO_4^{2-}, NO_3^- and NH_4^+ form mainly ammonia salts having low vapour pressures and consequently appearing as aerosols in the atmosphere (Stelson and Seinfeld, 1982a). The life cycles of the sulphur, nitrogen oxide and ammonium compounds taken into account in the model are given in Figure 7.1.

OPS computes the transport, dispersion and removal of one primary species (SO_2, NO_x or NH_3) and its associated reaction product (SO_4^{2-}, NO_3^{total} or NH_4^+) as schematically depicted in Figure 7.1. In the model output, NO_3^{total} is split into HNO_3, NO_3^{coarse} (in PM_{10} - $PM_{2.5}$) and NO_3^{fine} (in $PM_{2.5}$).
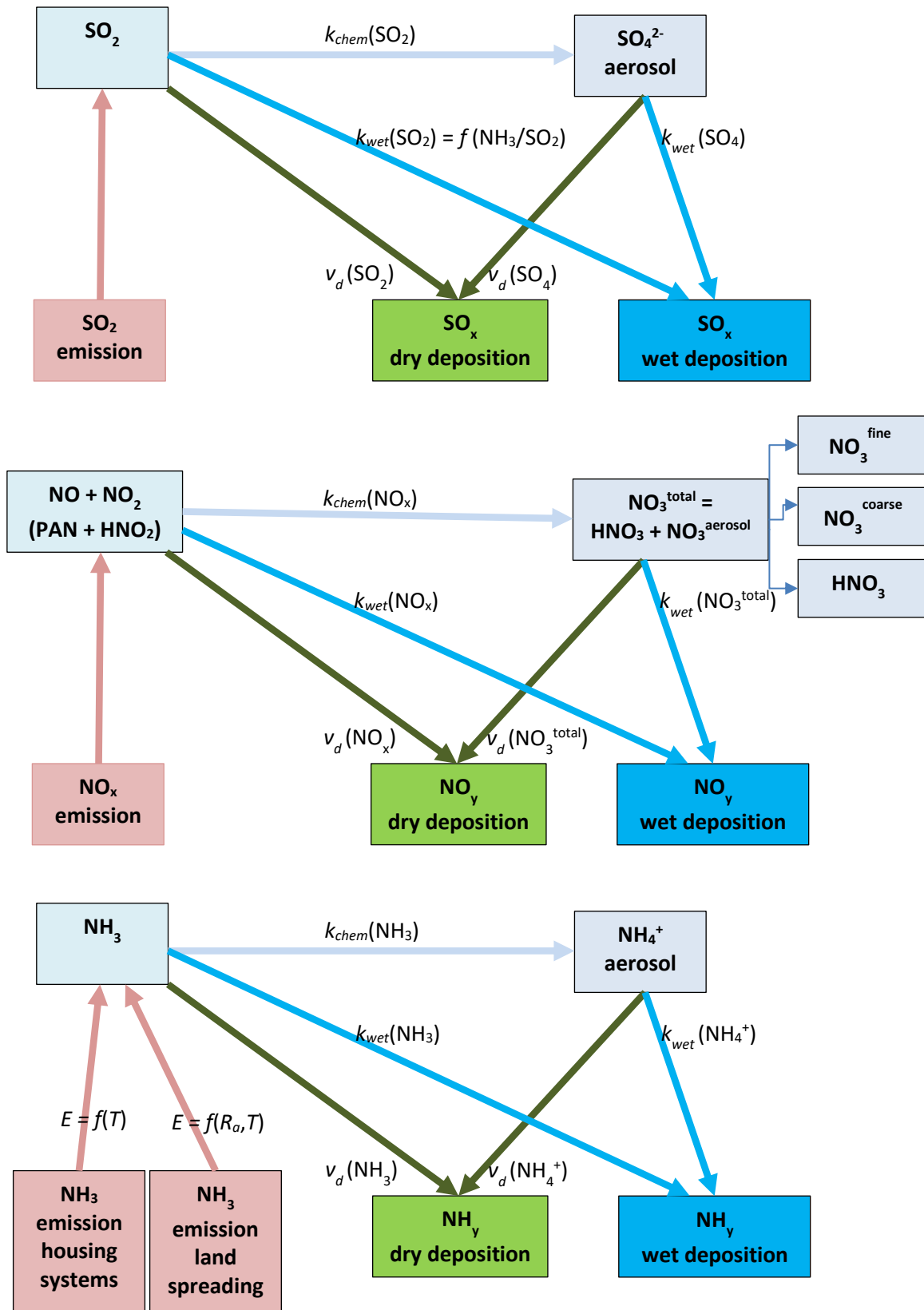
Figure 7.1: Emission, conversion and deposition paths of the OPS model for acidifying compounds. E = emission, T = temperature, R_a = aerodynamic resistance. k_{chem} = chemical conversion rate (1/s), k_{wet} = wet deposition rate (1/s), v_d = dry deposition velocity (m/s). v_d (NO_x) and $v_d(NO_3^{total})$ are weighed averages of v_d of NO, NO_2 , HNO_2 and HNO_3, $NO_3^{aerosol}$ respectively.

7.2.2   EMEP chemical conversion rates

Because of its use of analytical solutions for plumes, OPS is not well suited for implementing a full chemistry scheme with scores of chemical species and hundreds of reactions. OPS-versions prior to v5 used chemical conversion rates k_{chem} (%/hour) based on parameterisations that include background concentration maps. From version 5, OPS also has the option to use chemical conversion rates derived from the EMEP model (Simpson et al. 2012) in the configuration for The Netherlands (EMEP4NL, van der Swaluw, 2020). If files with EMEP conversion rate maps are not available for a specific year, the old OPS chemical conversion rates are used; these are described in the documentation of OPS 4.5.2. This documentation describes the EMEP conversion rates and how OPS uses them.

In order to be able to use the chemical conversion rates from EMEP in OPS, a special routine was added in EMEP, where for each grid cell and for each time step Δt, the mass of the precursors SO_2, NO_x and NH_3 at the start of the time step and the mass chemically converted into a secondary species during that time step is averaged into a grid of yearly averaged values. Here NO_3^{total} is HNO_3 + $NO_3^{aerosol}$ and mass is integrated over the mixing layer. These maps of M_{prec} = precursor-mass [$\mu g/m^2$] and ΔM_{conv} = converted-mass [$\mu g/m^2$] are read into OPS, then averaged over a trajectory and finally the conversion rate k_{chem} in %/hour can be computed as $k_{chem} = \frac{100}{\Delta t} \frac{\Delta M_{conv}}{M_{prec}}$. Note that for the convenience of the OPS calculations, the second type of map does not contain ΔM_{conv}, but $\frac{100}{\Delta t} \Delta M_{conv}$ [$\mu g/m^2$ (%/h)].

The chemical scheme used in EMEP computes the removal of the precursors SO_2, NO_x, NH_3 and the transformation into secondary inorganic aerosols sulphate, nitrate and ammonium. The sections below describe in short the chemistry involved, but for more details one is referred to the description in Simpson et al. 2012. Also presented are maps of chemical conversion rates for 2019 and 2030. For projections into the future, EMEP produced conversion rates for 2030, with projected 2030 emissions and an 'average' meteo year, for which 2009 has been selected as a more or less 'average meteo year'. We used the configuration for EMEP4NL with a nested grid around the Netherlands; the finest grid resolution is 1.3 x 2.1 km² (longitude-latitude grid).

7.2.3   Sulphur compounds

Sulphate formation in EMEP
The atmospheric oxidation of SO_2 can take place in the **gas phase** via the reaction with OH radicals forming sulphuric acid (H_2SO_4), which is then typically scavenged into aqueous droplets or aerosol particles.

$$SO_2 + OH \rightarrow ......H_2SO_4\ (+HO_2) \tag{7.3}$$

More importantly, sulphate is formed in the **liquid phase** once SO_2 is scavenged into solution. In the liquid phase, sulphur is oxidized by oxygen (catalysed by transition metals), ozone or hydrogen peroxide. Liquid phase oxidation reactions are orders of magnitude faster. Note that, in contrast to gaseous HNO_3, H_2SO_4 is considered to be part of the aerosol in the form of liquid aerosol droplets.

Most of the H_2SO_4 will react with NH_3 to yield an NH_4^+ containing aerosol. This is a one-way reaction and the aerosol will not evaporate again:

$$2\ NH_3 + H_2SO_4 \rightarrow (NH_4)_2\ SO_4 \tag{7.4}$$

and

$$NH_3 + H_2SO_4 \rightarrow (NH_4)HSO_4 \tag{7.5}$$

These reactions form the link between sulphur and ammonia in the atmosphere. EMEP uses the MARS equilibrium module of Binkowski and Shankar (1995) to calculate the partitioning between gas and aerosol phase in the system of SO_4^{2-} - HNO_3 - NO_3^- - NH_3 - NH_4^+.
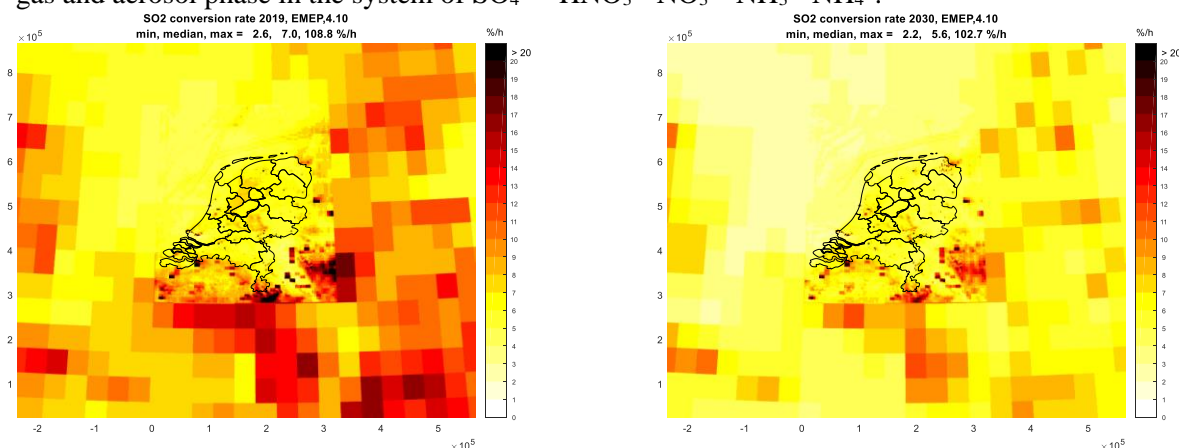

Figure 7.2. Chemical conversion rates for $SO_2 \rightarrow SO_4^{2-}$ (range [0 20] %/h) from EMEP for 2019 (left panel) and 2030 (right panel).Conversion rates for 2030 are computed with projected emissions and an 'average meteo year'. It is possible that the conversion rate is larger than 100 %/hour, for instance a conversion rate of 200 %/hour should be interpreted as 100% per ½ hour.

7.2.4   Nitrogen oxides

NO, NO$_2$, PAN, HNO$_2$

Modelling concentrations of NO_2 using the photo-stationary equilibrium reaction requires estimates of O_3 (background) concentrations on a local scale. Such O_3 concentrations are strongly influenced by neighbouring NO sources, making this approach unsuited for this model. Basically, the OPS model computes contributions of sources independent of each other, so empirical relations between NO and NO_2 concentrations cannot be used unless the 'background' NO_2 concentration is taken into account. An alternative would be an iterative approach, i.e. first calculating total concentrations linearly and then the non-linear relations using the results of the first step as the background levels. The computed NO_2, PAN and HNO_2 concentrations would not be very accurate anyway. These considerations have led to the choice of modelling the sum of NO, NO_2, PAN and HNO_2 as a single conservative species NO_x.

Measurements in Delft carried out by TNO indicate a PAN concentration which, on average, is only in the order of 5% of the NO_2 concentration (Ogilvie, 1982). The deposition properties are also uncertain but probably not very different from those of NO_2; it was therefore decided not to take PAN into account as a separate component for this model but to consider it as a part of NO_x.

Slanina *et al*. (1990) report average nitrous acid (HNO_2) concentrations of 0.64 ppb for a forest site in the Netherlands (Speulderbos), which is in the order of 4 % of $NO+NO_2$ concentrations. Similar results are reported by Kitto and Harrison (1992).

In OPS, modelled 'NO_x' consist of $NO + NO_2 + HNO_2 + PAN$, including a 4% contribution of HNO_2 and a possible PAN contribution of 5% to the NO_2 concentration. However, measurements of NO_x usually consist only of $NO + NO_2$. At an average NO_2/NO_x ratio of 0.65, the modelled NO_x ($NO + NO_2 + HNO_2 + PAN$) concentration may be systematically 8% higher than measured NO_x ($NO + NO_2$) concentrations. In order to keep the model output consistent to reported concentrations, an 8% reduction is applied to the model output of NO_x concentrations, such that the *model output* of NO_x represents the sum of NO and NO_2 .
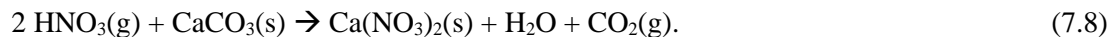
Nitrate formation in EMEP

An important source of aerosol nitrate in the troposphere is the following reaction of N_2O_5:

$$N_2O_5 + H_2O \rightarrow 2HNO_3. \tag{7.6}$$

HNO$_3$ formed in the reaction above is initially assumed to evaporate and will take part in the formation of ammonium nitrate or coarse nitrate. Coarse nitrate is formed from reactions with sea salt and dust particles with HNO$_3$ (aq = aqueous phase, g = gas, s = surface):

$$HNO_3(aq) + NaCl(aq, s) \rightarrow NaNO_3(aq, s) + HCl(g). \tag{7.7}$$

HNO$_3$ can also react with aqueous carbonates such as dissolved CaCO$_3$ and MgCO$_3$ on soil particles to form coarse mode nitrate:

$$2\ HNO_3(g) + CaCO_3(s) \rightarrow Ca(NO_3)_2(s) + H_2O + CO_2(g). \tag{7.8}$$

The MARS module in EMEP takes care of the partitioning between nitric acid (HNO$_3$) and (fine) nitrate in the form of ammonium nitrate:

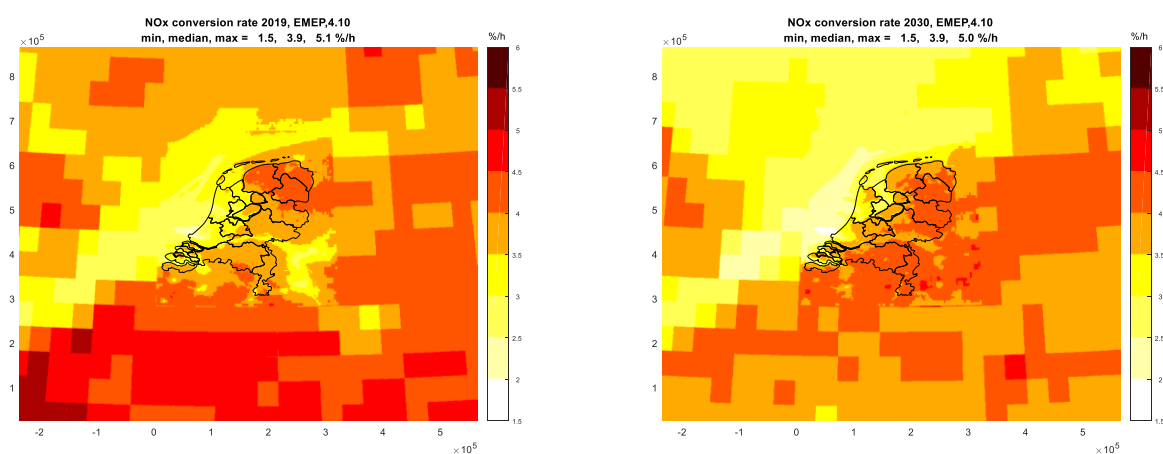$$NH_3 + HNO_3 \leftrightarrow NH_4NO_3 . \tag{7.9}$$

Figure 7.3. Chemical conversion rates for $NO_x \rightarrow NO_3^{total} = HNO_3 + NO_3^{coarse} + NO_3^{fine}$ (range [1.5 6] %/h) from EMEP for 2019 (left panel) and 2030 (right panel). Conversion rates for 2030 are computed with projected emissions and an 'average meteo year'.

NO$_2$/NO$_x$ ratio, background

Because the NO$_x$ species have rather different dry and wet deposition properties, the deposition properties of NO$_x$ are computed as a weighed average using NO$_2$/NO$_x$ ratios and a (fixed) HNO$_2$/NO$_x$ ratio. These NO$_2$/NO$_x$ ratios are derived from observations as a function of atmospheric stability and trajectory length according to the classification of meteorological situations used in the model.

The spatially variable NO$_2$/NO$_x$ ratio is defined in terms of a stability dependent factor and a spatially variable one:

$$r_{n,eff}(x,s) = \bar{r}_n(x,s)\, f_{n\_space}. \tag{7.10}$$

Table 7.2 presents the data for $\bar{r}_n(x,s)$ and $f_n(x,s)$ for the different classes for both summer and winter seasons on the basis of five years of measurements.

Table 7.2   *Statistical data on night time NO$_2$/NO$_x$ ratios and relative occurrences of night time hours for the meteorological classes used in the OPS model. The data are derived from LML observations at rural stations over the 1980-1985 period.*

	Period	Trajectory length (km)	Meteorological classes					
			U1	U2	N1	N2	S1	S2
NO$_2$/NO$_x$ ratio: $\bar{r}_n(x,s)$	Summer	10	0.78	0.78	0.78	0.78	0.78	0.78
		100	0.78	0.78	0.78	0.78	0.78	0.78
		300	0.78	0.78	0.78	0.78	0.78	0.78
		1000	0.78	0.78	0.78	0.78	0.78	0.78
	Winter	10	0.47	0.47	0.62	0.69	0.39	0.58
		100	0.47	0.47	0.62	0.69	0.39	0.58
		300	0.47	0.47	0.62	0.69	0.39	0.58
		1000	0.47	0.47	0.62	0.69	0.39	0.58
Relative frequency of nighttime hours: $f_n(x,s)$	Summer	10	0	0	0.61	0.61	1.00	0.98
		100	0.17	0.17	0.68	0.68	0.63	0.83
		300	0.43	0.43	0.44	0.44	0.42	0.44
		1000	0.43	0.43	0.44	0.44	0.42	0.44
	Winter	10	0	0	0.66	0.66	1.00	0.99
		100	0.25	0.25	0.71	0.71	0.77	0.92
		300	0.62	0.64	0.74	0.63	0.64	0.63
		1000	0.62	0.74	0.74	0.63	0.64	0.63

It can be concluded from Table 7.2 that it is more important to include seasonal variations in the parameterisations than variations in stability and/or mixing height.

The parameter $\bar{r}_n$ provides diurnal and seasonal variations in NO$_2$/NO$_x$ ratios to some extent. In the OPS model, also a spatial variation is introduced. This spatial variation is derived from a map of annual mean (background) NO$_2$ concentrations in combination with an empirical relation between NO$_2$ and NO$_x$ concentrations (see Eq. 7.17). The spatial variation factor, f_{n_space}, is computed as:

$$f_{n\_space} = \frac{[NO_2]_{bg}}{0.65[NO_x]_{bg}} = \frac{[NO_2]_{bg}}{0.65\exp\left(\frac{[NO_2]_{bg}+12.4}{8.6}\right)},$$ (7.11)

with [NO$_2$]$_{bg}$ in ppb. The value 0.65 represents the average NO$_2$/NO$_x$ ratio for the Netherlands, so f_{n_space} has unity value when averaged over the Netherlands. Equation (7.11) is applicable to annual mean [NO$_2$]$_{bg}$ values greater than 10 ppb, a value exceeded for almost all areas in the Netherlands; f_{n_space} has a range of 0.50 (urban areas) up to 1.2 (coastal area of Friesland).
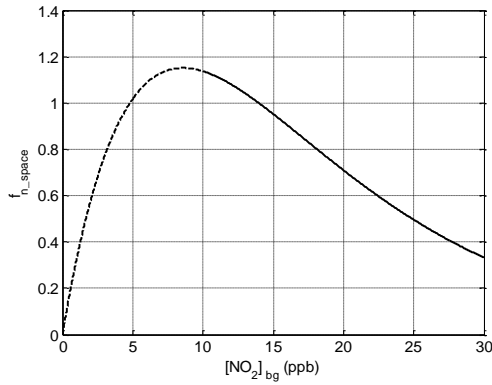
Figure 7.4: f_{n_space} as a function of background NO₂ concentration.

NO₂/NOₓ ratio near roads

During the development of an air quality model for traffic related sources, NO₂ concentrations were fitted against NOₓ concentrations per wind sector; see Van den Hout and Baars (1988), Wesseling and van Velze (2015):

$$\text{NO}_2(i) = f_{\text{NO}_2}\text{NO}_\text{x}(i) + \frac{\text{O}_3(i)\big(1 - f_{\text{NO}_2}\big)\text{NO}_\text{x}(i)}{\big(1 - f_{\text{NO}_2}\big)\text{NO}_\text{x}(i) + K},$$

$\text{NO}_2(i)$: yearly averaged concentration contribution of traffic to NO₂ concentration in wind sector i [μg/m³]

$\text{NO}_\text{x}(i)$: yearly averaged concentration contribution of traffic to NOx concentration in wind sector i [μg/m³]

f_{NO_2} : fraction directly emitted NO₂ [-]

K : empirical parameter = 100 μg/m³

$\text{O}_3(i)$: yearly averaged large scale ozone concentration in wind sector i [μg/m³].

Note that the NO₂/NOₓ ratio will become constant (independent of NOₓ) at larger distance from the road (($1 - f_{\text{NO}_2}$) NOₓ ≪ K):

$$\frac{\text{NO}_2}{\text{NO}_\text{x}} = f_{\text{NO}_2} + \frac{\text{O}_3\,(1 - f_{\text{NO}_2})}{(1 - f_{\text{NO}_2})\text{NO}_\text{x} + K} \rightarrow f_{\text{NO}_2} + \frac{(1 - f_{\text{NO}_2})}{K}\text{O}_3 \text{ , for NO}_\text{x} \rightarrow 0.$$

For example, using a fraction direct NO₂ = 0.15, results in limit values for the NO₂/NOₓ ratio of 0.5325 for O₃ = 45 μg/m³ and 0.915 for O₃ = 90 μg/m³.
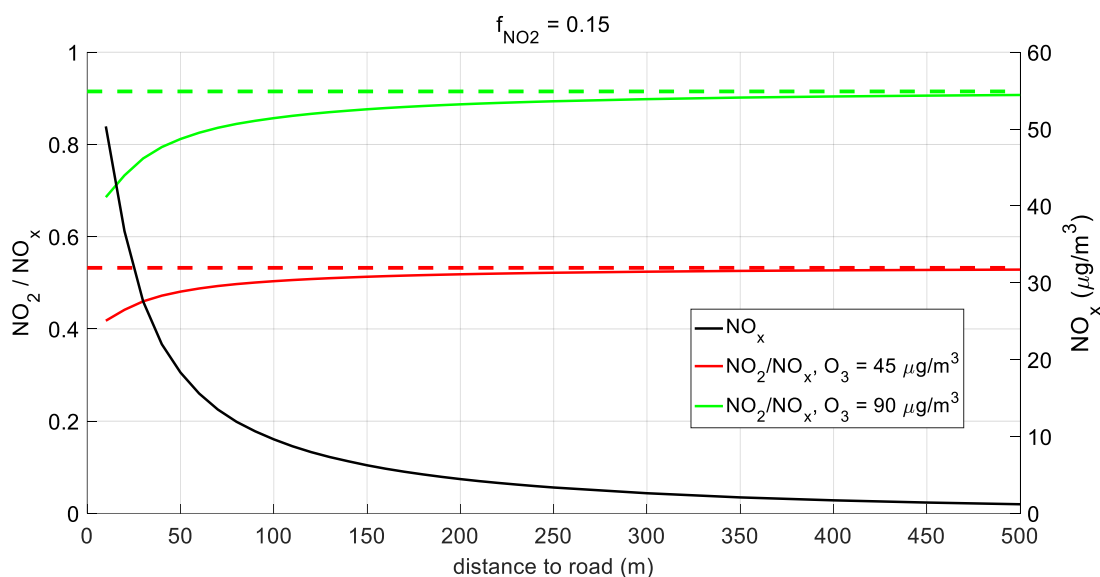
Figure 7.5: NO$_2$/NO$_x$ ratio as function of distance to the road, computed with the van den Hout formula, given a hypothetical NO$_x$ profile (black, right axis). Ozone concentration 45 µg/m^3 (red) or 90 µg/m^3 (green), fraction directly emitted NO$_2$ = 0.15. The dashed lines indicate the limit value for NO$_x$ → 0 µg/m^3.

The NO$_2$ conversion parametrisation by van den Hout should only be used for traffic related sources and for receptors within 5000 m of a source and with a receptor height lower than 5 m. An OPS user can specify for which traffic related economic sectors this parametrisation is used or can choose to use the standard method with background concentrations (more details in the OPS User Manual). Beyond 5000 m, OPS computes the NO$_2$/NO$_x$ ratio based on background concentration, as before. Before applying this formula, NO$_x$ contributions of all traffic related sources must be accumulated. This means that an extra iteration has been built in the OPS model, where NO$_x$ contributions are added per wind sector in the first iteration. There is currently no possibility to also include other sources (e.g. industry) in the NO$_x$ summation and NO$_2$ contributions from these different types of sources are added up linearly; any competition for the available ozone is neglected here. As a result of this approach, NO$_2$ may be slightly overestimated.

The ozone concentration needed in the van den Hout formula is given as a wind rose, in a 1x1 km^2 grid. We retrieved ozone concentrations in 12 wind sectors from PreSRM (https://presrm.nl). Data is supplied as part of the OPS-release. The ozone concentration is corrected for the contribution of major roads (the so-called double-counting correction). Consistent with other background data maps in the OPS model, ozone concentrations are available for actual years and prognostic years (based on multi-annual meteo for 2005-2014).

HNO$_3$/NO$_3^{total}$ ratio for deposition parameters
Because of the very different dry deposition properties of HNO$_3$ and NO$_3^-$, the ratio f_{HNO3} between (gaseous) HNO$_3$ and the total secondary compound, NO$_3^{total}$ (= HNO$_3$ + NO$_3^-$) is used to average dry canopy resistances of HNO$_3$ and NO$_3^-$. This fraction is modelled as a function of the NH$_3$ concentration according to:

$$f_{HNO3} = \frac{[HNO_3]}{([HNO_3]+[NO_3^-])} = 0.024 \left(\frac{[NH_3]_{bg}}{1000} \right)^{-0.44} \tag{7.12}$$

in which [NH$_3$]$_{bg}$ is the local (prescribed) background concentration of NH$_3$ in ppb (see section 7.3 for background concentrations).
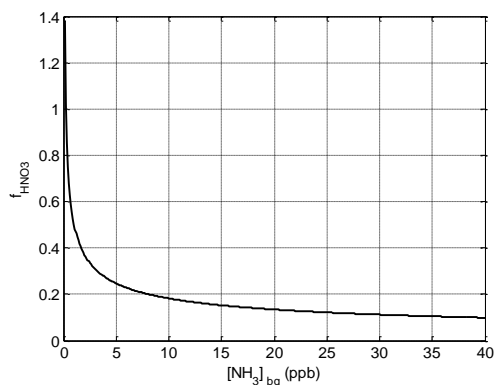
Figure 7.6: f_{HNO3} *as function of NH₃ concentration.*

The formulation of f_{HNO3} is determined by a best fit to NH$_3$ and HNO$_3$ concentration results of a 1D chemistry model applied for the typical Dutch pollution climate for a period of several months. Because of the relatively high NH$_3$ concentrations in the Netherlands, we can expect higher nitrate aerosol concentrations than elsewhere in Europe. This is what actually is seen in the EMEP network (Hjellbrekke, 1999).

HNO$_3$/NO$_3$^{total}, NO$_3$^{coarse}/NO$_3$^{total} , NO$_3$^{fine}/NO$_3$^{total} ratios for concentrations
The secondary species that is transported in OPS is NO$_3$^{total} = HNO$_3$ + NO$_3$^{aerosol}, where NO$_3$^{aerosol} = NO$_3$^{coarse} + NO$_3$^{fine}, with the fine fraction NO$_3$^{fine} inside PM$_{2.5}$ and the coarse fraction NO$_3$^{coarse} in coarse PM (i.e. PM$_{10}$ - PM$_{2.5}$). Maps of yearly averaged fractions HNO$_3$/NO$_3$^{total}, NO$_3$^{coarse}/NO$_3$^{total} and NO$_3$^{fine}/NO$_3$^{total} derived from EMEP are used in OPS to produce output of concentrations of HNO$_3$, NO$_3$^{coarse} and NO$_3$^{fine} separately. In Figure 7.7, we show examples for the years 2019 and 2030.

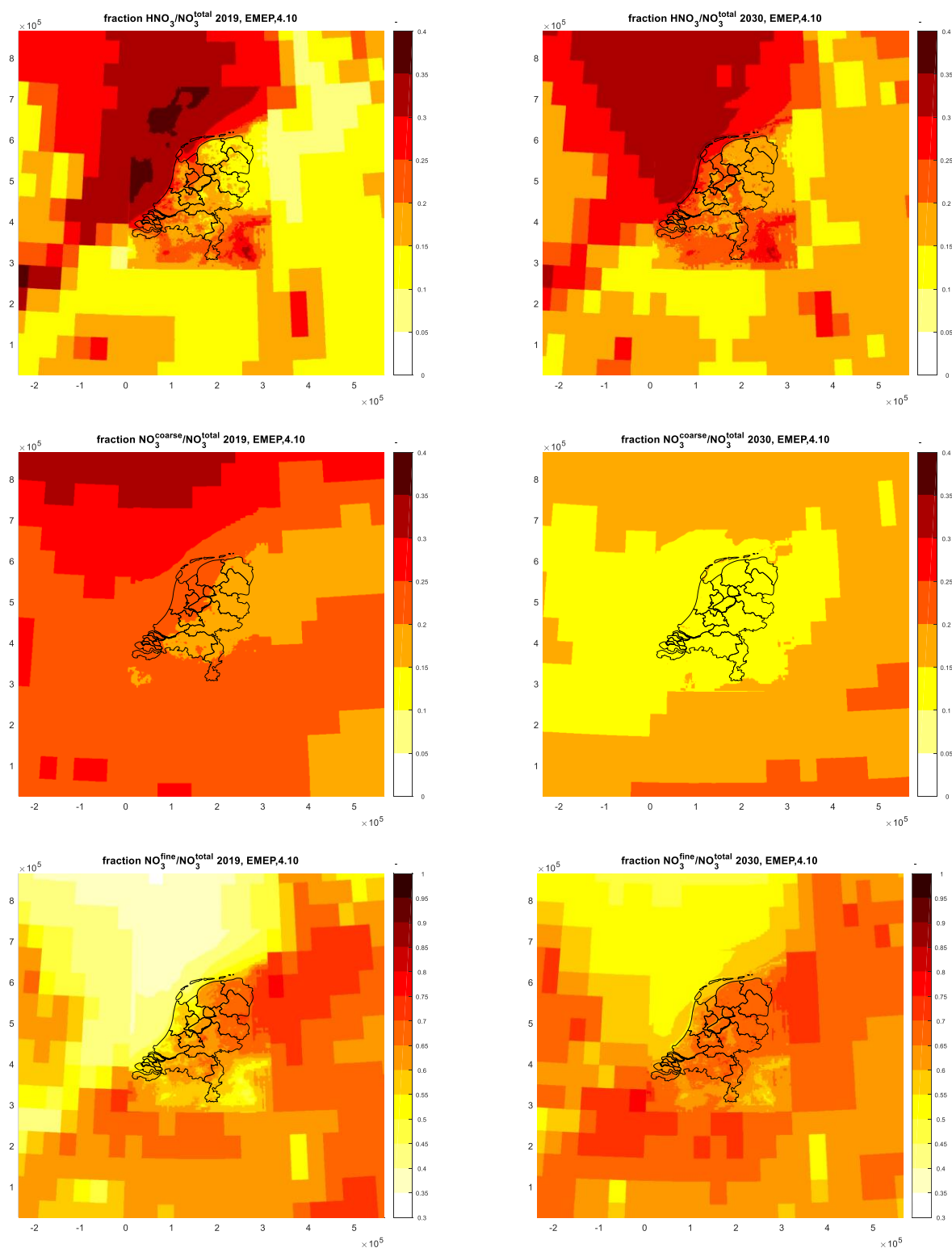*Figure 7.7. Yearly averaged fractions of sub-species of NO_3^{total} from EMEP for 2019 (left panels) and 2030 (right panels). Top row: HNO_3/NO_3^{total};(range [0 0.4]), middle row: $NO_3^{coarse}/NO_3^{total}$ (range [0 0.4]), bottom row: $NO_3^{coarse}/NO_3^{total}$ (range [0.3 1]). 2030 are computed with projected emissions and an 'average meteo year'.*

7.2.5   Ammonia compounds

Ammonium formation in EMEP

Under European conditions, a major part of the gaseous NH_3 will react with H_2SO_4 to yield an NH_4^+-containing aerosol:

$$2\ NH_3 + H_2SO_4 \rightarrow (NH_4)_2\ SO_4 \tag{7.13}$$

and

$$NH_3 + H_2SO_4 \rightarrow (NH_4)HSO_4\ . \tag{7.14}$$

These are one-way reactions and the aerosol will not evaporate again (Asman and Janssen, 1987). A part will react with gaseous HNO_3 through reaction:

$$NH_3 + HNO_3 \leftrightarrow NH_4NO_3 \tag{7.15}$$

 and a similar equilibrium reaction with HCl will form NH_4Cl (Pio and Harrison, 1987):

$$NH_3 + HCl\ \ \leftrightarrow NH_4Cl\ . \tag{7.16}$$

EMEP uses the MARS equilibrium module of Binkowski and Shankar (1995) to compute the partitioning between gas and aerosol phase in the system of SO_4^{2-} - HNO_3 - NO_3^- - NH_3 - NH_4^+. Note that because of the reverse reactions, chemical conversion rates can be negative, meaning a net conversion from NH_4^+ to NH_3.
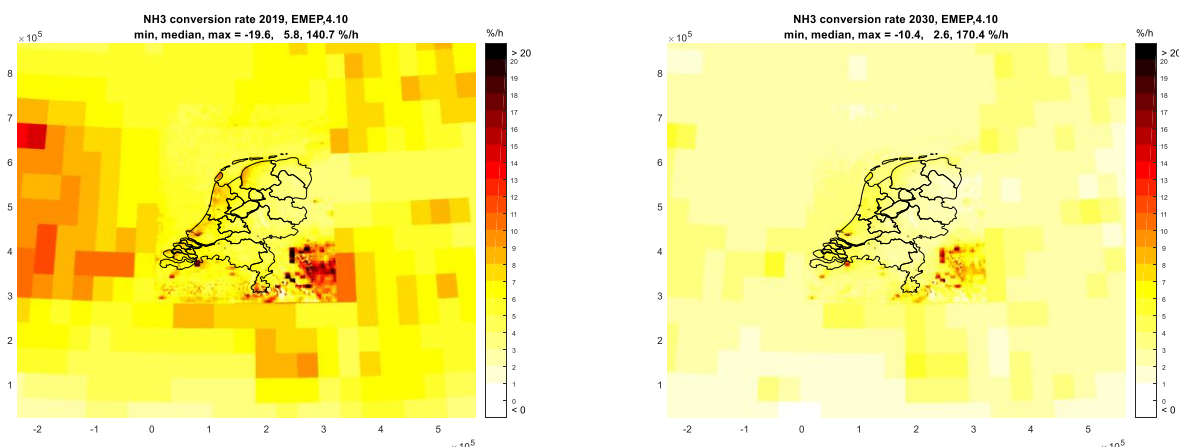

Figure 7.8. Chemical conversion rates for $NH_3 \rightarrow NH_4^+$ (range [0 20] %/h) from EMEP for 2019 (left panel) and 2030 (right panel).Conversion rates for 2030 are computed with projected emissions and an 'average meteo year'. It is possible that the conversion rate is larger than 100 %/hour, for instance a conversion rate of 200 %/hour should be interpreted as 100% per ½ hour. Negative conversion rates may occur for NH_3.

7.3   Prescribed concentration levels (background concentrations)

As mentioned in the introduction of this chapter, the OPS model cannot take changes in atmospheric composition due to chemical reactions or deposition processes *directly* into account: one has to quantify the effect of changing precursor levels on the (bulk) reactions and translate this into conversion maps using EMEP or use simple functions that depend on absolute precursor levels. For the latter, the model needs maps of precursor concentrations with sufficient spatial and temporal detail. One way to derive such simplified functions is to use a (complex) non-linear model to describe time series of concentration levels of the relevant compounds for a longer period and then fit a mathematical function to relevant model outputs.

For the modelling of transport and deposition of acidifying compounds, (existing) levels of SO_2, NO_2 and NH_3 have been found to be of great importance because of the chemical interactions. The most important is probably the role of NH_3 in the reaction of sulphuric acid to ammonia sulphates and nitric acid to ammonia nitrates. As such, the NH_3 is consumed, depending indirectly on levels of SO_2 and NO_2. A similar interrelation exists for the formation of secondary aerosols. If one considers the dramatic decrease of especially SO_2 in the past decades (see Figure 7.11), then it is important to include these background concentrations as input data to the OPS model.

A summary of where background concentrations are used in the model is given in the following table.

Table 7. 7.3: Summary of use of background concentrations in the OPS model

background concentrations	ratio	process
SO_2, NH_3	SO_2/NH_3	$NH_3 \rightarrow NH_4$ conversion, if EMEP data not available [1]
NO_x, NH_3	NO_2/NH_3	$NH_3 \rightarrow NH_4$ conversion, if EMEP data not available
NO_x	NO_2/NO_x	$NO_2 \rightarrow HNO_3$ conversion, if EMEP data not available
SO_2, NH_3	N/S	in-cloud scavenging ratio SO_2
NO_x	NO_2/NO_x	in-cloud scavenging ratio NO_x
NH_3	HNO_3/NO_3-total	canopy resistance $R_c(NO_3^{total})$
NO_x	NO_2/NO_x	canopy resistance $R_c(NO_x)$
NH_3		compensation point NH_3 (used in parametrisation of concentration in vegetation/soil and in air)
SO_2, NH_3	SO_2/NH_3	codeposition NH_3
O_3		NO_2 conversion near roads

[1] Standard runs use chemical conversion rates from EMEP.

Background concentrations of SO_2, NO_x, NH_3 and O_3 are included as gridded maps in the OPS model. These maps encompass a large part of Western Europe and have a spatial resolution of 1 x 1 km for the Netherlands and 5 x 5 km for the foreign countries. To produce these maps, the OPS model is run iteratively. Each iteration OPS computes concentration maps that are then biascorrected using observations and used as background concentration maps for the next iteration. In this way, non-linearities are approximated in a stepwise linear way. For ozone a slightly different approach is used: ozone concentrations in 12 wind sectors are retrieved from PreSRM (https://presrm.nl), which is also based on OPS runs.

Background concentration maps are obtained for each year from 2005 up to the most recent elapsed year, with the following iterative procedure:

1. **Computation at measurement sites**
   Concentrations are computed at the measurement sites of Luchtmeetnet (luchtmeetnet.nl) or MAN (for NH_3; Meetnet Ammoniak in Natuurgebieden) with the detailed emission data used in the production of GCN maps (Mijnen Visser et al., 2024).

2. **Computation of concentration maps**
   Concentration maps computed with the same modelinput.

3. **Bias correction of concentration maps**
   Modelled concentration maps are bias corrected using observations and calculations at the sites of Luchtmeetnet or MAN. The bias correction methods are the same as the methods used in the production of GCN maps (Mijnen-Visser et al., 2024).

4. **Computation at measurement sites and stop criterion**

Concentrations are again computed at the measurement sites of Luchtmeetnet or MAN, but now with the concentration maps of step 3 as background concentration maps. If the concentrations at more than 5% of the measurement sites change by more than 5% the iteration loop continues at step 2.

The background concentration of NO_2 is derived from the background NO_x concentration using a simple empirical relation derived from LML observations. This relation is:

$$[NO_2] = \beta_1 \ln([NO_x]) + \beta_2,$$ (7.17)

with [] concentrations in ppbv and empirical parameters $\beta_1 = 8.6, \beta_2 = -12.4$. This relation has been derived from 1993 LML-measurements. Since this function drops below zero for low values of $[NO_x]$, a linear function is used for $[NO_x] \leq \exp(1 - \frac{\beta_2}{\beta_1})$, that touches the ln-function at $\exp(1 - \frac{\beta_2}{\beta_1})$ and is zero for $[NO_x] = 0$ ppbv.

This conversion function typically explains more than 90% of the variation in yearly averaged measured NO_2 concentrations.
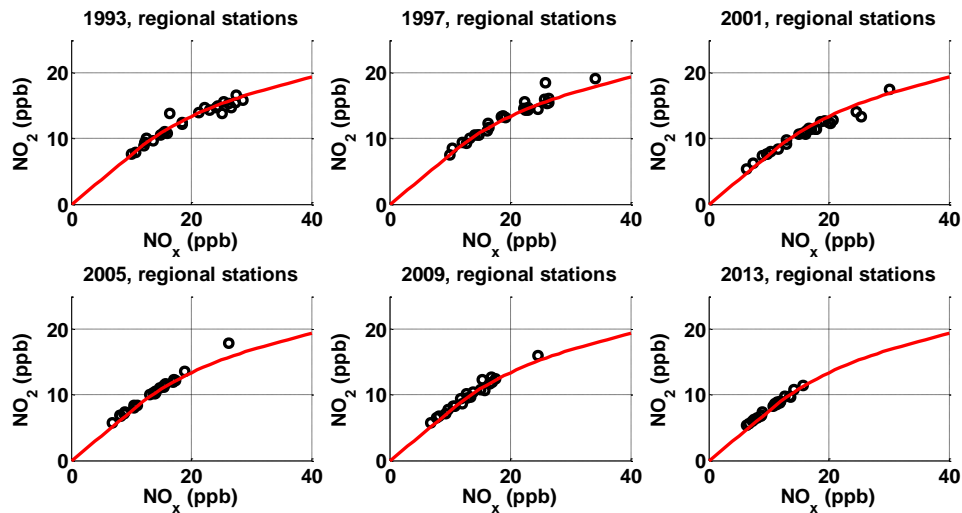

Figure 7.9: Yearly averaged NO_2- vs. NO_x-concentration for regional LML-stations. In red the $NO_x \rightarrow NO_2$-conversion function.

The calibrated maps of the background concentrations of SO_2, NO_x and NH_3 for the year 2005 are given in Figure 7.10.
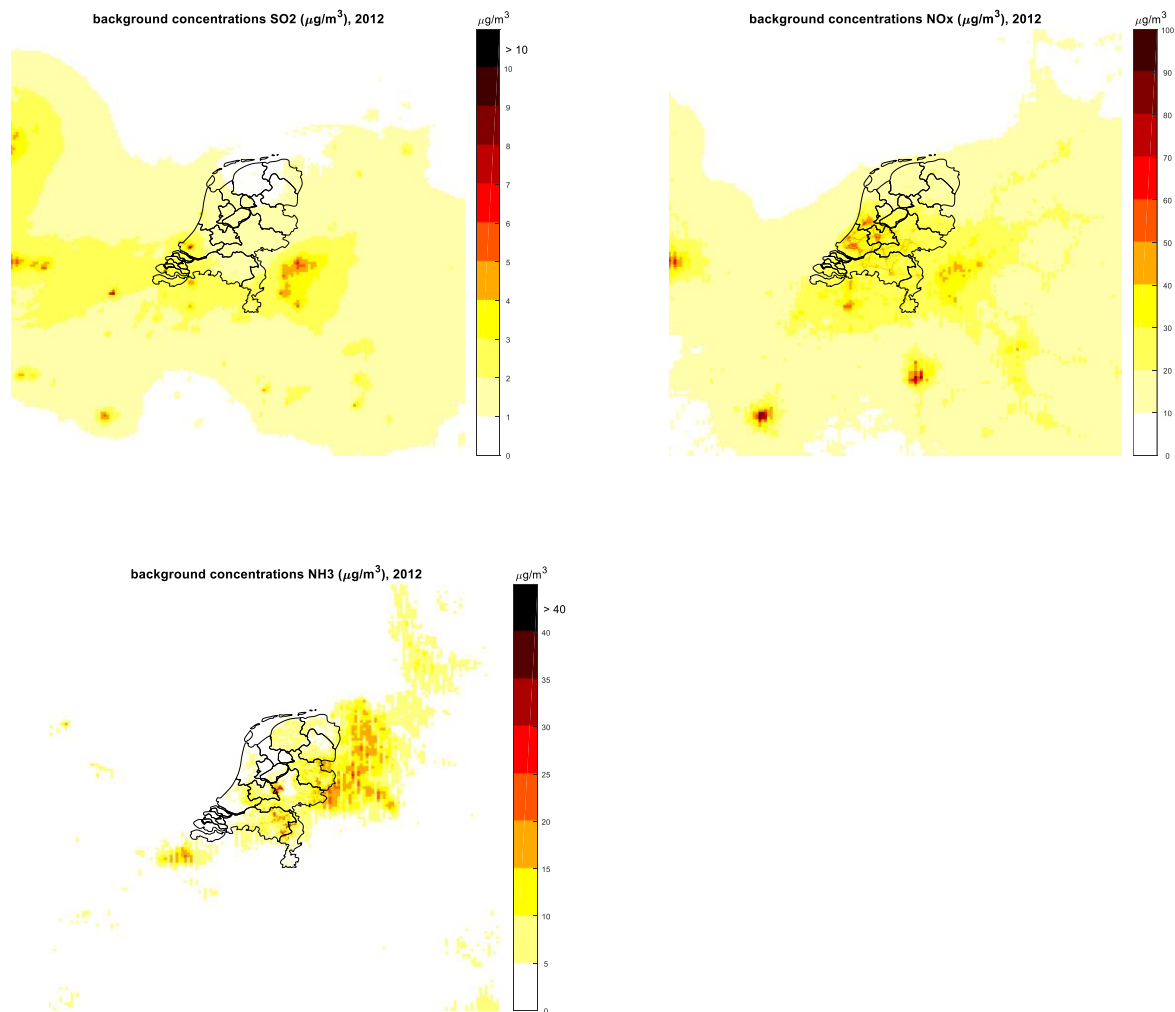
Figure 7.10. *Background concentration maps (μg/m³) for 2012; left upper panel: SO₂ (range [0 10]), right upper: NOₓ (range [0 100]), bottom: NH₃ (range [0 40]).*

The yearly mean concentrations, used in the calculation of the trend factors, are presented in Figure 7.11).
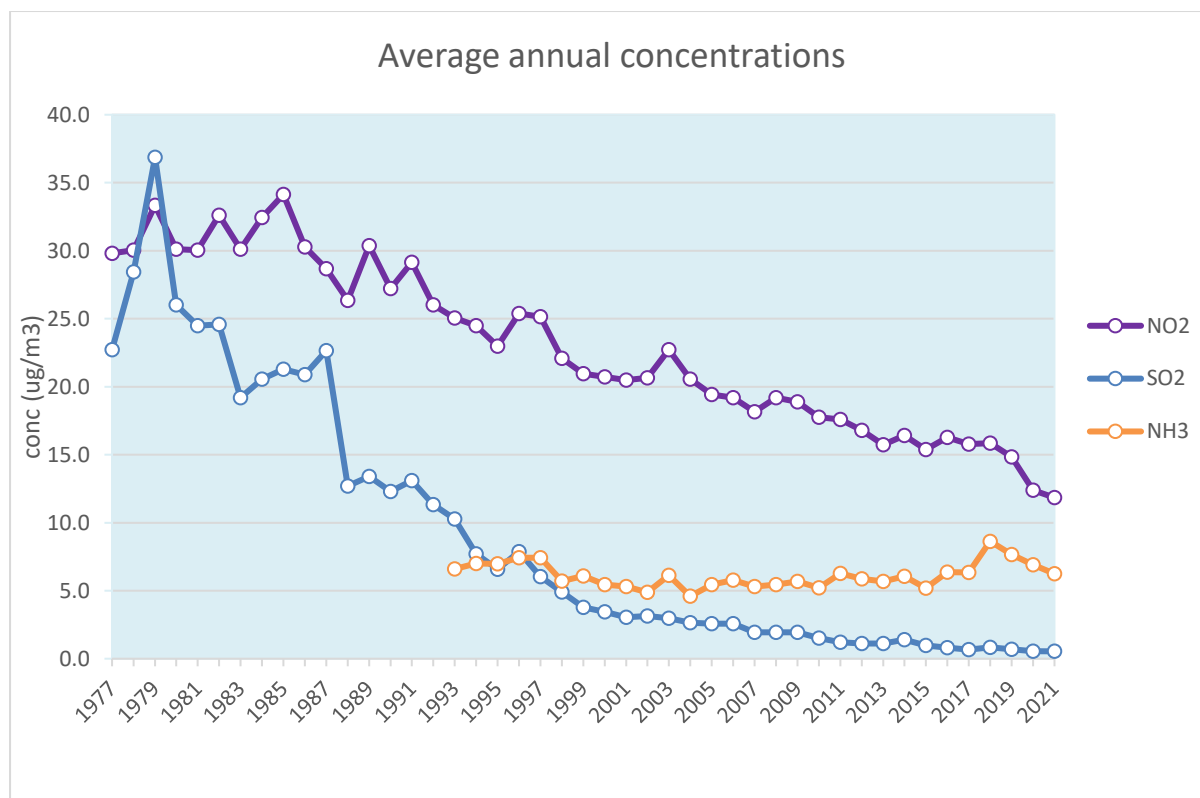
Figure 7.11. Average annual concentrations (µg/m³) of SO₂, NO₂ and NH₃, derived from measurements at the regional stations of the LML network. For NH₃ also stations of the MAN network are used starting in 2005. See table 7.4 for representative periods.

7.4   Secondary species in OPS

The production and deposition of a secondary species cannot be treated as a steady state process and this means that a numerical time stepping procedure along the trajectory is used in order to estimate the cross-wind integrated mass flux (= depleted source strength) $\tilde{Q}_{sec,num}$ [g/s] of a secondary species at the receptor. Because the production of the secondary species obviously depends on the amount of primary species, the time stepping procedure also keeps track of the primary species. The processes in this time stepping procedure are:

- loss of primary species due to dry deposition, wet deposition and chemical conversion; this also gives a primary mass flux $\tilde{Q}_{pri,num}$ at the receptor.
- Production of secondary species due to chemical conversion of the primary species.
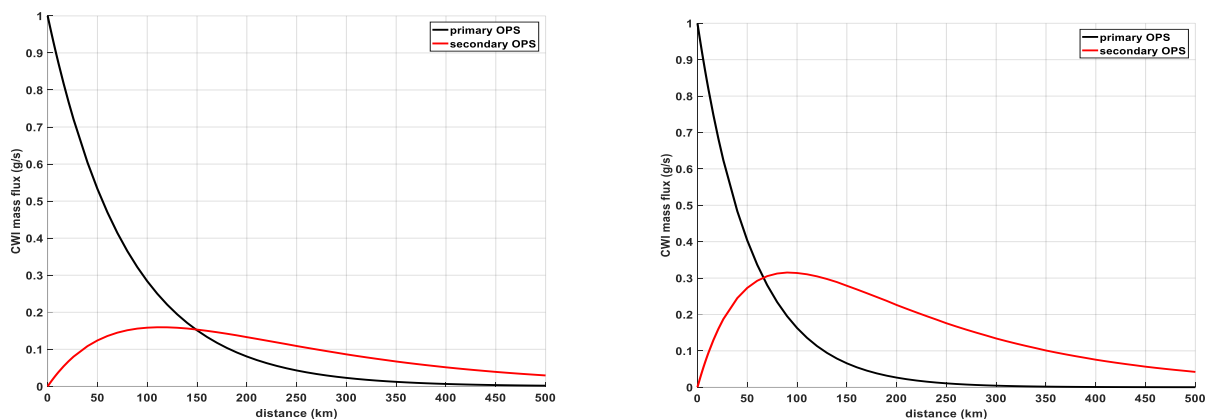- Loss of secondary species due to dry deposition and wet deposition.

Figure 7.12   Examples of cross-wind integrated mass flux of primary (black) and secondary (red) species as function of downwind distance, computed in the numerical time stepping procedure. Left panel: chemical conversion rate 4 %/h, right panel: 10 %/h. Mixing height 800 m, wind speed: 3 m/s, initial primary source strength = 1 g/s, deposition velocity 0.8 cm/s (primary) and 0.1 cm/s (secondary). Wet deposition rates 6 %/h (primary and secondary). Molar mass ratio = 18/17.

Earlier, OPS computed the 'exact' mass flux of the primary species $\tilde{Q}_{pri}$, taking into account a rising mixing height and a transport velocity depending on plume height. The numerical time stepping procedure uses a number of simplifications, such as a wind direction sector with constant mixing height and a constant transport velocity. Assuming that the secondary species is subject to the same transport processes as is the primary substance, the mass flux is corrected for these simplifications as follows:

$$\tilde{Q}_{sec} = \tilde{Q}_{sec,num} \frac{\tilde{Q}_{pri}}{\tilde{Q}_{pri,num}}.$$ (7.18)

Once the cross-wind integrated mass flux $\tilde{Q}_{sec}$ is known, the concentration at the receptor of the secondary species can be computed according to the Gaussian plume formulae (eq. **3.7**, in combination with **3.8** and **3.9** or **3.15**).

7.5   References

Asman W.A.H. and Janssen A.J. (1987) A long-range transport model for ammonia and ammonium for Europe. *Atmospheric Environment* **21**, 2099-2119.

Binkowski, F. and Shankar, U. (1995) The Regional Particulate Matter Model .1. Model description and preliminary results, J. Geophys.Res., 100, 26191–26209, 1995.

Hjellbrekke A.G. (1999) Data Report 1997; Part 1: Annual summaries. EMEP/CCC-Report 3/99, Norwegian Institute for Air Research, Kjeller, Norway.

Kitto A.M.N. and Harrison R.M. (1992) Nitrous and nitric acid measurements at sites in south-east England. *Atmospheric Environment* **26A**, 235-241.

Mijnen-Visser S., L.A. de Jongh, S.B. Hazelhorst, R. Hoogerbrugge, I. Soenario, G.J.C. Stolwijk, W.J. de Vries, R.J. Wichink Kruit, and S. Zuidberg (2024). Grootschalige concentratiekaarten Nederland. Rapprotage 2024. RIVM-rapport 2024-0059.

Ogilvie F.R. (1982) Buitenluchtverontreiniging in Delft in 1980. TNO, Delft, the Netherlands. Report G 980.

Pio C.A. and Harrison R.M. (1987) The equilibrium of ammonium chloride aerosol with gaseous hydrochloric acid and ammonia under tropospheric conditions. *Atmospheric Environment* **21**, 1243-1246.

Simpson D., A. Benedictow, H. Berge, R. Bergström, L. D. Emberson, H. Fagerli, C. R. Flechard, G. D. Hayman, M. Gauss, J. E. Jonson, M. E. Jenkin, A. Nyíri, C. Richter, V. S. Semeena, S. Tsyro, J.-P. Tuovinen, Á. Valdebenito, and P. Wind (2012) The EMEP MSC-W chemical transport model - technical description,

Atmospheric Chemistry and Physics **12**, 7825-7865, https://www.atmos-chem-phys.net/12/7825/2012/, doi 10.5194/acp-12-7825-2012.

Slanina J., Keuken M.P., Arends B., Veltkamp A.C. and Wyers G.P. (1990) Acidification research at ECN. Contribution to the Dutch Priority Programme on Acidification. ECN, Petten, the Netherlands.

Stelson A.W. and Seinfeld J.H. (1982a) Relative humidity and pH dependence of the vapor pressure of ammonium nitrate-nitric acid solutions at 25 ºC. *Atmospheric Environment* **16**, 993-1000.

Van den Hout, K.D. and Baars, H.P. (1988) Ontwikkeling van twee modellen voor de verspreiding van luchtverontreiniging door verkeer: het TNO-Verkeersmodel en het CAR Model. *TNO rapport R88/192*. (in Dutch).

Van der Swaluw E. et al. (2020) Trend Analysis of Air Pollution and Nitrogen Deposition Over the Netherlands Using the EMEP4NL and OPS Model. In: Mensink C., Gong W., Hakami A. (eds) Air Pollution Modeling and its Application XXVI. ITM 2018. Springer Proceedings in Complexity. Springer, Cham.

Wesseling, J. and van Velze, K. (2015) *Technische beschrijving van standaardrekenmethode 2 (SRM-2) voor luchtkwaliteitsberekeningen*, RIVM, https://rivm.openrepository.com/handle/10029/576049 (in Dutch).

8.   Model comparison and validation

In the original report *Description and validation of OPS-Pro 4.1,* RIVM report 500045001/2004 (van Jaarsveld, 2004) various model validation exercises, have been presented. Since then, many more model intercomparison studies and validation exercises have been published and in this chapter we will present an overview of these studies. It should be noted that results of older validation studies may not be valid for the current OPS-version; this is especially true for NH_3, where the implementation of bi-directional exchange (compensation point) in 2010 has improved model results considerably.

1. A comparison of monthly averaged concentrations and wet depositions with measurements for SO_2, SO_4^{2-} (1980-1982), NO_x, NO_3-aerosol (1987-1989), HNO_3 (1989) and NH_3 (1998-2000) on a monthly basis in van Jaarsveld (2004).
2. A comparison of trends in yearly averaged concentrations and wet depositions for SO_2, SO_4^{2-} (1981-2002), NO_x, NO_3-aerosol (1990-2002), NH_3, NH_4-aerosol (1995-2002) in van Jaarsveld (2004).
3. Comparisons for a single source (Kincaid / Prairie grass / Copenhagen experiments) in van Jaarsveld (2004).
4. A comparison between the parameterisations of Barrie (1981) for SO_2 scavenging and the one used in OPS, depending on the NH_3/SO_2 ratio in van Jaarsveld (2004).
5. Studies 1, 2 and 3 can also be found in van Jaarsveld (2005).
6. A study on the dispersion of ammonia in an agricultural area in van Pul et al. (2008).
7. An comparison of measured and modelled ammonia concentrations in nature areas in Stolk et al. (2009).
8. A study on the influence of sea-salt particles on the exceedances of daily PM_{10} air quality standards in van Jaarsveld and Klimov (2011).
9. A comparison between modelled and measured wet deposition levels of ammonium, nitrate and sulphate over the period 1992-2008 in van der Swaluw et al. (2011).
10. An application of the OPS-model in modeling the spread of Q-fever bacteria in The Netherlands in van Leuken et al. (2016).
11. A comparison between the OPS-model, the grid model LOTOS-EUROS and a hybrid combination of both models for several components (i.e. gas, particles and deposition) in van der Swaluw et al. (2017).
12. An evaluation of emission and concentration trends of ammonia in The Netherlands in Wichink Kruit et al. (2017).
13. A model comparison between CHIMERE and OPS-ST for spatial patterns in ammonia in Azouz et al. (2019).
14. Evaluations of yearly produced large-scale maps of air pollution in the Netherlands in Hoogerbrugge et al. (2019).

8.1   References

Niramson Azouz, Jean-Louis Drouet, Matthias Beekmann, Guillaume Siour, Roy Wichink Kruit, Pierre Cellier (2019) Comparison of spatial patterns of ammonia concentration and dry deposition flux between a regional Eulerian chemistry-transport model and a local Gaussian plume model. Air Quality, Atmosphere & Health, https://doi.org/10.1007/s11869-019-00691-y, April 2019

Hoogerbrugge, R and Geilenkirchen, GP and den Hollander, HA and van der Swaluw, E and Visser, S and de Vries, WJ and Wichink Kruit, RJ (2019) Large-scale concentration and deposition maps of the Netherlands: 2019 report. RIVM report 2019-0091 (in Dutch). https://doi.org/10.21945/RIVM-2019-0091
https://www.rivm.nl/publicaties/grootschalige-concentratie-en-depositiekaarten-nederland-rapportage-2019
Also available for other years.

Stolk A.P., van Zanten M.C., Noordijk H, van Jaarsveld J.A. van Pul W.A.J. (2009) Meetnet Ammoniak in Natuurgebieden, Meetnetresultaten 2005 – 2007. RIVM Rapport 680710001/2009

Van der Swaluw E., Asman, W.A.H., van Jaarsveld H., Hoogerbrugge R. (2011) Wet deposition of ammonium, nitrate and sulfate in the Netherlands over the period 1992–2008, *Atmospheric Environment*, **45**, 3819-3826, 10.1016/j.atmosenv.2011.04.017.

Van der Swaluw (Eric), Wilco de Vries, Ferd Sauter, Jan Aben, Guus Velders, Addo van Pul (2017). High-resolution modelling of air pollution and deposition over the Netherlands with plume, grid and hybrid modelling, Atmospheric Environment, Volume 155, April 2017, Pages 140-153.

Van Leuken (J.P.G.) , A.N. Swart, J. Brandsma, W. Terink, J. Van de Kassteele, P. Droogers, F. Sauter, A.H. Havelaar, W. Van der Hoek: Human Q fever incidence is associated to spatiotemporal environmental conditions. *One Health, Volume 2, December 2016, Pages 77–87.* doi:10.1016/j.onehlt.2016.03.004

Van Jaarsveld J.A. (2004) Description and validation of OPS-Pro 4.1, RIVM report 500045001/2004.

Van Jaarsveld, H., Velders G. and Van Pul A. (2005) Evaluation and validation of the OPS multi-scale model using local, national and international datasets. 10th Int. Conf. on Harmonisation of Atmospheric Dispersion models for Regulatory Purposes; 17-20 oktober 2005, Sissi, Kreta

Van Jaarsveld J.A. and D. Klimov (2011) Modelling the impact of sea-salt particles on the exceedances of daily PM_{10} air quality standards in the Netherlands. *Int. J. Environment and Pollution, Vol. 44, Nos. 1/2/3/4, 2011*

Van Pul, W.A.J., J.A. van Jaarsveld, O.S. Vellinga, M.van den Broek, M.C.J. Smits (2008) The VELD experiment: An evaluation of the ammonia emissions and concentrations in an agricultural area. *Atmospheric Environment*, **42**, 8086-8095

Wichink Kruit, R. J., Aben, J., de Vries, W., Sauter, F., van der Swaluw, E., van Zanten, M. C., and van Pul, W. A. J. (2017) Modelling trends in ammonia in the Netherlands over the 1990-2014, *Atmos. Environ., 154, 20-30,* https://doi.org/10.1016/j.atmosenv.2017.01.031, 2017.